An Investigation of the MBE Growth of
InGaAs and InAlAs Lattice Matched to InP

A thesis submitted to the Faculty of Engineering

of the University of Glasgow

for the degree of

Doctor of Philosophy

by

Mark McElhinney, B. Eng

September 1994

ProQuest Number: 10992156

ProQuest 10992156

In Memory of Donald S. Reid

"It's easy come
And it's easy go
All this talking
Is only bravado"

Paul Buchanan *'Tinseltown'*

Abstract

The MBE growth of $In_{0.53}Ga_{0.47}As$ and $In_{0.52}Al_{0.48}As$ lattice matched to InP is investigated. Accurate formulae relating the splitting between X-ray rocking curve peaks to the composition of $In_xGa_{(1-x)}As$ and $In_xAl_{(1-x)}As$ are developed, enabling accurate characterisation of alloy composition close to the lattice matched condition. Close scrutiny of the behaviour of InAs RHEED intensity oscillations indicates that the onset of In droplet formation during InAs growth correlates with a small reduction in the period of the intensity oscillations. This reduction can therefore be used to identify the minimum permissible As_2 partial pressure for good morphology growth at any substrate temperature. The measured values of minimum As_2 flux for the growth of InAs agree very well with predictions based on simple thermodynamic arguments. These arguments can be extended to deal with the behaviour of $In_{0.53}Ga_{0.47}As$ and $In_{0.52}Al_{0.48}As$ by treating the ternary alloys as a pseudo-binary compounds. The results are again in excellent agreement with experimental measurements, although in the case of $In_{0.52}Al_{0.48}As$ it is necessary to derive the necessary thermodynamical constants by performing a fit to the experimental data.

Photoluminescence characterisation of bulk $In_{0.53}Ga_{0.47}As$ indicates the presence of a surface InAs segregation layer whose thickness is controlled by the mismatch between the layer and the substrate. Accurate control of alloy composition, obtained by calibrating the incident group III fluxes using RHEED oscillations on separate substrates, enables the thickness of the segregation layer to be minimised. The accuracy of the RHEED calibration technique is demonstrated by the close correlation between the measured and predicted wavelengths of photoluminescence peaks from a series of single quantum well samples. It is also shown that a marked improvement in the interface quality of single quantum wells is obtained by increasing the substrate temperature during growth and minimising the As_2 overpressure.

A series of high quality Si ∂- and slab-doped $In_{0.53}Ga_{0.47}As$ samples has been grown with design doping densities in the range $2 \times 10^{12} cm^{-2}$ to $1.5 \times 10^{13} cm^{-2}$. Analysis of Shubnikov-de Haas oscillations obtained for the samples shows increasing amphoteric behaviour and spreading away from the doping plane as the doping density is increased. By distributing the Si dopant atoms through a thin slab during growth it is possible to increase the activity of the Si and obtain comparable spreading, suggesting that this is the more efficient method of generating high carrier densities in $In_{0.53}Ga_{0.47}As$.

Table of Contents

List of Figures

Chapter 4

Chapter 5

Chapter 6

Chapter 7

Chapter 8

Chapter 9

List of Tables

Chapter 8

Chapter 1

Introduction

1.1 General Introduction

The molecular beam epitaxy (MBE) process utilises the reaction of one or more thermally produced beams of atoms and molecules with a heated substrate held in ultra-high-vacuum (UHV) conditions. The first practical demonstration of this process for GaAs was by Gunther[1] in 1958 on glass substrates so the layers produced were polycrystalline. It was not until ten years later when monocrystalline material was produced by Davey et al [2] and Arthur[3] that films grown by MBE were shown to have electrical and optical properties which were comparable to those produced by the then dominant growth techniques, such as liquid phase epitaxy (LPE). MBE has several advantages: it is possible to obtain precise control over layer thicknesses, doping profiles, and uniformity across the wafer. The UHV environment of the growth chamber allows the growth process to be controlled in situ by a range of measurement techniques such as mass spectrometry, reflection high energy electron diffraction[4] (RHEED), Auger electron spectroscopy[5], X-ray photoelectron spectroscopy[6], low-energy electron diffraction[7], electron energy loss spectroscopy[8] and secondary-ion mass spectroscopy[9].

Much of the initial research into the growth of III-V materials by MBE involved the GaAs/AlGaAs material system. This was preferred to other possible III-V combinations since the conjunction of GaAs with AlGaAs produced abrupt changes in band-gap energies and refractive indices, while at the same time maintaining an almost identical lattice constant. As a result, GaAs/AlGaAs has been the most extensively studied of the III-V systems and the surface dynamics and growth kinetics have been thoroughly investigated. Early pioneering work by Foxon and Joyce[10,11], in particular, has given a clear understanding of the growth processes and several comprehensive reviews on the subject have been published[12,13,14].

The diversification of MBE into other materials systems was prompted by two separate requirements: the necessity of improving the performance of existing devices, which had become limited by the basic properties of the GaAs/AlGaAs system, and the need to tailor the operating wavelength of optical devices to specific applications. The indium containing ternary InGaAs/AlInAs system lattice matched to InP became of interest since it offered improvement in the performance of

millimetre wave components[15] but could also operate at wavelengths suitable for a variety of optical devices, especially in the area of fibre communication[16].

High electron mobility transistors (HEMTs) are a fundamental part of many millimetre wave systems. In these devices, electrons are transferred from a highly doped wide-gap material to a narrow-gap intrinsic material. The electrons form a 2-dimensional electron gas (2DEG) at the hetero-interface, which is spatially separated from the donor. This separation between donor impurities and donated electrons reduces scattering in the structure and enables devices to be produced with very high electron mobilities. The maximum doping density of the 2DEG is limited by the conduction band offset, ΔE_c, at the interface. For $GaAs/Al_xGa_{(1-x)}As$ devices, the value of ΔE_c in the range $0 \leq x \leq 0.45$ is given by[17]:-

$$\Delta E_c = 0.81x \qquad\qquad\qquad (1.1)$$

where x is the Al fraction in the $Al_xGa_{(1-x)}As$ and is, in practice, limited to about 0.3 as higher values produce deep level traps which degrade device performance. This effectively restricts the conduction band offset in $GaAs/Al_xGa_{(1-x)}As$ to a maximum value of 0.24eV. The conduction-band offset between $In_{0.53}Ga_{0.47}As$ and $In_{0.52}Al_{0.48}As$ is 0.52eV, more than twice as large as GaAs/AlGaAs. This allows higher 2DEG densities and provides stronger confinement for the quantum well that is formed at the interface.

The relative effective mass of electrons in $In_{0.53}Ga_{0.47}As$ is 0.041, which is lighter than the GaAs value of 0.067. This results in higher electron velocities and hence smaller electron transit times through $In_{0.53}Ga_{0.47}As$ devices. A comparison of the velocity-field characteristics[17] of Si, GaAs and $In_{0.53}Ga_{0.47}As$ is shown in Figure 1.1. The maximum electron velocity in $In_{0.53}Ga_{0.47}As$ is $\approx 3 \times 10^7 cm \ s^{-1}$, which is very much larger than both Si and GaAs, making $In_{0.53}Ga_{0.47}As$ ideal for use as the active channel in HEMT structures.

2
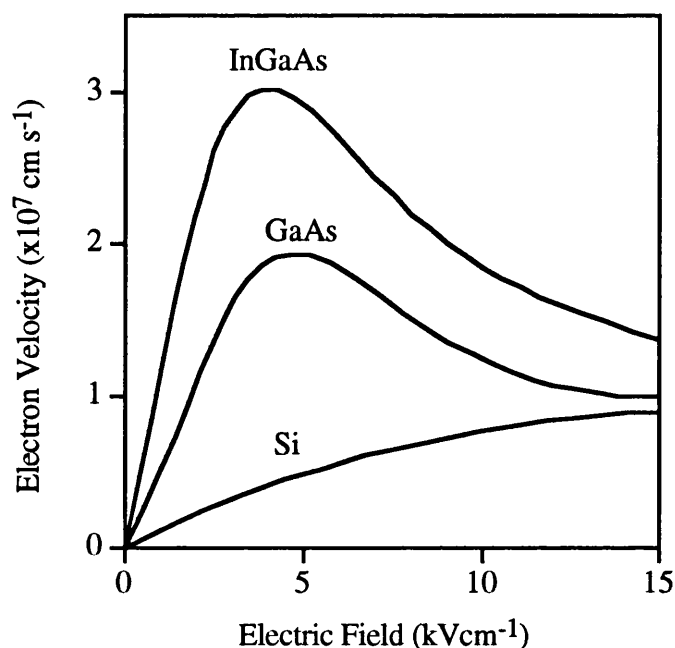
Figure 1.1. Velocity-Field characteristics of electrons in Si, GaAs and $In_{0.53}Ga_{0.47}As$

(reproduced from reference 17)

Another attraction of $In_{0.53}Ga_{0.47}As$ is its larger energy separation between the Γ and L valleys within the band structure. Electrons find it more difficult to get scattered out of the high-mobility valley and as a result when, they first encounter an electric field, they are accelerated to higher velocities before the first scattering event occurs. The velocity overshoot is therefore stronger in $In_{0.53}Ga_{0.47}As$-HEMT's, which further enhances their speed advantage over GaAs based devices for high frequency applications.

$In_{0.53}Ga_{0.47}As/In_{0.52}Al_{0.48}As$ HEMT's on InP substrates have been produced with current gain cutoff frequencies of over 300GHz[18], and minimum noise figures of 1.2dB at 94GHz[19]. This makes $In_{0.53}Ga_{0.47}As/In_{0.52}Al_{0.48}As$ devices very promising for operation in the 94 and 140GHz atmospheric windows. Applications for such high frequency devices include future communications systems operating at more than 40Gbs[-1], high definition radar systems, smart weapons, and collision detectors.

A principal goal of optoelectronic device research has been high transmission rate capacity over long distances. This requires lasers and detectors which operate at a wavelength of 1.55μm where optical fibres have their minimum loss. GaAs optical devices which operate at 0.8μm are not appropriate for this application, and interest has focused on the InP based materials systems such as $In_{0.53}Ga_{0.47}As/In_{0.52}Al_{0.48}As$. It is already possible to obtain reliable

3

low-threshold lasers based on $In_{0.53}Ga_{0.47}As$ grown by metal organic chemical vapour deposition (MOCVD), and integration of a PIN detector diode with a MESFET transistor on InP has also been achieved[20]. In general, however, the technology for InP optoelectronic integrated circuits (OEIC's) has not progressed much beyond small-scale integration[21]. This is in part due to the limitations of the growth technology, which has meant that InP and $In_{0.53}Ga_{0.47}As$ electronic devices integrated with optical devices have not been able to match the performance of GaAs based devices.

In addition to fibre communications systems, InP based technology has been used in optical computing applications[22]. Optical signals do not interfere with each other and are free from the capacitance effects associated with electrical signals: this makes massively parallel data-processing systems possible[23]. An example of the type of device being investigated for such a system is the light amplifying optical switch[24] (LAOS). This is a phototransistor vertically integrated with a light-emitting diode (LED) or a laser. The device can be made by epitaxial growth of AlInAs and InGaAs on InP substrates. A schematic diagram of a LAOS is shown in Figure 1.2.
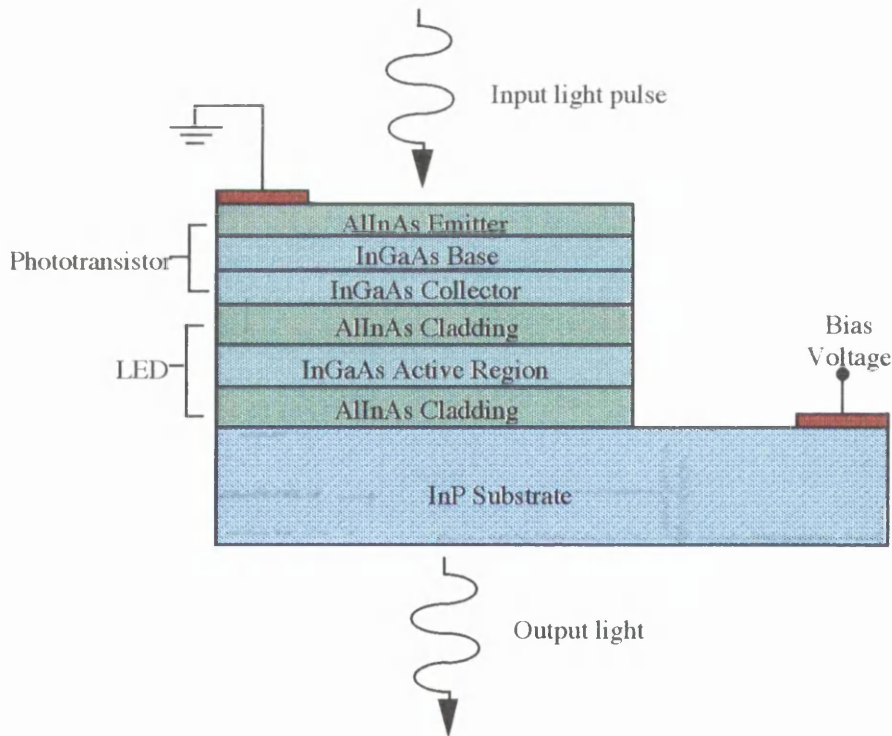
Figure 1.2. Structure of a LAOS device

An input light pulse, through the transparent wide gap emitter, produces a current through the phototransistor. This current flows through the LED, turning it on, and producing light in both upward and downward directions. The light

emitted by the LED causes the phototransistor to remain on even after the input pulse has ended. The transparent InP substrate allows transmission of the light output from the LED, which has effectively been latched by the input pulse. The device remains on and emitting if current is kept above a certain critical value. Such devices have applications in smart pixel computing and image processing.

1.2 Background

The aim of this project was to investigate the MBE growth and properties of $In_{0.53}Ga_{0.47}As$ and $In_{0.52}Al_{0.48}As$ lattice matched to InP. The $In_{0.53}Ga_{0.47}As/In_{0.52}Al_{0.48}As$ system is, as has been described above, superior to the $GaAs/Al_xGa_{1-x}As$ system for many applications. Both the opto-electronic and nano-electronic research groups within the Electronic and Electrical Engineering Department at the University of Glasgow are interested in fabricating devices which will exploit the properties of this materials system.

The requirements of these research groups are for high quality layers with good uniformity and reproducibility which will enable the reliable fabrication of both opto-electronic and microwave devices. While the initial work was to be on the lattice matched ternary $In_{0.53}Ga_{0.47}As/In_{0.52}Al_{0.48}As$ system it was foreseen that this would lead to the growth of strained device structures such as pseudomorphic HEMTs and strained laser structures. A flexible approach was therefore required which would enable the growth conditions to be tailored to the desired structure and would allow the incident fluxes to be accurately calibrated to provide the correct composition and growth rate without the need to grow several calibration layers. It was decided to attempt to perform the group III calibrations using RHEED intensity oscillations[25] on separate InAs and GaAs calibration samples. This technique had not previously been tried and it was thought that it had the capability to give the same control over composition and growth rate as was obtainable for the GaAs/AlGaAs system. There were, however, problems discovered in this approach. The first difficulty encountered was a discrepancy between measurements of the composition of $Al_xGa_{1-x}As$ layers using a double crystal X-ray diffraction (DCXD) system and the intended composition which had been calibrated by RHEED. It was essential to have confidence in the RHEED calibration technique for the $GaAs/Al_xGa_{1-x}As$ system before extending the method to the more complicated $In_{0.53}Ga_{0.47}As/In_{0.52}Al_{0.48}As$ system, and it was equally important to be able to accurately determine the composition of $In_xAl_{1-x}As$ and $In_xGa_{1-x}As$ layers after growth, so the difference between the measured and calibrated compositions had to be resolved. Chapter 2 of this thesis shows that the disagreement was produced by an incorrect derivation of the composition of a

strained ternary layer from the lattice distortion produced by the strain. A new, more precise model relating the strain between $Al_xGa_{1-x}As$ and GaAs to the consequent deformation of the $Al_xGa_{1-x}As$ lattice structure[26] is presented, based on the assumption that RHEED oscillations can be used to accurately determine the composition of the alloy. This model is then applied to $In_xAl_{1-x}As$ and $In_xGa_{1-x}As$, enabling a more accurate determination of the composition of these alloys than has so far been possible using the DCXD technique.

The second difficulty discovered with the RHEED oscillation technique was an apparent inconsistency between the calibration growth rate of InAs on an InAs substrate and the In content of bulk $In_xAl_{1-x}As$ and $In_xGa_{1-x}As$ layers. It was discovered that ternary layers grown with nominally identical calibration points had a composition distribution which was double-peaked. The origin of this distribution was traced to a reduction in the steady state incorporation of In into InAs at moderate substrate temperatures, well removed from the regime where 'conventional' In desorption becomes significant. Chapter 3 examines this effect in detail and discusses the influence of substrate temperature and As overpressure on the incorporation of In into InAs. The thermal stability of InAs is examined and the results are compared with theoretical predictions based on thermodynamical arguments.

Many of the effects discovered during investigations into the homo-epitaxial growth of InAs were found to be present in the growth of $In_{0.53}Ga_{0.47}As$ and $In_{0.52}Al_{0.48}As$. Chapter 4 discusses the growth of these materials and points out the similarities with InAs. The thermodynamic model developed for InAs is expanded to include the ternary alloys and a coherent picture for the conditions necessary for their growth is derived[27]. The results explain the inconsistencies between the growth conditions recommended in the literature which range from substrate temperatures of 500°C with V:III pressure ratios of 40:1[28] to substrate temperatures of 580°C with pressure ratios of $\approx$4:1[29].

The measured optical and electrical properties of undoped $In_{0.53}Ga_{0.47}As$ and $In_{0.52}Al_{0.48}As$ grown by MBE are given in Chapter 5. Particular emphasis is given to photoluminescence (PL) spectra containing anomalous peaks which are attributed to the presence of an In-rich segregation layer on the surface of the sample, the thickness of which is determined by the epi-layer/substrate strain. It is shown that by accurately lattice matching $In_{0.53}Ga_{0.47}As$ and $In_{0.52}Al_{0.48}As$ epi-layers high optical quality material can be obtained with a much lower As overpressure than is common in the literature[30,31]. Chapter 6 shows that the minimisation of As overpressures can also be used to enable the growth of $In_{0.53}Ga_{0.47}As/In_{0.52}Al_{0.48}As$ quantum well samples containing high quality

interfaces, demonstrated by the presence of monolayer splitting[32,33] in their PL spectra.

A systematic study of the magnetotransport properties of a series of Si ∂- and slab-doped $In_{0.53}Ga_{0.47}As$ samples was undertaken as an initial step towards understanding the behaviour of Si in both $In_{0.53}Ga_{0.47}As$ and $In_{0.52}Al_{0.48}As$. The aim of this investigation was to optimise Si-doping profiles in device structures. Chapter 7 details the results of the study, and presents the first consistent set of magnetotransport measurements for ∂-doped $In_{0.53}Ga_{0.47}As$.

Two examples of device structures are given in Chapter 8 and the MBE growth issues particular to each structure are discussed. Characterisation data for devices fabricated from the material is given and a comparison is made with published performance figures.

1.3 Growth System

Epitaxial layers were grown in an Varian Modular Gen II system as shown in Figure 1.3.
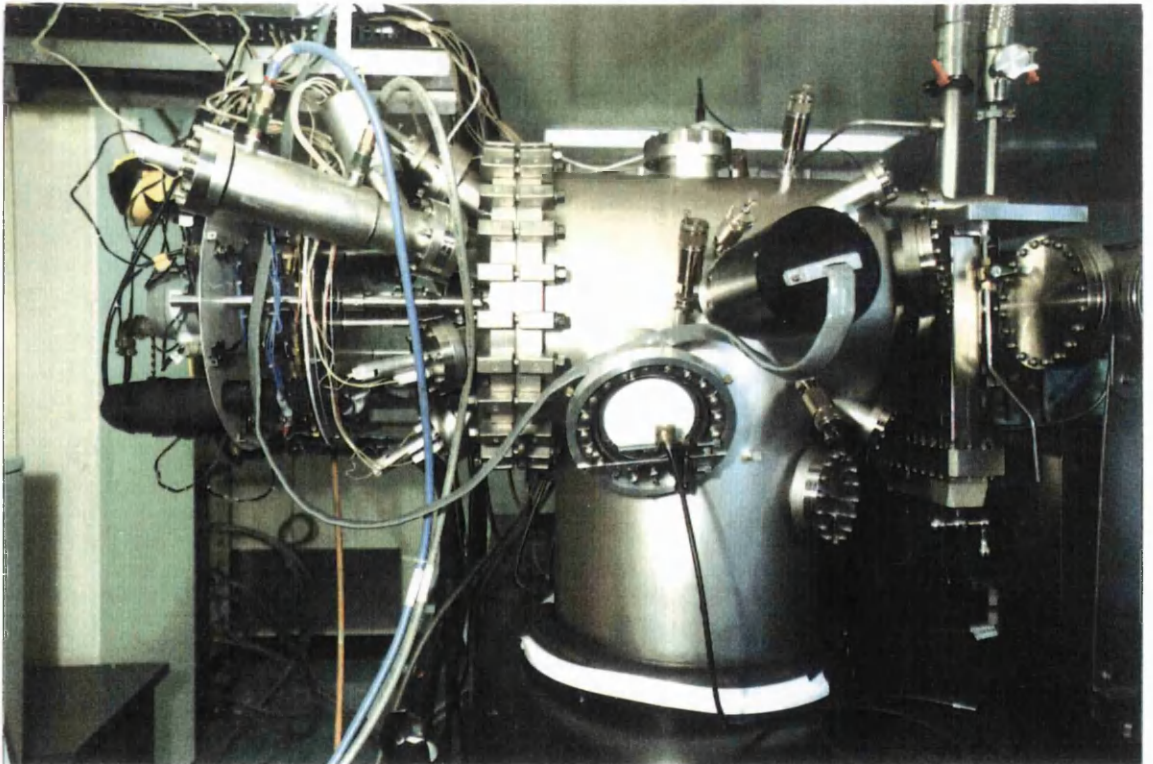
Figure 1.3. Varian Modular Gen II MBE system.

The system is composed of three vacuum chambers: an entry/exit interlock chamber, an intermediate buffer chamber, and the main growth chamber itself. This arrangement is shown schematically in Figure 1.4.
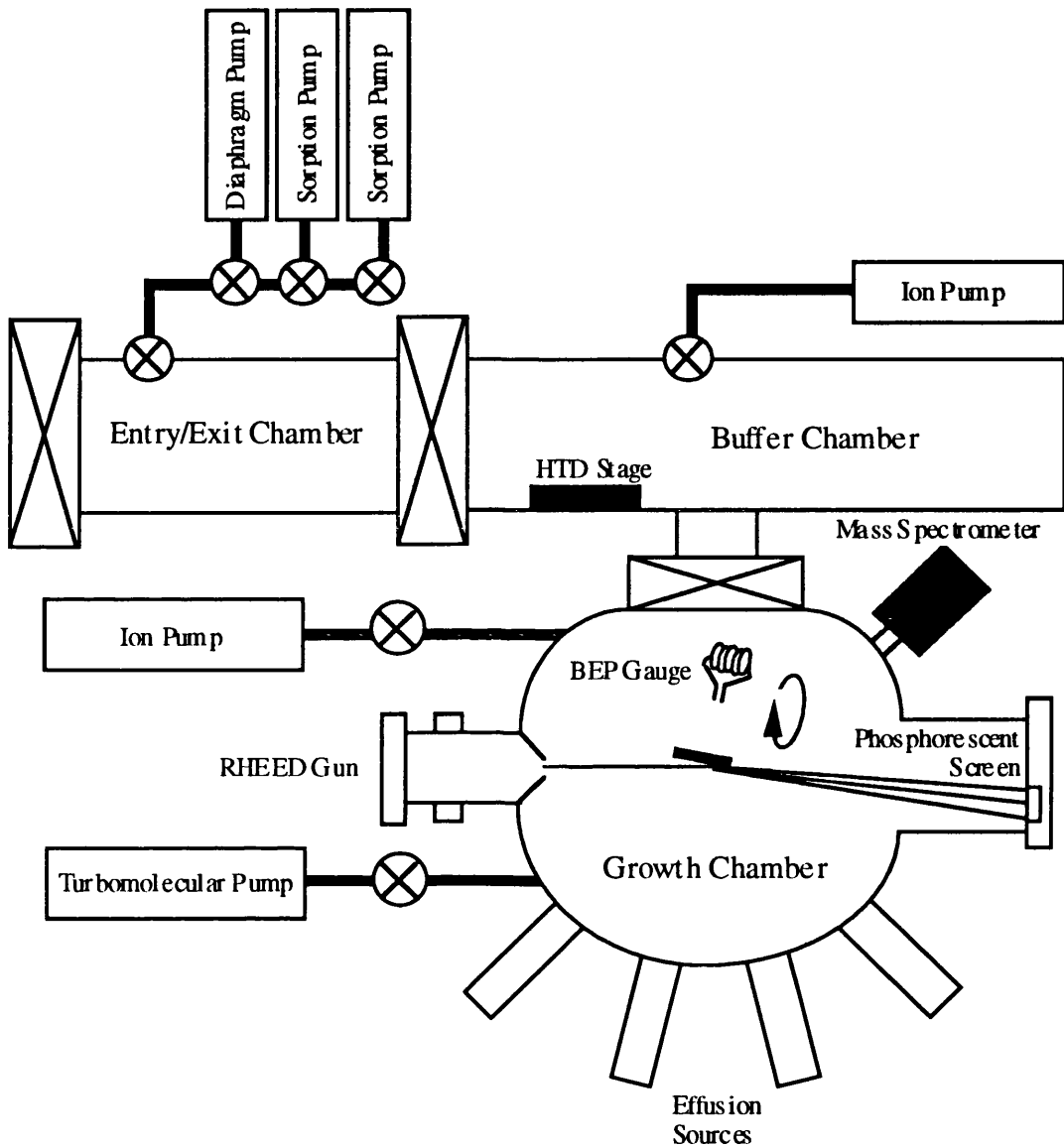
Figure 1.4. Schematic diagram of MBE system.

Several different pumping systems are employed for each chamber. When substrates have been loaded, the entry exit chamber is pumped from atmospheric pressure by a diaphragm pump, sorption pumps and a CTI-Cryogenics Ltd 350l/s cryopump consecutively. Atmospheric water vapour is then removed by baking the chamber walls at a temperature of 200°C for a period of three hours. On cooling, the pressure in the entry exit chamber reaches $\approx 5 \times 10^{-9}$ Torr, at which point substrates are transferred to the buffer chamber for degas. This chamber is pumped

by an Varian 200l/s ion pump and contains a Ti-ball to remove any remaining water vapour. Substrates are given a prolonged degas on a heater stage mounted in the buffer chamber, before being transferred to the growth chamber for epitaxial deposition. The pumping system for the growth chamber is configured to deal with phosphorus and contains a Balzers GmbH 350l/s plasma turbomolecular pump and liquid nitrogen trap in addition to an Varian 400l/s ion pump and a Ti sublimation pump, giving a base pressure of $\approx 1 \times 10^{-11}$ Torr. The residual level of gases remaining in the growth chamber is monitored using a quadrupole mass spectrometer and the beam equivalent pressures of growth fluxes incident on a substrate can be monitored by an ion gauge which is rotated to the growth position. *In-situ* growth characterisation is performed using a 15keV reflection high energy electron diffraction arrangement, which is used to examine surface reconstruction and perform growth rate measurements using intensity oscillations of the specular spot.

Standard solid source effusion furnaces for Al, Si and Be were used, together with 'hot-lip' type In and Ga sources, and Varian 'cracker' furnaces[34] to produce As_2. The arsenic cracker was operated at a temperature of $\approx 700°C$ producing a >95% conversion of As_4 molecules into As_2[35,36]. The suppliers and purity of the materials loaded into the effusion cells are given in Table 1.1.

Material	Supplier	Purity
Indium	Johnson Matthey Ltd.	6N's
Gallium	Rhône Poulenc Ltd.	8N's
Aluminium	Metals Crystals & Oxides Ltd.	6N's
Arsenic	Preussag GmbH.	7N's

Table 1.1. Suppliers and purity of source materials used for MBE growth.

1.4 Calculation of As_2 Partial Pressures

The BEP gauge controller is calibrated for nitrogen and so a scaling factor must be used to obtain the real As_2 partial pressure from the BEP gauge reading. The relationship between the ionization efficiency η of a given species and the ionisation efficiency of nitrogen is given by[37] :-

$$\frac{\eta}{\eta_{N_2}} = \left(\frac{0.4Z}{14}\right) + 0.6 \qquad (1.2)$$

where Z is the atomic number. For As_2 the atomic number is 75, which gives a ratio between the ionization efficiencies of 2.74. The measured As_2 partial pressure must, therefore, be divided by 2.74 to obtain the real As_2 partial pressure. For a pressure of 1×10^{-7} Torr, the collector current of the BEP gauge is 11.75 nA[38]. The minimum possible As_2 partial pressure which permits the growth of $In_{0.53}Ga_{0.47}As$ at 1μm/hr produces a collector current of 150 nA, corresponding to a pressure reading of 1.27×10^{-6} Torr which is, in turn, equivalent to a real As_2 partial pressure of 4.6×10^{-7} Torr. This value is extensively quoted in the following chapters as the minimum permissible As_2 partial pressure for growth at 1μm/hr.

1.5 Sources of Error in Growth Rate Measurement by RHEED

1.5.1 Flux Transients

Group III furnaces can produce both long and short term flux transients which cause the growth rate to differ from that calibrated by RHEED. Short term transients are caused by a change in the thermal equilibrium of the furnace, which is produced by opening its shutter and reducing in the amount of heat which is reflected back into the furnace. Such effects cause the flux density to fall during the first few minutes after the shutter is opened. Figure 1.5 shows the measured response of the BEP gauge when the indium shutter is opened. No significant short term flux transient is observed indicating that the growth rate calibrated by RHEED is an accurate value for the actual growth rate during growth. Similar results were obtained for both the aluminium and gallium furnaces.

10
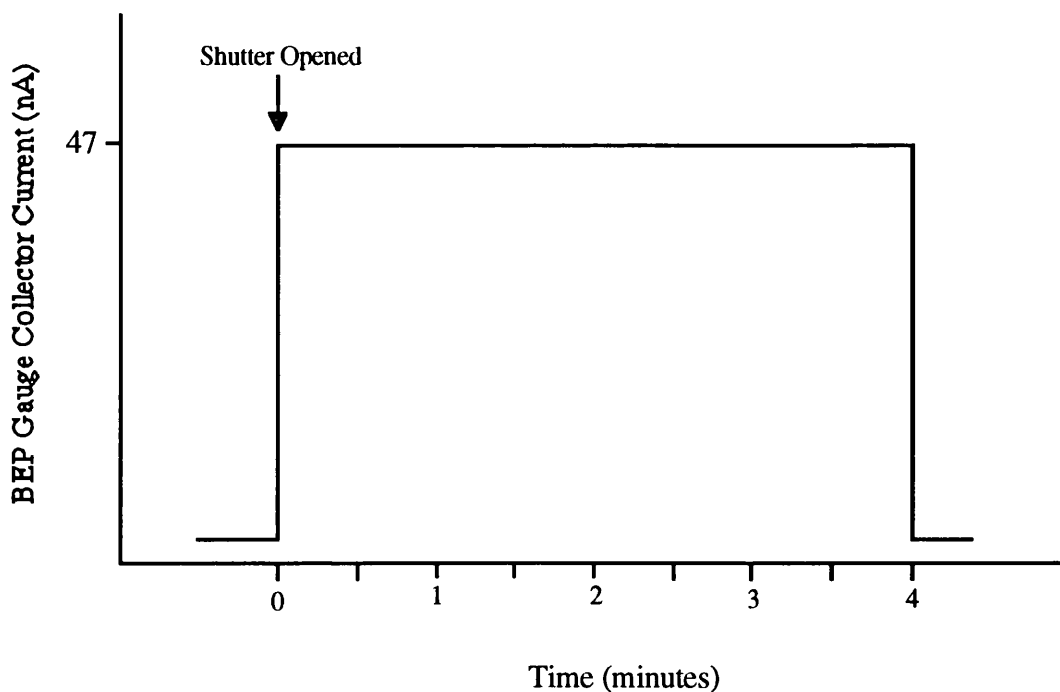
Figure 1.5. Measured BEP gauge collector current when In shutter is opened.

Long term flux transients are produced by the depletion of the source material over time. This effect is greater in furnaces using conical crucibles because of more rapid reductions in melt surface area in those furnaces. The rate of flux change varies with time and is typically very low at the start of a growth run when the furnaces have just been recharged. Measurement of growth rates before and after growth at 1μm/hr of a 15μm GaAs layer gives a drop in growth rate of only 0.5% during this period. As the distance between the crucible orifice and the melt surface increases, however, the rate of change of the growth rate increases and reaches values as high as 4% over 15 hours. Experimental evidence suggests that the samples grown for this study did not suffer from significant long term flux transients. Narrow linewidth X-ray peaks were observed for all of the ternary samples, indicating little or no composition drift during growth; and an $In_{0.23}Ga_{0.87}As$/GaAs MQW structure approximately 1.5μm thick displayed a state of the art linewidth (see Chapter 8), indicating minimal variation in growth rate during its growth.

1.5.2 Flux Distribution

The physical geometry of an MBE growth chamber results in an uneven flux distribution across a large wafer. In most MBE systems this is compensated for by rotating the wafer to average out such variations. RHEED flux calibration is performed without rotation, which means that there is a danger that unless the

11

calibration is performed at the centre of rotation then there will be a discrepancy between the calibrated flux density and the average flux density during growth. The samples used for performing RHEED calibrations were 5mm squares.
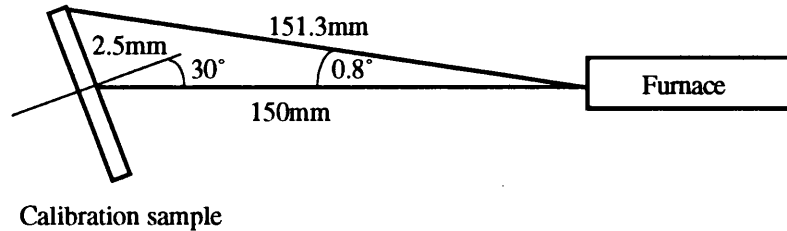
Figure 1.6. Geometry for a simple Lambertian model of flux variation across a 5mm square calibration sample. The furnace is 150mm from the sample and at an angle of 30° to it.

A simple Lambertian model[39] (see Figure 1.6) for the distribution of flux across such a sample gives the following relationship between the flux density at the centre of rotation and 2.5mm away from the centre :-

$$\frac{F_0}{F_{2.5}} = \frac{\left(\dfrac{\cos 30°}{150^2}\right)}{\left(\dfrac{\cos 30.8°}{151.2^2}\right)} = 1.02 \qquad (1.3)$$

i.e. a 2% error in flux density is obtained if the calibration is performed at the edge of the sample. This is a considerable overestimate since the furnaces are very far from being point sources. In practise, negligible variation in flux density has been observed across a calibration sample and it is believed that this effect may be ignored.

1.6 References

1   K.G. Gunther in 'Compound Semiconductors'
    Edited by R.K. Willardson and H.L. Goering
    New York 1962 Vol.1 p313

2   'Epitaxial GaAs Films Deposited by Vacuum Evaporation'
    J.E. Davey and T. J. Pankey
    Journal of Applied Physics 1968 Vol.39 No.6 pp1941-1943

3   'Interaction of Ga and As_2 Molecular Beams with GaAs Surfaces'
    J. R. Arthur
    Journal of Applied Physics 1968 Vol.39 No.12 pp4032

4   'Molecular-Beam Epitaxial-Growth On Radiation-Heated Substrates'
    S.C. Palmateer, B.R. Lee and J.C.M. Hwang
    Journal Of The Electrochemical Society 1984 Vol.131 No.12 pp.3028-3029

5   C.C. Chang in 'Characterization of Solid Surfaces'
    Edited by P.F. Kane and G.B. Larrabee
    (Plenum, New York 1974)

6   A.B. Christie in 'Methods of Surface Analysis'
    Edited by J.M. Walls
    Cambridge University Press, Cambridge, 1989

7   R.Z. Bachrach in 'Crystal Growth'
    Edited by B.R. Pamplin
    Pergamon Press, Oxford, 1980

8   'Electron Energy Loss Spectroscopy of GaAs and Ge surfaces'
    R. Ludeke and L. Esaki
    Physics Review Letters 1974 Vol.33 No.12 pp653-657

9   'Quantitative-Analysis of Buried Interfacial Impurity Layers by SIMS and RBS'
    P. Williams, J.E. Baker, J.A. Davies, T.E. Jackman
    Nuclear Instruments & Methods In Physics Research 1981 Vol.191 No.1-3
    pp.318-322

10 'Interaction Kinetics of As_4 and Ga on (100) GaAs Surfaces Using a
    Modulated Beam Technique'
    C.T. Foxon, B.A. Joyce
    Surface Science 1975 Vol.50 No.2 pp434-450

11 'Interaction Kinetics of As_2 and Ga on (100) GaAs Surfaces'
    C.T. Foxon, B.A. Joyce
    Surface Science 1977 Vol.64 No.1 pp293-304

12 'Growth of III-V Semiconductors by Molecular-Beam Epitaxy and their Properties'
A.Y. Cho
Thin Solid Films 1983 Vol.100 No.4 pp.291-317

13 C.T. Foxon and B.A. Joyce in 'Growth and Characterisation of Semiconductors'
Edited by R.A. Stradling and P.C. Klipstein
(Adam Hilger, Bristol) 1990

14 'The Technology and Physics of Molecular Beam Epitaxy'
edited by E.H.C. Parker
(New York, London, 1985)

15 'Electron Mobilities in Modulation Doped $In_{0.53}Ga_{0.47}As/In_{0.52}Al_{0.48}As$ Heterojunctions Grown by Molecular Beam Epitaxy'
K.Y. Cheng, A.Y. Cho, T.J. Drummond, H. Morkoc
Applied Physics Letters 1982 Vol.40 No.2 pp147-149

16 '$1.5-1.6\mu m$ $In_{0.53}Ga_{0.47}As/In_{0.52}Al_{0.48}As$ Multiquantum Well Lasers Grown by Molecular Beam Epitaxy'
H. Temkin, K. Alavi, W.R. Wagner, T.P. Pearsall and A.Y. Cho
Applied Physics Letters 1983 Vol.42 No.10 pp845-847

17 Semiconductor and Electronic Devices (3rd ed)
A. Bar-Lev
(London, Prentice-Hall, 1993)

18 '50-nm Self-Aligned-Gate Pseudomorphic AlInAs GaInAs High Electron-Mobility Transistors'
L.D. Nguyen, A.S. Brown, M. A. Thompson and M.A. Jelloian
IEEE Transactions On Electron Devices 1992 Vol.39 No.9 pp.2007-2014

19 'Low-Frequency Noise Behavior of $0.15-\mu M$ Gate-Length Lattice-Matched and Lattice-Mismatched MODFETs on InP Substrates'
M.S. Thurairaj, M.B. Das, J.M. Ballingall, P. Ho, P.C. Chao, M.Y. Kao
IEEE Electron Device Letters 1991 Vol.12 No.8 pp.410-412

20 'InGaAsP/InP Long Wavelength Optoelectronic Integrated-Circuits (OEICs) for High-Speed Optical Fiber Communication-Systems'
A. Suzuki, K. Kasahara and M. Shikada
Journal Of Lightwave Technology 1987 Vol.5 No.10 pp.1479-1487

21 'Optoelectronic integration: a technology for future telecommunication systems'
R.F. Leheny
IEEE Circuits and Devices Magazine 1989 Vol.5 No.3 pp38-41

22 'Integrated Optical NAND Gate'
X. An, K.M. Geib, M.J. Hafich, L.M. Woods, S.A. Feld, F.R. Beyette, G.Y. Robinson and C.W. Wilmsen
Electronics Letters 1992 Vol.28 No.16 pp.1545-1546

23 'Switching Light with Light'
C.W. Wilmsen, S.A. Feld, F.R. Beyette and X. An
IEEE Circuits And Devices Magazine 1991 Vol.7 No.6 pp.21-25

24 'Smart pixels using the light amplifying optical switch (LAOS)'
C.W. Wilmsen, F.R. Beyette, X. An, S.A. Feld and K.M. Geib
IEEE Journal of Quantum Electronics 1993 Vol.29 No.2 pp769-774

25 'Dynamics of Film Growth of GaAs By MBE from Rheed Observations'
J.H. Neave, B.A. Joyce, P.J. Dobson and N. Norton
Applied Physics A-Solids And Surfaces 1983 Vol.31 No.1 pp.1-8

26 'Measurement of Aluminum Concentration in Epitaxial Layers of $Al_xGa_{1-x}As$ on GaAs by Double Axis X-Ray-Diffractometry'
B.K. Tanner, A.G. Turnbull, C.R. Stanley, A.H. Kean, M. McElhinney
Applied Physics Letters 1991 Vol.59 No.18 pp.2272-2274

27 'MBE Growth and Thermodynamic Analysis of InGaAs and InAlAs Lattice
   Matched to InP'
   M. McElhinney and C.R. Stanley
   Presentation to the Eighth International Conference on MBE
   Osaka, Japan, Aug/Sep, 1994
   to be published in the Journal of Crystal Growth

28 'III-V Alloy Growth by Molecular Beam Epitaxy'
   C.E.C. Wood
   in 'GaInAsP Alloy Semiconductors'
   edited by T.P. Pearsall
   (Wiley, New York, 1982)

29 'Very High Purity $In_{0.53}Ga_{0.47}As$ Grown by Molecular Beam Epitaxy'
   T. Mishima, M. Takahama, Y. Uchida, T. Tanoue and S. Takahashi
   Journal of Electronic Materials 1991 Vol.20 No.1 pp113-116

30 Optical-Quality GaInAs Grown by Molecular-Beam Epitaxy'
   G. Wicks, C.E.C. Wood, H. Ohno, L.F. Eastman
   Journal Of Electronic Materials 1982 Vol.11 No.2 pp.435-440

31 'Growth of InGaAs and InAlAs for Laser Diodes'
   R. Sivertsen, K. Øvsthus, D. Wang, P.I. Jensen, S.I. Hansen, K. Pettersen,
   A. Sudbø, L. Hafskjær and K. Gjønnes
   Presentation to the 7th European Workshop on MBE
   Bardonecchia, Italy 1993

32 'Heterointerfaces in Quantum Wells and Epitaxial Growth Processes:
   Evaluation by Luminescence Techniques'
   M.A. Herman, D. Bimberg and J. Christen
   Journal of Applied Physics 1991 Vol.70 No. 2 ppR1-R52

33 'Structural-Changes of the Interface, Enhanced Interface Incorporation of
   Acceptors, and Luminescence Efficiency Degradation in GaAs Quantum Wells
   Grown by Molecular-Beam Epitaxy Upon Growth Interruption'
   D. Bimberg, D. Mars, J.N. Miller, R. Bauer, D. Oertel
   Journal Of Vacuum Science & Technology B-Microelectronics Processing and
   Phenomena 1986 Vol.4 No.4 pp.1014-1021

34 'Characterization of High-Purity GaAs Films Grown by Molecular-Beam Epitaxy from a Solid As Cracker'
R. Chow, R. Fernandez, D. Atchley, K. Chan, D. Bliss
Journal Of Vacuum Science & Technology B-Microelectronics Processing and Phenomena 1990 Vol.8 No.2 pp.163-167

35 'Dimer Arsenic Source Using a High-Efficiency Catalytic Cracking Oven for Molecular-Beam Epitaxy'
J.C. Garcia, A. Barski, J.P. Contour and J. Massies
Applied Physics Letters 1987 Vol.51 No.8 pp.593-595

36 'Peak Electron Mobilities Between 2.75 and $3.32 \times 10^5 cm^2 v^{-1} s^{-1}$ in GaAs Grown by Molecular-Beam Epitaxy with As_2'
C.R. Stanley, M.C. Holland and A.H. Kean
Applied Physics Letters 1990 Vol.57 No.19 pp.1992-1994

37 G.J. Davies and D.Williams in 'The Technology and Physics of Molecular Beam Epitaxy'
Edited by E.H.C. Parker
(Plenum Press, New York, 1985)

38 Varian ion gauge controller handbook

39 'Geometrical and Physical Optics'
R.S. Longhurst
(Longmans, London, 1964)

Chapter 2
Lattice Constant Determination by Double Crystal X-Ray Diffraction

2.1 Introduction

The composition of an epitaxial film decides its optical and electrical properties, governs the amount of strain between the epi-layer and the substrate, and hence controls the critical thickness of the film. The growth of mismatched layers for device applications requires accurate control of the relative proportions of the elements in the component alloys to obtain the expected performance. Determination of alloy compositions is also important for the growth of $In_{0.53}Ga_{0.47}As$ and $In_{0.52}Al_{0.48}As$ lattice-matched to InP substrates since flux calibration for this alloy system is not straightforward and small compositional changes can produce large changes in the lattice constants of the epi-layers.

The double crystal X-ray diffraction (DCXD)[1,2] technique allows measurement of the difference in lattice constant between an epi-layer and the substrate material, which can be used to derive the composition of ternary alloys. The calculation of the composition of an alloy from its mismatch with the substrate relies on knowledge of two material parameters: the Poisson ratio of the material, which relates strain induced lattice distortion perpendicular to its interface with the substrate to the relaxed lattice constant of the epi-layer material; and the variation in lattice constant of the unstrained alloy as a function of composition. The Poisson ratio and lattice constant for most binary III-V semiconductors are known with considerable accuracy. This was not, however the case for bulk AlAs at the beginning of these experiments. Due to the difficulty of growing bulk AlAs neither of these parameters was well defined for this material. Furthermore, the Poisson ratio of ternary materials has never been measured and no values for this parameter are available in the literature.

This chapter addresses the problem of relating DCXD mismatch measurements to the composition of ternary alloys. Since RHEED intensity oscillations can be used to accurately define the group III fluxes used for the MBE growth of $Al_xGa_{1-x}As$ layers, such layers are used to derive the Poisson ratio as a function of composition[3]. The results are then used to give the relationship between DCXD measurements and the composition of strained

on GaAs substrates and by analogy, the relationship for $In_xGa_{1-x}As$ and $In_xAl_{1-x}As$ on InP substrates.

2.2 The DCXD Technique

A typical arrangement for double crystal x-ray diffractometry (DCXD) is shown in Figure 2.1
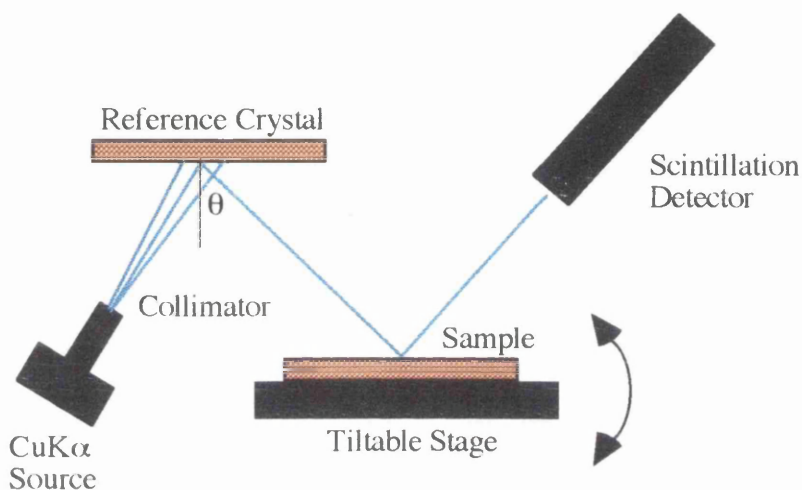
Figure 2.1. Schematic diagram of the arrangement for double crystal diffractometry (θ = Bragg angle).

The angle at which the incident beam strikes the specimen crystal is varied by a precision drive motor which tilts the stage upon which the specimen is mounted. The layer/substrate mismatch can be calculated from the angular separation of the diffraction peaks on an intensity versus angle plot known as a *rocking curve*. The breadth of the layer diffraction peak can also be used as an indication of the crystalline perfection of the layer.

The angular width of the Bragg peaks in a single crystal diffraction experiment is limited by the angular divergence of the incident beam. The scattering of X-ray crystals is weak so the angular range of Bragg reflection from a highly perfect crystal is typically of the order of a few seconds of arc. It is impractical to use slit collimators to reduce the beam divergence to this level so, in order to study small changes in lattice constant, the DCXD technique uses a reference crystal to condition the beam incident on the surface of the specimen crystal (see Figure 2.2).
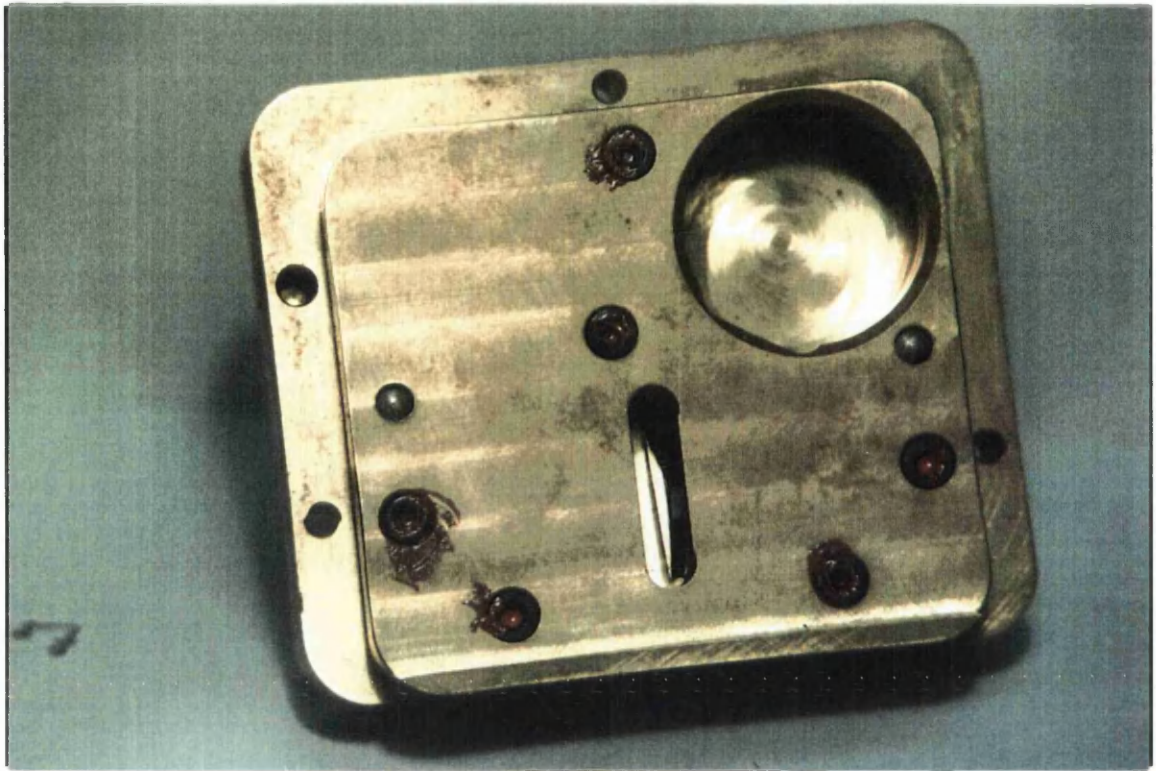
Figure 2.2. Reference crystal and mounting block from DCXD system.

Across the angular divergence of the collimator, X-rays of the different wavelength will satisfy the Bragg condition at different points across the reference crystal. Provided that the reference and specimen crystals are of the same material and the same reflection is used for both, when the crystals are accurately parallel then any ray satisfying the Bragg condition for the reference crystal will satisfy the Bragg condition for the sample crystal. The angular range over which Bragg reflection occurs is small so any angular displacement of the crystals will result in no diffracted signal from the specimen. It is essential that the tilt of the specimen is adjusted correctly to bring the diffraction vectors of the two crystals into the plane of incidence. Tilt misalignment causes a broadening of the rocking curve which is purely geometric in nature and becomes significant when examining pure crystals with narrow intrinsic peaks. The method commonly used to minimise tilt misalignment is to adjust the tilt position while searching for a maximum intensity position. Once the signal had been maximised, two measurements of peak splitting are recorded with the specimen rotated 180° about its surface normal to eliminate the effects of tilting[4].

2.3 Experimental

For thick, uniform layers the lattice mismatch can be calculated from the angular separation between the layer and substrate peaks. However, for thin (typically sub-micron) layers, 'substrate pulling'[5] produced by interaction between a thin layer and the substrate causes a shift in the DCXD layer peak position and the structure needs to be modelled by dynamical diffraction theory [6,7]. To avoid such effects the $Al_xGa_{1-x}As$ layers grown for this study were all at least 1μm thick. The composition of the samples was established using RHEED intensity oscillations at the commencement of growth[8]. Substrate temperatures were set to below 630°C to avoid loss of gallium through re-evaporation[9] and to ensure good surface morphology[10]. All of the layers were grown with the surface exhibiting the (001) - (2 x 4) As-stable reconstruction[11].

Characterisation of AlGaAs layers was undertaken using a Bede QC2 deskside double crystal diffractometer[12] (see Figure 2.3).

Figure 2.3. Bede QC2 deskside double crystal diffractometer.

The analysis software for this system assumes that the Poisson ratio for all As-containing ternary alloys is 0.33 regardless of composition, and that the relaxed lattice constant of a III_A-III_B-V alloy varies with the III_A-V fraction x according to Vergard's law i.e. :-

21

$$a = xa_A + (1\text{-}x)a_B \qquad\qquad (2.1)$$

where a, a_A , a_B are the lattice constants of the alloy, and the III_A-V and the III_B-V components respectively.

2.4 Results and Discussion

The lattice mismatch between layer and substrate can be calculated from the angular separation of the relevant peaks in the rocking curve using the equation for the Bragg condition :-

$$n\lambda = 2a\sin\theta \qquad\qquad (2.2)$$

where λ is the x-ray wavelength and θ is the Bragg angle. This equation can be differentiated to give the relationship between lattice mismatch and peak spacing :-

$$m^* = -\cot\theta\,\partial\theta \qquad\qquad (2.3)$$

where m^* represents the effective lattice mismatch and $\partial\theta$ represents the angular difference between the peaks. To calculate the relaxed mismatch m, the value obtained from the above equation has to be multiplied by an expression involving the Poisson ratio v, which relates horizontal lattice strain to the vertical lattice distortion measured by the DCXD technique:-

$$m = \frac{m^*(1-v)}{(1+v)} \qquad\qquad (2.4)$$

This value can be used to calculate the alloy composition of a ternary layer from Vergard's law.

To evaluate the Bede QC2 diffractometer, double axis rocking curves were measured for a series of $Al_xGa_{1\text{-}x}As$ of different x value. A typical rocking curve is given in Figure 2.4.

22
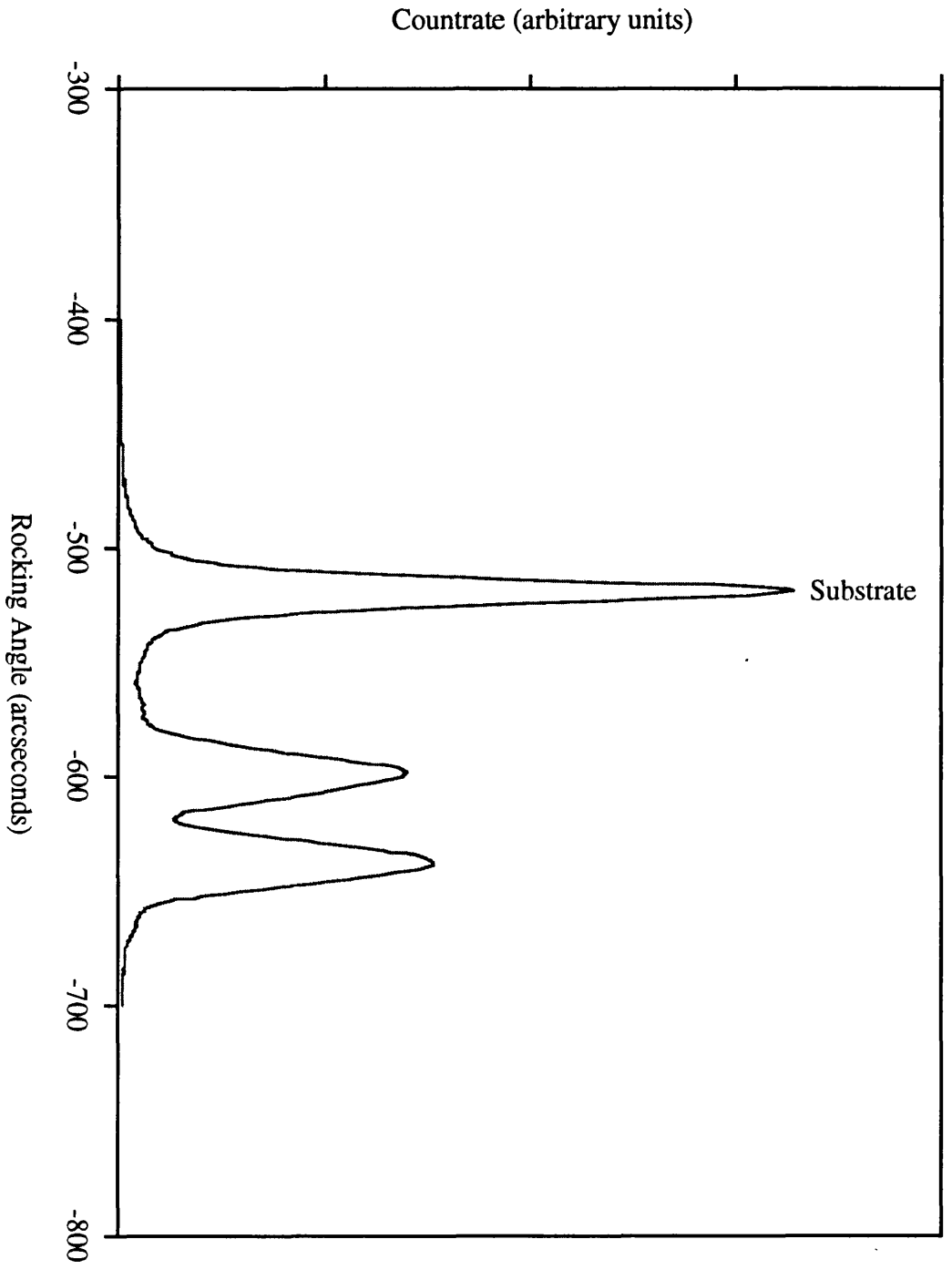
Figure 2.4. DCXD rocking curve for sample B103 containing 1μm of 20% AlGaAs and 1μm of 30% AlGaAs (as determined by RHEED).

The structure used for this example contained two layers of $Al_xGa_{1-x}As$ of different composition as shown in Figure 2.5.

$$\overset{o}{100A}\ GaAs\ cap$$

| $1\mu m$ AlGaAs x=0.3 |
| $1\mu m$ AlGaAs x=0.2 |
| GaAs substrate |
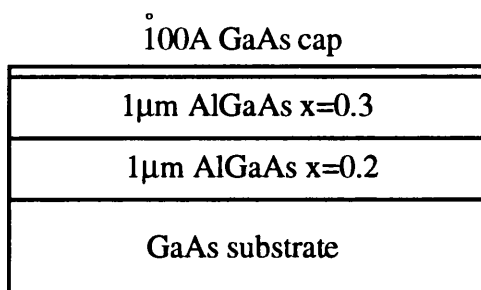
Figure 2.5. Structure for DCXD rocking curve shown in Figure 2.4

The results obtained for sample #B103, together with measurements for several other samples, showed a discrepancy between the composition calibrated by RHEED and the value derived from the rocking curve. The RHEED value was consistently smaller than the rocking curve value. This is illustrated in Figure 2.6, which shows the distribution of the error between the desired and measured composition for a series of nominally x=0.3 $Al_xGa_{1-x}As$ layers.
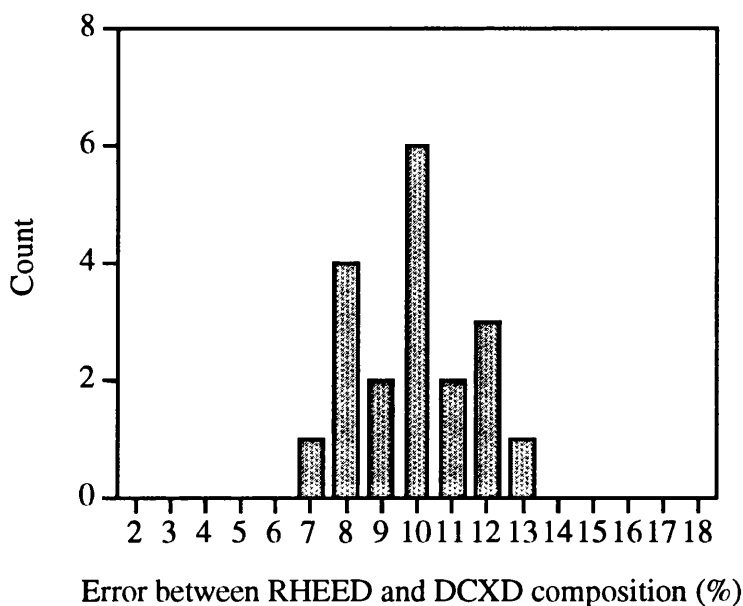
Figure 2.6. Distribution of the error between the desired and measured composition of a series of nominally x=0.3 $Al_xGa_{1-x}As$ layers.

The growth conditions were sufficiently well controlled for it to be unlikely that the layer compositions were in error. It was assumed that the problem was caused by inaccuracy of the value of Poisson ratio used to compensate for relaxation.

In an attempt to refine the accuracy of the measurements the assumption that v obeys Vergard's law was made. This gives the equation :-

$$v_{ternary} = (1 - x)v_A + xv_B \qquad (2.5)$$

or

$$v_{ternary} = v_A - x\Delta v \qquad (2.6)$$

where $\Delta v = v_A - v_B$. Substituting into equation 2.3 gives :-

$$|\Delta\theta| = \tan\theta \frac{m_r x(1 + v_A - x\Delta v)}{(1 - v_A + x\Delta v)} \qquad (2.7)$$

where m_r is the real mismatch between the binary components and is given by :-

$$m_r = \frac{a_B - a_A}{a_A} = \frac{m}{x} \qquad (2.8)$$

Equation 2.7 may be rewritten as :-

$$|\Delta\theta| = \tan\theta \frac{m_r xR(1 - x\Delta p)}{(1 + x\Delta q)} \qquad (2.9)$$

where

$$R = \frac{(1 + v_A)}{(1 - v_A)} \qquad \Delta p = \frac{\Delta v}{(1 + v_A)} \qquad \Delta q = \frac{\Delta v}{(1 - v_A)}$$

A binomial expansion of the last term in equation 2.9 yields a second order term in x :-

$$|\Delta\theta| = \{\tan\theta\}m_r xR \left[1 - \frac{2x\Delta v}{(1 - v_A^2)} \right] \qquad (2.10)$$

25

Thus the first and second order coefficients of a plot of $\Delta\theta$ versus x give unambiguous values of m_r and Δv, provided that the Poisson ratio v_A is known. In the case of the AlGaAs alloy v_A represents the Poisson ratio of GaAs which has been measured by a number of workers, most recently by Grimsditch $et\ al$ [13] using Brillouin scattering. From their measured values of c_{11} and c_{12}, which agree well with those of previous authors, it can be deduced that $v_{GaAs} = 0.311$. This is also the value used by Bassignana and Tan[14].

A quadratic function was fitted by the method of least squares to the measured peak splitting $\Delta\theta$ as a function of x. A good fit was achieved, in contrast to a linear function which gave a very poor representation of the data. From the first and second order coefficients of the quadratic fit it was found that $m_r = 1620$p.p.m ($\pm$ 1%) and $\Delta v = -0.04 \pm 0.01$, i.e. $v_{AlAs} = 0.27 \pm 0.01$.

The 1μm AlAs sample grown for this study did, however, have a poor surface morphology suggesting partial relaxation had occurred. Double axis diffractometry using asymmetric reflections was used to examine the AlAs epitaxial layer. This method provides a means of measuring the in-plane strain and hence the relaxation in an epitaxial layer. Rocking curves were recorded at the University of Durham using a Bede Model 150 diffractometer, from the four inclined (115) type planes, in both high and low angle of incidence, a total of 8 measurements. The data is summarised in Table 2.1. From the difference in the peak splitting on rotation of the wafer by 180° about its surface normal, the epitaxial layer was found to be tilted with respect to the substrate by 4±0.5 arcseconds in the [110] (0-180°) direction and 0±0.5 arcseconds in the [1$\bar{1}$0] direction.

Reflection	Sample Orientation	Mean Peak Separation (secs)	Tilt (secs)
115 Low	0-180°	676	4.5
115 Low	90-270°	679	0
115 High	0-180°	382	3.5
115 High	90-270°	381	0

Table 2.1. Asymmetric diffractometry data.

In the early stages of relaxation, inclined 60° dislocations are nucleated, the edge type Burgers vector components of which provide relaxation in the two orthogonal [110] directions in the specimen surface[15]. Due to the different dislocation mobilities on the A(g) and B(g) slip systems in III-V compounds, a mechanism for asymmetric relaxation in the two [110] directions thus exists. The

data in Table 2.1 can be used to determine the lattice parameter c normal to the specimen surface and the spacing of the two sets of (110) planes with their normals in the surface (see Table 2.2).

Parameter	0-180° Sample Orientation	90-270° Sample Orientation
c	5.66941Å (±0.00005Å)	5.66945Å
d_{110}	3.99802Å (±0.00004Å)	3.99787Å

Table 2.2. Layer lattice parameters deduced from asymmetric reflection diffractometry

In the calculation, a value of the GaAs lattice constant of 5.65375Å has been assumed, which is the mean value determined from synchrotron radiation Bond measurements by Usuda *et al* [16]. There is excellent agreement in Table 2.2 between the c parameters determined from the 0-180° data and the 90-270° data but a clear asymmetry of the in-plane strain exists. The mismatch deduced from the quadratic fit of the 004 symmetric reflection data gives the lattice parameter of totally relaxed AlAs as 5.66291 ± 0.00005Å. This is between the extreme values of 5.6605Å [17] and 5.670Å [18] found in the literature. Using this value the relaxation R can be deduced from the equation :-

$$R = (d_l\text{-}d_0)/(d_r\text{-}d_0) \qquad\qquad (2.11)$$

where d_l is the in-plane lattice parameter, d_r is the relaxed layer parameter, and d_0 is the substrate lattice parameter, in this case all referring to the (110) plane separation. For the [110] direction, this gives R_x = 3.3% and for the [1$\bar{1}$0] direction R_y = 1.0%.

The presence of relaxation was confirmed using X-ray topography [19], performed at the Daresbury Laboratory. This method images of the contours of lattice planes in crystal structures. Dislocations can be imaged since the intensity of the X-rays diffracted from the deformed planes differs from the intensity diffracted by the perfect crystal. To ensure maximum sensitivity, the sample is positioned at an angle corresponding to the steeply sloping side of the layer peak on the rocking curve. The experimental arrangement for double crystal reflection X-ray topography is shown schematically in Figure 2.7.
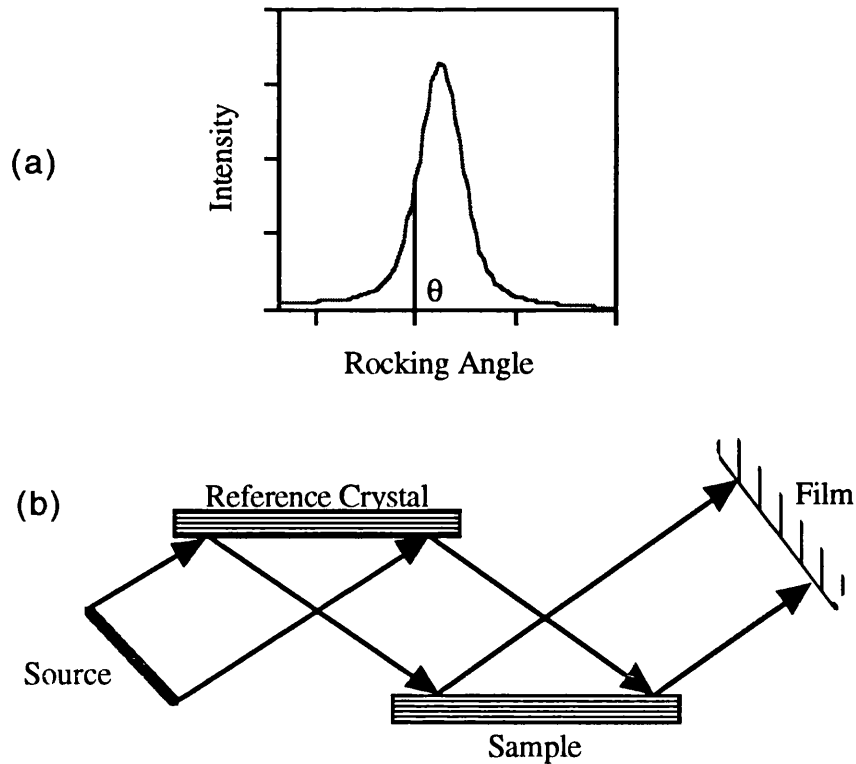
Figure 2.7. Double crystal X-ray topography technique. (a) Sample angle is adjusted to a position on the side of the diffraction peak to increase sensitivity. (b) Lattice distortions produce changes in the intensity of the diffracted beam which are detected on the photographic film.

A topograph of the AlAs layer is shown in Figure 2.8. The topographs were recorded on Ilford L4 nuclear emulsions in the surface symmetric 004 reflection at a wavelength of 1.882Å using a 111 silicon beam conditioner. The topograph of Figure 2.8 shows part of the dislocation network observed which varied in density from zero at the edge of the wafer to a maximum near the centre. At the spot where the rocking curves were recorded the misfit dislocation spacing was measured to be 11 ± 1 and 10 ± 2 μm respectively. In one direction the magnitude of the relaxation determined from the dislocation line density is in agreement with that deduced from the diffractometry. However, in the orthogonal direction, the misfit dislocation density is significantly lower than predicted by diffractometry. This may be ascribed to the bunching of misfit dislocations such that the individual dislocations are not resolved within the resolution limit of X-ray topography.
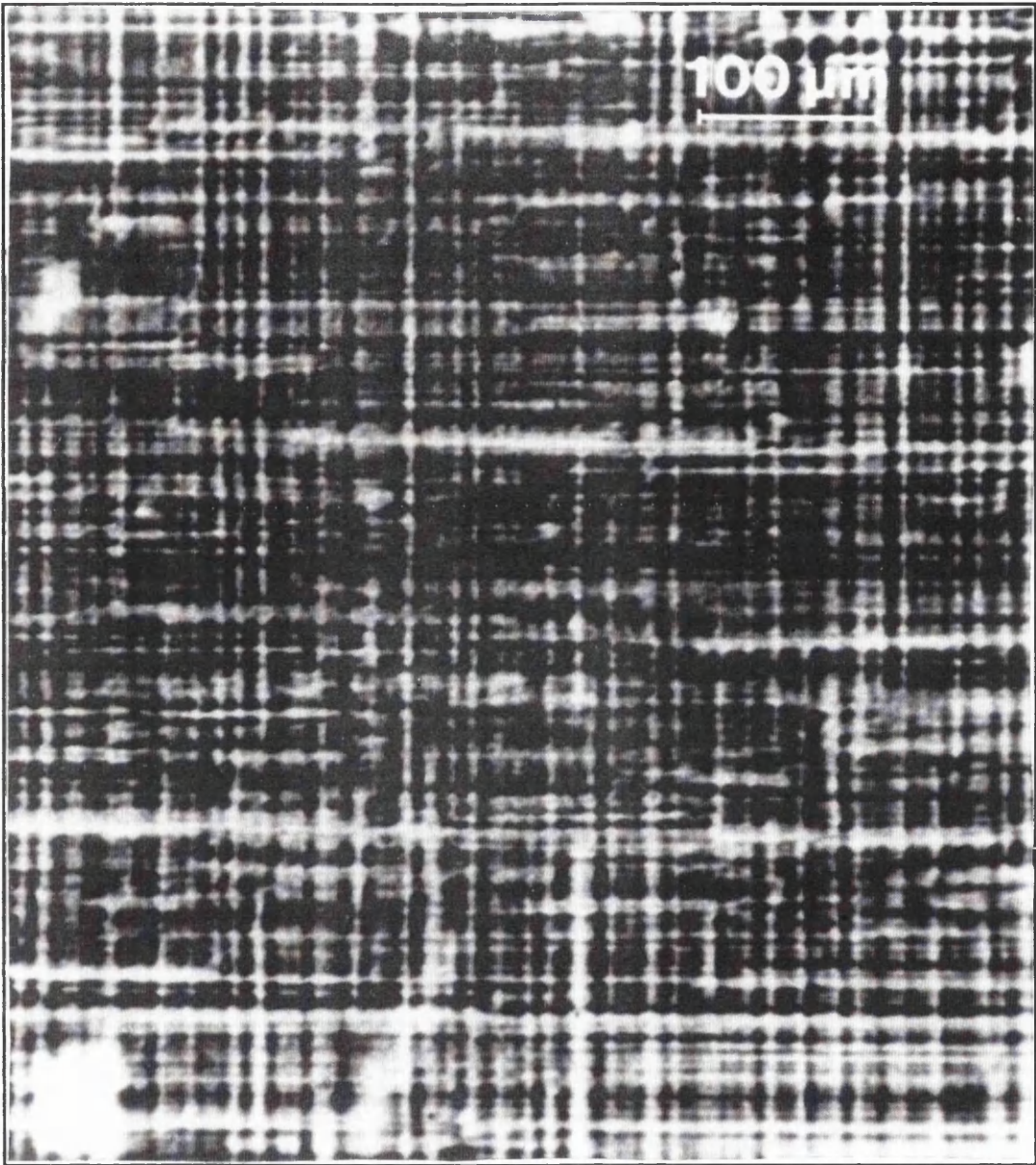
Figure 2.8. X-ray topograph of misfit dislocation network in 1μm thick AlAs layer
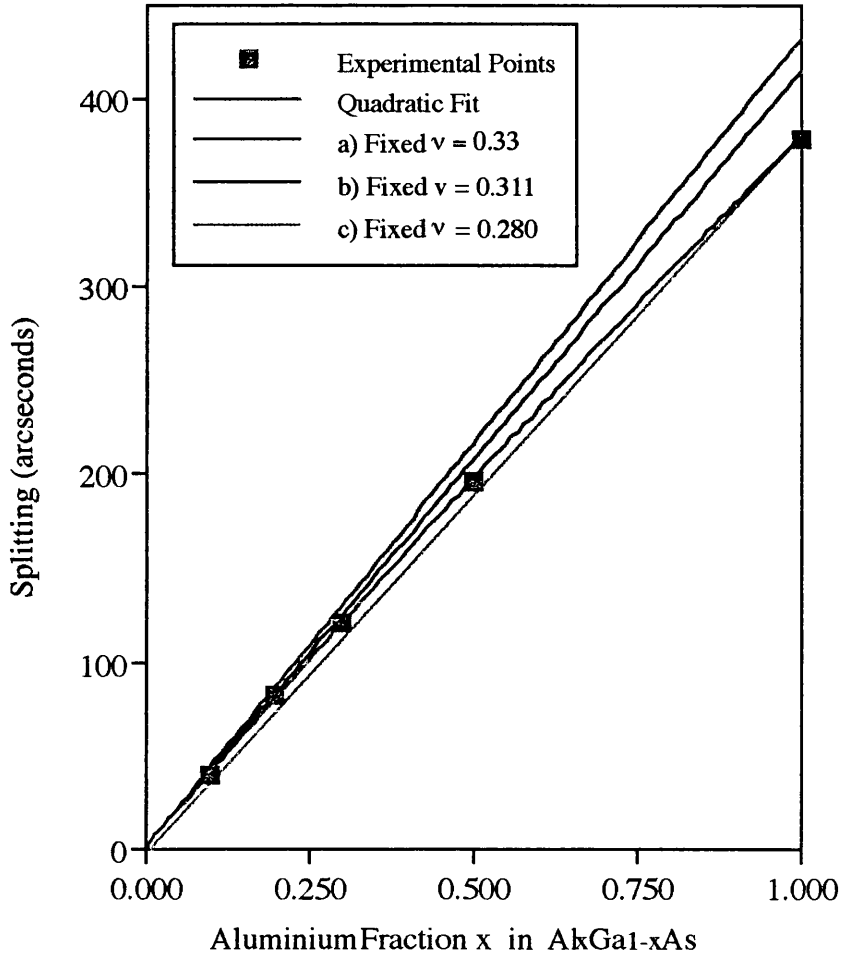
Figure 2.9. Rocking curve peak splitting vs aluminium composition x using data corrected for relaxation. The solid line is a least squares fit to the data. The dashed lines indicate linear fits for Poisson ratios of a) 0.33 the original value used by the Bede software, b) 0.311 the GaAs value and c) 0.28 the derived AlAs value

For a mismatch of 1620ppm, the rocking curve peak splitting for a 100% relaxed layer is 218 arcseconds. The strain in the (001) direction ε_{zz} is related to the orthogonal strains ε_{xx} and ε_{yy} in the plane by :-

$$\varepsilon_{zz} = -2\nu\frac{\varepsilon_{xx}(1-R_x) + \varepsilon_{yy}(1-R_y)}{1-\nu} \tag{2.12}$$

Thus as ε_{zz} is proportional to the mean of the orthogonal relaxations R_x and R_y (2.2% in this case), the calculated splitting is 379±1arcseconds for a thick, but unrelaxed AlAs layer on GaAs. When this value for the x = 1 point is used to fit a quadratic function (see Figure 2.9), the first and second order coefficients are found to be 409 and -29.5 arcseconds respectively. This correction gives the best

30

fit value of the GaAs to AlAs mismatch of 1600p.p.m. (±1%) and a value of 0.28±0.01 for the AlAs Poisson ratio. These values are in excellent agreement with an independent study (published at the same time as the results of this work[3]) by Goorsky *et al* [20] , who used photoluminescence and electron microprobe analysis to compare with X-ray diffraction data.

2.5 Conclusions

The variation of Poisson ratio with $Al_xGa_{1-x}As$ alloy composition can be calculated from the equation :-

$$v_{Al_xGa_{1-x}As} = 0.28x + 0.311(1-x) \qquad (2.14)$$

Linear fits which do not take this dependence into account are inaccurate and result in discrepancies between the measured and predicted compositions. The dependence of Poisson ratio on alloy composition means that the DCXD splitting is related to the composition by a quadratic of the form :-

$$\Delta\theta = -29.5x^2 + 409x \quad \text{arcseconds} \qquad (2.15)$$

Calculation of composition from a measured splitting is therefore not completely straightforward. It is necessary to perform self-consistent calculations or use a look-up table to derive the alloy composition from the measured splitting. Calculated splittings for a range of $Al_xGa_{1-x}As$ compositions are shown in Table 2.3.

X	$|\Delta\theta|$	X	$|\Delta\theta|$	X	$|\Delta\theta|$
0.005	2.0	0.205	82.6	0.405	160.8
0.01	4.1	0.21	84.6	0.41	162.7
0.015	6.1	0.215	86.6	0.415	164.7
0.02	8.2	0.22	88.6	0.42	166.6
0.025	10.2	0.225	90.5	0.425	168.5
0.03	12.2	0.23	92.5	0.43	170.4
0.035	14.3	0.235	94.5	0.435	172.3
0.04	16.3	0.24	96.5	0.44	174.2
0.045	18.3	0.245	98.4	0.445	176.2
0.05	20.4	0.25	100.4	0.45	178.1
0.055	22.4	0.255	102.4	0.455	180.0
0.06	24.4	0.26	104.3	0.46	181.9
0.065	26.5	0.265	106.3	0.465	183.8
0.07	28.5	0.27	108.3	0.47	185.7
0.075	30.5	0.275	110.2	0.475	187.6
0.08	32.5	0.28	112.2	0.48	189.5
0.085	34.6	0.285	114.2	0.485	191.4
0.09	36.6	0.29	116.1	0.49	193.3
0.095	38.6	0.295	118.1	0.495	195.2
0.1	40.6	0.3	120.0	0.5	197.1
0.105	42.6	0.305	122.0	0.525	206.6
0.11	44.6	0.31	124.0	0.55	216.0
0.115	46.6	0.315	125.9	0.575	225.4
0.12	48.7	0.32	127.9	0.6	234.8
0.125	50.7	0.325	129.8	0.625	244.1
0.13	52.7	0.33	131.8	0.65	253.4
0.135	54.7	0.335	133.7	0.675	262.6
0.14	56.7	0.34	135.6	0.7	271.8
0.145	58.7	0.345	137.6	0.725	281.0
0.15	60.7	0.35	139.5	0.75	290.2
0.155	62.7	0.355	141.5	0.775	299.3
0.16	64.7	0.36	143.4	0.8	308.3
0.165	66.7	0.365	145.4	0.825	317.3
0.17	68.7	0.37	147.3	0.85	326.3
0.175	70.7	0.375	149.2	0.875	335.3
0.18	72.7	0.38	151.2	0.9	344.2
0.185	74.7	0.385	153.1	0.925	353.1
0.19	76.6	0.39	155.0	0.95	361.9
0.195	78.6	0.395	157.0	0.975	370.7
0.2	80.6	0.4	158.9	1	379.5

Table 2.3. Splitting in arcseconds for a range of $Al_xGa_{1-x}As$ alloy compositions.

The parameters derived for AlAs can be used to extend the principle of scaling the Poisson ratio using Vergard's Law to the calculation of InGaAs and AlInAs compositions around the lattice matched condition. The Poisson ratio for

InAs is well defined and has a value of 0.352^{14}. This value gives a relationship between the composition of $In_xGa_{1-x}As$ and peak splitting of the form :-

$$\Delta\theta = 1620.0x^2 + 15840.9x - 8891.8 \qquad (2.14)$$

Similarly the equation relating composition and peak splitting for $In_xAl_{1-x}As$ is :-

$$\Delta\theta = 2666.2x^2 + 13806.7x - 7923.0 \qquad (2.15)$$

These relationships are shown graphically in Figure 2.9.
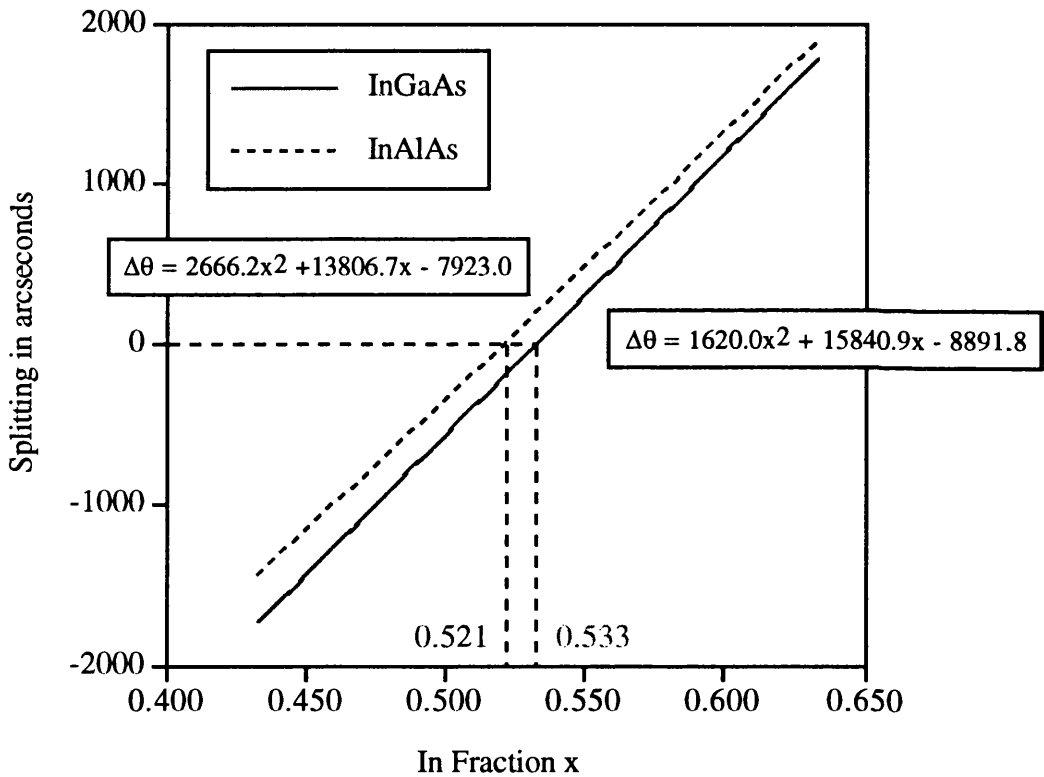
Figure 2.10. Calculated rocking curve peak splitting as a function of In fraction x for $In_xAl_{(1-x)}As$ and $In_xGa_{(1-x)}As$ on InP. Both curves assume v varies according to Vergard's law and the $In_xAl_{(1-x)}As$ curve assumes the AlAs lattice parameter and Poisson ratio have the previously derived values.

Look-up tables enabling the composition of $In_{0.53}Ga_{0.47}As$ and $In_{0.52}Al_{0.48}As$ on InP to be determined for a given DCXD peak splitting are given in Tables 2.4 and 2.5 respectively. These tables allow a more accurate

determination of composition than is possible using existing data, and they have been used extensively in work described in later chapters.

X	$\Delta\theta$	X	$\Delta\theta$	X	$\Delta\theta$
0.433	-1729.0	0.513	-339.1	0.553	363.6
0.435	-1694.5	0.514	-321.6	0.555	398.9
0.437	-1660.0	0.515	-304.1	0.557	434.1
0.439	-1625.5	0.516	-286.6	0.559	469.4
0.441	-1591.0	0.517	-269.1	0.561	504.7
0.443	-1556.4	0.518	-251.6	0.563	540.1
0.445	-1521.8	0.519	-234.0	0.565	575.4
0.447	-1487.3	0.52	-216.5	0.567	610.8
0.449	-1452.7	0.521	-199.0	0.569	646.1
0.451	-1418.1	0.522	-181.5	0.571	681.5
0.453	-1383.5	0.523	-163.9	0.573	716.9
0.455	-1348.8	0.524	-146.4	0.575	752.3
0.457	-1314.2	0.525	-128.8	0.577	787.7
0.459	-1279.5	0.526	-111.3	0.579	823.1
0.461	-1244.9	0.527	-93.8	0.581	858.6
0.463	-1210.2	0.528	-76.2	0.583	894.0
0.465	-1175.5	0.529	-58.6	0.585	929.5
0.467	-1140.8	0.53	-41.1	0.587	965.0
0.469	-1106.1	0.531	-23.5	0.589	1000.5
0.471	-1071.4	0.532	-6.0	0.591	1036.0
0.473	-1036.6	0.533	11.6	0.593	1071.5
0.475	-1001.9	0.534	29.2	0.595	1107.0
0.477	-967.1	0.535	46.7	0.597	1142.6
0.479	-932.3	0.536	64.3	0.599	1178.1
0.481	-897.5	0.537	81.9	0.601	1213.7
0.483	-862.7	0.538	99.5	0.603	1249.3
0.485	-827.9	0.539	117.1	0.605	1284.9
0.487	-793.1	0.54	134.6	0.607	1320.5
0.489	-758.2	0.541	152.2	0.609	1356.1
0.491	-723.4	0.542	169.8	0.611	1391.7
0.493	-688.5	0.543	187.4	0.613	1427.4
0.495	-653.6	0.544	205.0	0.615	1463.1
0.497	-618.7	0.545	222.6	0.617	1498.7
0.499	-583.8	0.546	240.2	0.619	1534.4
0.501	-548.9	0.547	257.9	0.621	1570.1
0.503	-514.0	0.548	275.5	0.623	1605.8
0.505	-479.0	0.549	293.1	0.625	1641.6
0.507	-444.1	0.55	310.7	0.627	1677.3
0.509	-409.1	0.551	328.3	0.629	1713.1
0.511	-374.1	0.552	346.0	0.631	1748.8

Table 2.4. Splitting in arcseconds for a range of $In_xGa_{(1-x)}As$ alloy compositions.

X	Δθ
0.422	-1621.9
0.424	-1589.8
0.426	-1557.6
0.428	-1525.5
0.43	-1493.3
0.432	-1461.0
0.434	-1428.8
0.436	-1396.5
0.438	-1364.2
0.44	-1331.9
0.442	-1299.6
0.444	-1267.3
0.446	-1234.9
0.448	-1202.5
0.45	-1170.1
0.452	-1137.7
0.454	-1105.2
0.456	-1072.7
0.458	-1040.2
0.46	-1007.7
0.462	-975.2
0.464	-942.6
0.466	-910.1
0.468	-877.5
0.47	-844.8
0.472	-812.2
0.474	-779.5
0.476	-746.9
0.478	-714.2
0.48	-681.4
0.482	-648.7
0.484	-615.9
0.486	-583.1
0.488	-550.3
0.49	-517.5
0.492	-484.6
0.494	-451.8
0.496	-418.9
0.498	-386.0
0.5	-353.0

X	Δθ
0.502	-320.1
0.503	-303.6
0.504	-287.1
0.505	-270.6
0.506	-254.1
0.507	-237.6
0.508	-221.1
0.509	-204.6
0.51	-188.1
0.511	-171.5
0.512	-155.0
0.513	-138.5
0.514	-121.9
0.515	-105.4
0.516	-88.8
0.517	-72.2
0.518	-55.7
0.519	-39.1
0.52	-22.5
0.521	-6.0
0.522	10.6
0.523	27.2
0.524	43.8
0.525	60.4
0.526	77.0
0.527	93.6
0.528	110.3
0.529	126.9
0.53	143.5
0.531	160.1
0.532	176.8
0.533	193.4
0.534	210.1
0.535	226.7
0.536	243.4
0.537	260.1
0.538	276.7
0.539	293.4
0.54	310.1
0.541	326.8

X	Δθ
0.542	343.5
0.544	376.9
0.546	410.3
0.548	443.7
0.55	477.2
0.552	510.7
0.554	544.2
0.556	577.7
0.558	611.3
0.56	644.8
0.562	678.4
0.564	712.1
0.566	745.7
0.568	779.4
0.57	813.0
0.572	846.7
0.574	880.5
0.576	914.2
0.578	948.0
0.58	981.8
0.582	1015.6
0.584	1049.4
0.586	1083.3
0.588	1117.1
0.59	1151.0
0.592	1184.9
0.594	1218.9
0.596	1252.8
0.598	1286.8
0.6	1320.8
0.602	1354.9
0.604	1388.9
0.606	1423.0
0.608	1457.1
0.61	1491.2
0.612	1525.3
0.614	1559.5
0.616	1593.7
0.618	1627.9
0.62	1662.1

Table 2.5. Splitting in arcseconds for a range of $In_xAl_{(1-x)}As$ alloy compositions.

2.6 References

1 'X-Ray Topography and Precision Diffractometry of Semiconducting
  Materials'
  B.K. Tanner
  Journal Of The Electrochemical Society 1989 Vol.136 No.11 pp.3438-3443

2 ' High-Resolution X-Ray-Diffraction And Topography For Crystal
  Characterization'
  B.K. Tanner
  Journal Of Crystal Growth 1990 Vol.99 No.14 pp.1315-1323

3 'Measurement of Aluminum Concentration in Epitaxial Layers of $Al_xGa_{1-x}As$
  on GaAs by Double Axis X-Ray-Diffractometry'
  B.K. Tanner, A.G. Turnbull, C.R. Stanley, A.H. Kean and M. McElhinney
  Applied Physics Letters 1991 Vol.59 No.18 pp.2272-2274

4 'Measurement of Aluminum Concentration in $Al_xGa_{1-x}As$ Epitaxial Layers by
  Double-Axis X-Ray-Diffraction'
  B.K. Tanner, S.J. Miles, G.G. Peterson and R.N. Sacks
  Materials Letters 1988 Vol.7 No.5 pp.239-241

5 'Rocking Curve Peak Shift in Thin Semiconductor Layers'
  C.R. Wie
  Journal Of Applied Physics 1989 Vol.66 No.2 pp.985-988

6 'Composition and Lattice-Mismatch Measurement of Thin Semiconductor
  Layers by X-Ray-Diffraction'
  P.F. Fewster and C.J. Curling
  Journal Of Applied Physics 1987 Vol.62 No.10 pp.4154-4158

7 'Principles and Performance of a PC-Based Program for Simulation of
  Double-Axis X-Ray Rocking Curves of Thin Epitaxial-Films'
  D.K. Bowen, N. Loxley, B.K. Tanner, L. Cooke and M.A. Capano
  Materials Research Society Symposium Proceedings: Advances In Surface
  and Thin Film Diffraction 1991 Vol.208 pp48-50

8 'Dynamics of Film Growth of GaAs By MBE from RHEED Observations'
J.H. Neave, B.A. Joyce, P.J. Dobson, N. Norton
Applied Physics A-Solids And Surfaces 1983 Vol.31 No.1 pp.1-8

9 'Incorporation Rates of Gallium and Aluminum on GaAs During Molecular-Beam Epitaxy at High Substrate Temperatures'
R. Fischer, J. Klem, T.J. Drummond, R.E. Thorne, W. Kopp, H. Morkoc, A.Y. Cho
Journal Of Applied Physics 1983 Vol.54 No.5 pp.2508-2510

10 'Investigation of Surface-Roughness of Molecular-Beam Epitaxy $Al_xGa_{1-x}As$ Layers and Its Consequences on GaAs/$Al_xGa_{1-x}As$ Heterostructures
F. Alexandre, L. Goldstein, G. Leroux, M.C. Joncour, H. Thibierge and E.V.K Rao
Journal Of Vacuum Science & Technology B-Microelectronics Processing and Phenomena 1985 Vol.3 No.4 pp.950-955

11 'Bonding Direction and Surface-Structure Orientation on GaAs (001)'
A.Y. Cho
Journal of Applied Physics 1976 Vol.47 No.7 pp2841-2843

12 'Application of a Desk-Side Double-Axis X-Ray Diffractometer for Very Large Area Epilayer Characterization'
N. Loxley, D.K. Bowen, B.K. Tanner
Materials Research Society Symposium Proceedings: Advances In Surface and Thin Film Diffraction 1991 Vol.208 pp.119-124

13 'Elastic Properties Of GaAs/AlAs Superlattices'
M. Grimsditch, R. Bhadra, I.K. Schuller, F. Chambers, G. Devane
Physical Review B-Condensed Matter 1990 Vol.42 No.5 pp.2923-2925

14 'Determination of Epitaxic-Layer Composition and Thickness by Double-Crystal X-Ray-Diffraction'
I.C. Bassignana, C.C. Tan
Journal of Applied Crystallography 1989 Vol.22 pp.269-276

15 'Asymmetric Relaxation in Epitaxial Layers of III-V Compounds'
    A.G. Turnbull, G.S. Green, B.K. Tanner, M.A.G. Halliwell
    Evolution of Thin-Film and Surface Microstructure 1991 Vol.202 pp.513-518

16 'Lattice-Parameter Measurement of GaAs Crystals Using Monochromatic
    Synchrotron Radiation'
    K. Usuda, S. Yasuami, Y. Higashi, H. Kawata, M. Ando
    Japanese Journal Of Applied Physics Part 2-Letters 1990 Vol.29 No.2
    pp272-274

17 'Physics of Semiconductor Devices'
    S.M. Sze
    (New York, Wiley, 1981) p848

18 JCPDS Powder Diffraction File
    JCPDS International Centre for Diffraction Data
    Swarthmore, PA, USA (1986)

19 'X-ray Diffraction Topography'
    B. K. Tanner
    (Oxford, Pergamon Press, 1976)

20 'Determination Of Epitaxial $Al_xGa_{1-x}As$ Composition from X-Ray-
    Diffraction Measurements'
    M.S. Goorsky, T.F. Kuech, M.A. Tischler, R.M. Potemski
    Applied Physics Letters 1991 Vol.59 No.18 pp.2269-2271

Chapter 3

Analysis of the Homo-Epitaxial Growth of InAs by MBE

3.1 Introduction

The range of growth conditions used for the MBE growth of ternary and quaternary alloys are, in general, determined by the stability of the most volatile III-V pseudo-binary component of the alloy. In the case of $Al_xGa_{1-x}As$, it has been shown that the maximum permissible substrate temperature (T_S) for the growth of AlGaAs is limited by Ga evaporation from the surface of the alloy, which prevents accurate control of the composition[1,2,3,4,5].

Conditions for the growth of In(Al,Ga)As alloys will be dominated by the behaviour of the InAs component. An understanding of the growth processes involved in the homoepitaxial growth of InAs is therefore necessary to understand properly the behaviour of the In(Al,Ga)As alloys, and explain the restricted range of conditions which can be used to grow these alloys.

It has been demonstrated that InAs RHEED intensity oscillations can be used to calibrate the indium flux for the growth of In(Al,Ga)As alloys[6]. Under certain circumstances this technique results in an underestimation of the actual In flux[7], which is due to a reduction in the incorporation of In under notionally (2x4) As-stable conditions. Confident calculation of the actual In flux requires that the conditions for this reduced In incorporation be recognised and eliminated.

In this chapter RHEED intensity oscillations are used to study the conditions necessary for the homo-epitaxial growth of InAs. This work arose out of the need to establish repeatable conditions for the growth of $In_{0.53}Ga_{0.47}As$ and $In_{0.52}Al_{0.48}As$ lattice matched to InP. The determination of the 'envelope' of possible growth conditions for InAs was found to be a pre-requisite for further work on ternary materials. The experimental results presented in this chapter are shown to be in good agreement with a theoretical treatment developed from the thermodynamic model proposed by Heckingbottom $et\,al$ [8], and it is shown in Chapter 4 that the arguments used here can be expanded to encompass the MBE growth of lattice matched ternary materials.

3.2 Experimental procedures

Surface symmetries were examined by RHEED, with the electron beam incident on the wafer at a glancing angle of $\approx 2°$ along either the [1$\bar{1}$0] or [110] azimuth of the (100) surface. The growth rate of InAs was measured by RHEED intensity oscillations from a 5 x 5mm^2 (100)-InAs sample. Intensity variations of the specular spot were detected with an optical fibre and photomultiplier tube whose output was connected via a transimpedance amplifier either directly to a chart recorder or into a computer for data analysis. The cracking section of the arsenic sources on the MBE system was maintained at a temperature of 700°C estimated to produce a cracking efficiency of >95%[9]. Substrate temperatures were measured with an Ircon series V optical pyrometer.

3.3. Experimental Results

3.3.1 Arsenic Incorporation as a Function of Substrate Temperature

The sticking coefficient of arsenic dimers (S_{As_2}) on GaAs substrates has been shown by Foxon et al [10] to approach unity for the conditions normally used in the growth of GaAs. The sticking coefficient of As_2 on an InAs growth surface can, therefore, be evaluated by comparing the As limited growth rate of GaAs with that of InAs for an identical incident As_2 flux.

For GaAs growth, the transition between Ga- and As-limited growth for a fixed As_2 flux was obtained by increasing the Ga cell temperature (T_{Ga}) until a change from an As-stable (2×4) to a Ga-stable (4×2) reconstruction was obtained. The change in reconstruction pattern was accompanied by a characteristic change from an exponential relationship between T_{Ga} and the growth rate (G_r) measured by RHEED, to a regime where G_r was independent of the Ga cell temperature[11]. This can clearly be seen in Figure 3.1 which plots G_r as a function of T_{Ga}. The substrate temperature (T_s) during these measurements was maintained at 540°C to ensure maximum As incorporation[12]. The As limited growth rate at this substrate temperature, and for the As_2 flux density used in this experiment, was found to be 2.15μm/hr corresponding to an incorporating As_2 flux density of 6.6×10^{14} molecules/cm^2.

In the case of InAs the reconstruction observed by RHEED during growth at low substrate temperatures ($\approx 450°C$) was a (2×4) pattern similar to that observed during the growth of GaAs under Ga- limited growth conditions[13].
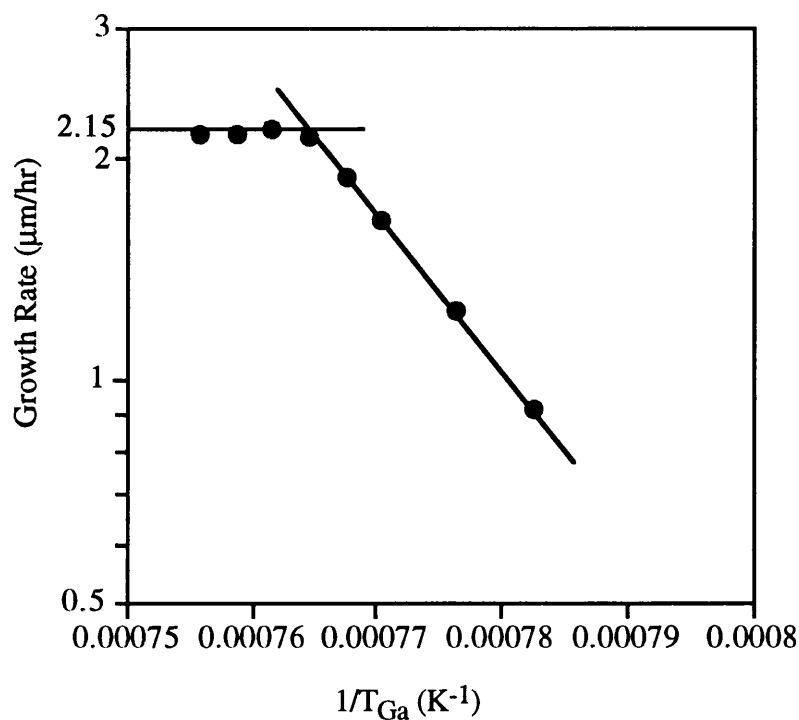
Figure 3.1. GaAs growth rate measured by RHEED oscillations vs reciprocal of gallium cell temperature for a substrate temperature of 540°C and an As_2 flux density of 6.6×10^{14} molecules/cm^2.

The growth rate and surface reconstruction of InAs were similarly measured for an increasing indium furnace temperature (T_{In}) while the As flux density was maintained at the 6.6×10^{14} molecules/cm^{2}s value used for the GaAs measurements. At low substrate temperatures the growth was controlled by the In flux and the surface reconstruction was an As stable (2×4) pattern similar to that observed during the growth of GaAs under gallium limited growth conditions. The growth rate rose with increasing indium furnace temperature (and hence increasing indium flux) until, eventually, a temperature was reached above which the growth rate remained constant. At this point the RHEED pattern became an In-stable (4×2) reconstruction indicating that a transition from In-limited to As-limited growth[14] had taken place. The growth rate as a function of T_{In} is shown in Figure 3.2 for a range of T_S. The behaviour is broadly similar to that observed for GaAs with a switch to an As-limited growth regime where G_r is independent of T_{In}. There is however, for a given In cell temperature in the regime of In-limited growth, a spread in the measured growth rates with T_S. This is not seen in the case of GaAs and indicates a dependence of growth rate on T_S which will be examined in detail later.

41
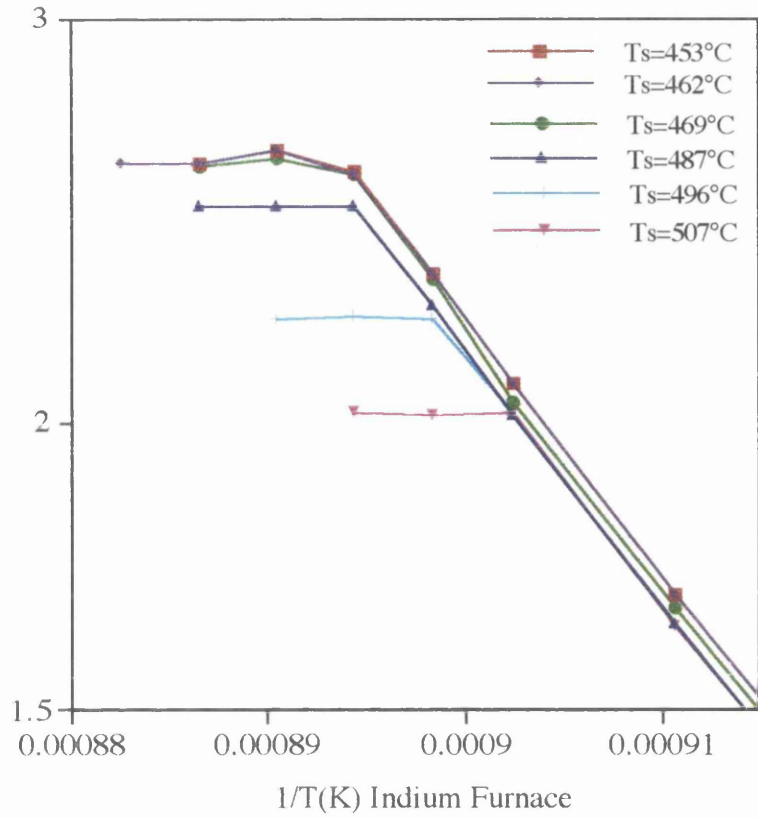
Figure 3.2. Arrhenius plot of growth rate vs reciprocal of indium furnace thermocouple temperature.
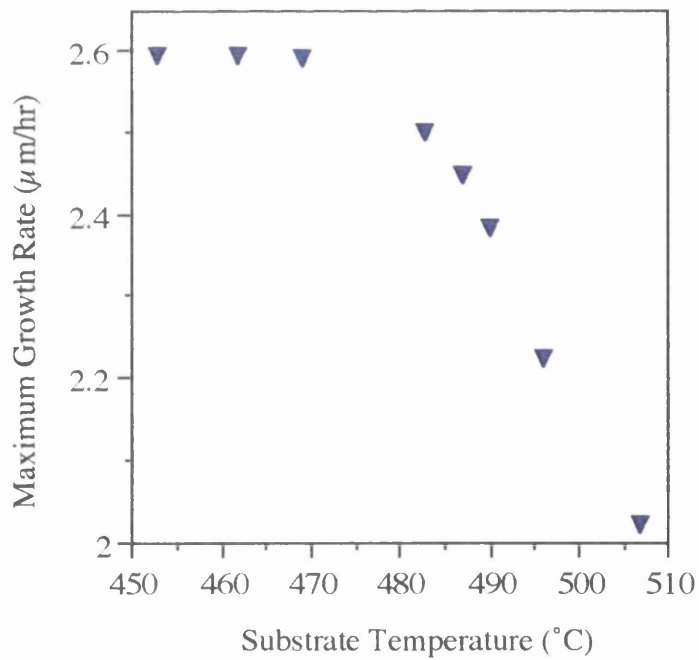
Figure 3.3. G_r^{max} vs T_S for the homoepitaxial growth of InAs.

The dependence of the growth rate in the As-limited regime (G_r^{max}) on substrate temperature is shown in Figure 3.3. G_r^{max} remains constant at 2.60μm/hr for T_S < 470°C. Above 470°C, G_r^{max} decreases with increasing T_S, reflecting a reduction in S_{As_2}. The value of G_r^{max} for the growth of InAs at T_S < 470°C of 2.60μm/hr should be compared with the figure of 2.15μm/hr obtained for the growth of GaAs. The difference is entirely accounted for by the larger lattice constant of InAs. If the maximum sticking coefficient of As_2 on InAs is the same as on GaAs then the ratio between the growth rates should be given by the ratio of the cubes of the individual lattice constants. ie :-

$$\frac{a_{InAs}^{3}}{a_{GaAs}^{3}} = \frac{6.05838^{3}}{5.65325^{3}} = 1.23 \qquad (3.1)$$

The ratio of maximum growth rates obtained experimentally is 1.20 which confirms that the maximum sticking coefficients of arsenic dimers on InAs and GaAs are similar. The minimum arsenic flux density required for the growth of InAs at low T_S is therefore approximately equal to half of the indium flux density.

3.3.2 InAs Growth Rate as a Function of Substrate Temperature

It has been observed[15] that an intermediate stage of InAs growth exists where, although the reconstruction remains (2 ×4), droplets of liquid indium are observed on the surface after growth. This surface indium accretion regime represents a range of 'forbidden' substrate temperatures which produce material with poor morphology. Growth on either side of this regime produces mirror smooth surfaces although the best quality material is grown in the higher temperature, indium stable regime[16]. The onset of indium accretion cannot easily be discerned from examination of the RHEED reconstruction pattern which remains a clear (2 ×4) throughout and is largely unaffected by the surface indium droplets: however, close examination of RHEED growth rate measurements made at increasing substrate temperatures reveals a step reduction in the measured growth rate. This is illustrated in Figure 3.4.
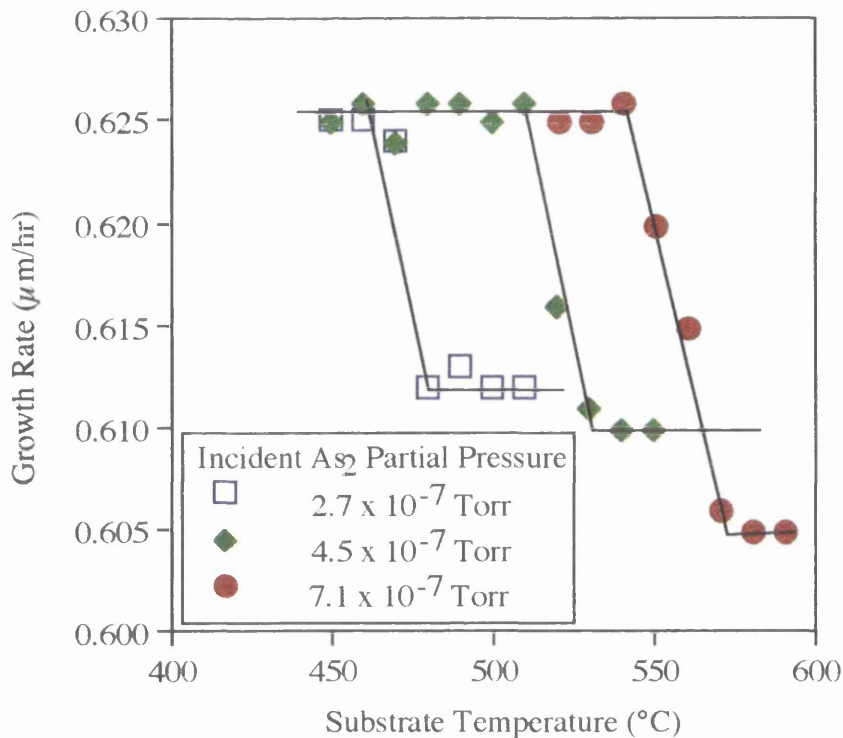
Figure 3.4. Measured growth rate vs substrate temperature for the growth of InAs for three different values of incident arsenic partial pressures.

The growth rate alternates between two stable plateau regions about some critical substrate temperature defined as T_C. Below T_C the growth rate is constant at a value corresponding to the incident indium flux, in this case $0.625\mu m/hr$ but, as the substrate temperature is raised above T_C, the growth rate falls to a lower value, and remains stable at this new level until the onset of desorption. The important point is that the value of T_C is influenced by the arsenic pressure used for the growth. The pressures quoted in Figure 3.4 are not direct BEP pressure readings, but have instead been calculated by scaling the minimum BEP collector current reading for growth at low substrate temperatures where arsenic desorption is minimal.

Typical oscillations obtained during the growth rate measurements are shown in Figure 3.5. The drop in growth rate at T_C appears to correlate with a change in the behaviour of the RHEED oscillations themselves. At temperatures below T_C the intensity rises sharply at the commencement of growth. As the substrate temperature is increased towards T_C the magnitude of this initial rise is reduced. When T_S is approximately equal to T_C the initial rise disappears entirely and the intensity of the specular spot falls when the indium shutter is opened. The origin of this initial rise is unclear but appears to consistently co-incide with growth at temperatures below T_C.
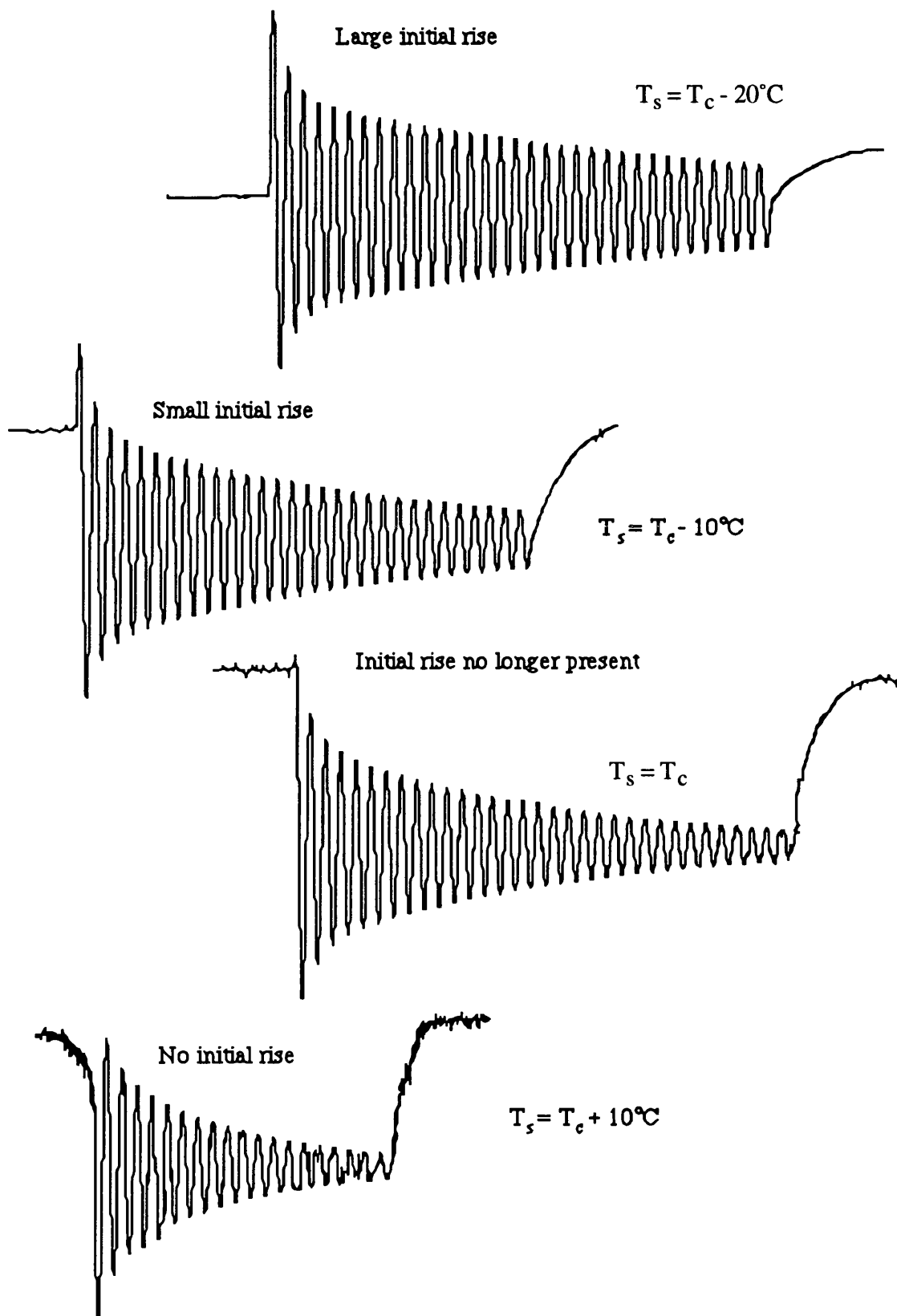
Figure 3.5. RHEED intensity oscillations obtained for the homoepitaxial growth of InAs. The disappearance of the initial rise observed in the intensity of the specular spot appears to be linked to the onset of indium droplet formation. These oscillations were recorded with constant diffraction geometry, and only the substrate temperature was changed.

3.4 Discussion

If the upper plateau regions of Figure 3.4 are assumed to represent complete incorporation of incident indium, then the apparent drop in growth rate as the substrate temperature is increased represents a real reduction in the amount of incorporating indium. The transition from 2D nucleation to step flow growth has been reported by Joyce et al[17] to cause a reduction in the measured rate of change of step density without any real reduction in the growth rate. This effect does not explain the second regime of constant growth rate for $T_S > T_C$. Observations of the RHEED reconstruction during growth with $T_S > T_t$ confirm that the measured drop in G_r is real. Although there is no immediate change in the RHEED reconstruction during growth, the pattern fades noticeably after ≈ 15 minutes ($\approx 0.15 \mu m$) and shows the arrowhead-like diffraction spots normally associated with facetted growth. This behaviour is typical of growth in the regime where indium is accumulating on the surface.

The RHEED oscillation technique monitors the change in average surface step density with time and the period of the oscillation should be unaffected by the presence of small droplets where the surface 'roughness' is constant. This is, however, only true if there is no interaction between the droplets and the growth surface. From the drop in growth rate it appears that the droplets, once formed, act as sinks for a proportion of the indium adatom population, reducing the fraction of the incident In flux contributing to the nett growth. This is illustrated in Figure 3.6.
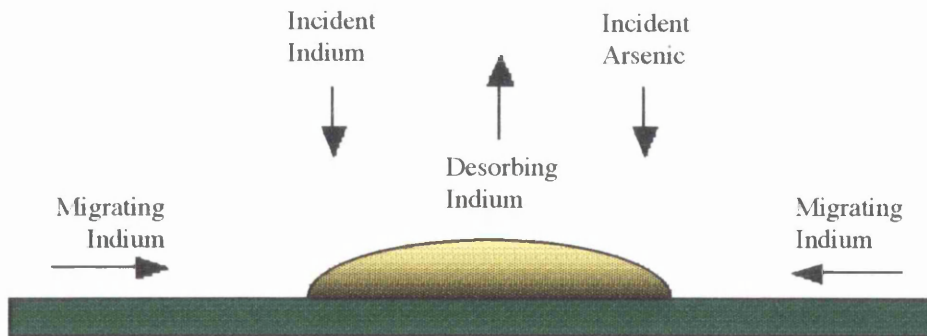
Figure 3.6. Matter flows into and out of an indium droplet.

If the number of indium droplets on the surface is relatively constant with substrate temperature, then the amount of indium which can be involved in any interaction with the droplets will also be constant and the growth rate will stabilise at a lower value for substrate temperatures above T_C. The step in growth rate is, therefore, a surface kinetic effect rather than one produced by

thermodynamic considerations. This does not, however, preclude the use of thermodynamic arguments to analyse the results obtained.

3.5 Thermodynamic Analysis

Despite the fact that MBE growth takes place under strongly non-equilibrium conditions, it has been shown that a thermodynamic approach can be used[18] to model growth processes. Modulated beam experiments[19,20,21] have demonstrated that the thermalisation time of incident atoms and molecules is much shorter than the time taken to deposit one monolayer and desorbing atoms can be assumed to have the temperature of the substrate regardless of the temperature of the incident species.

At normal growth temperatures, desorption of As_2 predominates over As_4[22,23,24]. The main desorption reaction for InAs is therefore[25] :-

$$InAs(s) \rightarrow In(g) + \tfrac{1}{2} As_2(g) \qquad (3.2)$$
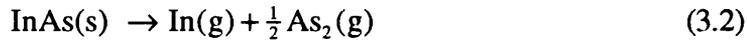
For which the equilibrium constant is:-

$$K_{InAs} = p_{As_2}^{\frac{1}{2}} p_{In} \qquad (3.3)$$

The value of this equilibrium constant can be calculated from the equation (ref.25 eq^n 9):-

$$\ln K_{InAs} = -47696 / T + 25.17 \qquad (3.4)$$

where P_{As_2} and P_{In} are the equilibrium partial pressures of indium and arsenic over the substrate surface. The congruent vaporisation relation for InAs is :-

$$F_{As_2} = \tfrac{1}{2} F_{In} \qquad or \qquad \frac{F_{As}}{F_{In}} = 1 \qquad (3.5)$$

where F_{As} and F_{In} are the atomic flows of arsenic and indium respectively. In vacuum, the atomic flow is related to the partial pressure of a species by the Hertz-Knudsen relation[26]:-

$$F_j = \frac{\sum_j (v_j^i p_j \alpha_j)}{\sqrt{2\pi M_j RT}} \qquad (3.6)$$

where v_j^i is the stoichiometric coefficient of the element i in any gaseous species j, M_j is the molar mass, p_i is the partial pressure and α_j is the evaporation coefficient. Substituting into equation 3.3 gives :-

$$\frac{p_{As_2}}{p_{In}} = \frac{1}{2}\sqrt{\left(\frac{M_{As_2}}{M_{In}}\right)} = 0.571 \qquad (3.7)$$

This can be substituted into equation 3.3 to give the arsenic partial pressure over the solid solution (ref.**25** eq^n 11):-

$$\ln p_{As_2}^{S} \, (atm) = -31798 \, / \, T + 16.40 \qquad (3.8)$$

Under indium rich conditions, the value of P_{As_2} can be obtained from the arsenic partial pressure along the In-InAs liquidus of InAs. Figure 3.7 shows the liquidus of InAs reproduced from Tmar et al [27].
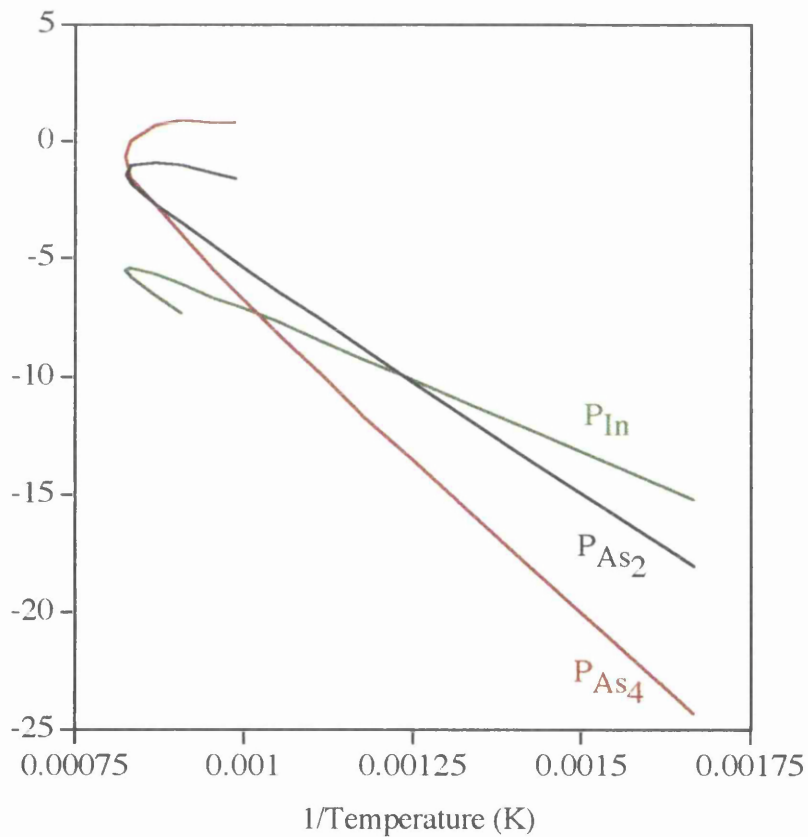
Figure 3.7. Partial Pressures of As$_2$,As$_4$ and In along the liquidus in the InAs system (from Tmar et al [27])

This gives :-

$$\ln p_{As_2}^{L} \,(atm) = -38166 \,/\, T + 26.57 \qquad\qquad (3.9)$$

Figure 3.8 shows the data of Figure 3.3 replotted as G_r^{max} versus $1/T_s$. Also plotted is the natural logarithm of the desorption rate of As_2, $Ln(D_r^{As_2})$, expressed in $\mu m/hr$ and calculated from the difference between G_r^{max} and $2.60\mu m/hr$.
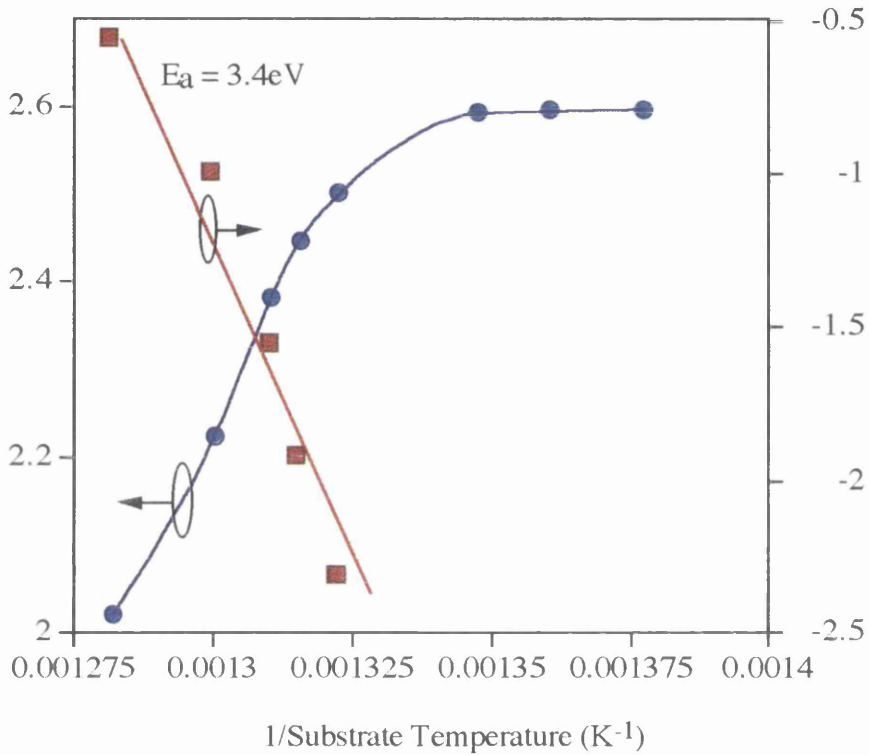
Figure 3.8. G_r^{max} and $Ln(D_r^{As_2})$ vs $1/T_s$ for the homoepitaxial growth of InAs.

The slope of the desorption curve has an activation energy of 3.4eV in the region where significant arsenic desorption is taking place. This value should be compared with the activation energy of 3.3eV for the partial pressure of As_2 along the InAs liquidus as described by Tmar *et al* [27] . An implication of this result is that the sticking coefficient of arsenic on InAs is determined by the desorption rate of As_2 from InAs which is independent of growth rate and depends only on the substrate temperature used. This confirms the results of Hancock *et al* [28] who found by studying the transition from a (2×4) to a (4×2) reconstruction that the governing factor controlling the substrate temperature for this change was not the flux ratio but rather the amount of excess arsenic supplied.

Shen *et al* [29] have shown that the limit of congruent vaporisation is given by the intersection of the $p_{As_2}^{L}$ and the $p_{As_2}^{S}$ lines (shown graphically in Figure 3.9). This represents the maximum stable temperature of InAs under vacuum and

in the absence of any arsenic overpressure. For substrate temperatures higher than this the arsenic flow is larger than that of indium and the excess indium builds up on the surface and forms droplets. The congruent temperature limit value derived from Figure 3.9 is 400°C which may be compared with the value of 380°C quoted by Wood[30].

If it is assumed that the ratio of incident and desorbing partial pressures is approximately equal to the ratio of incident and desorbing fluxes, then the excess arsenic necessary to suppress droplet formation during growth is equal to the difference between the arsenic partial pressures for congruent evaporation and the partial pressure along the liquidus :

$$p_{As_2}^{Excess} = p_{As_2}^{L} - p_{As_2}^{S} \qquad (3.10)$$
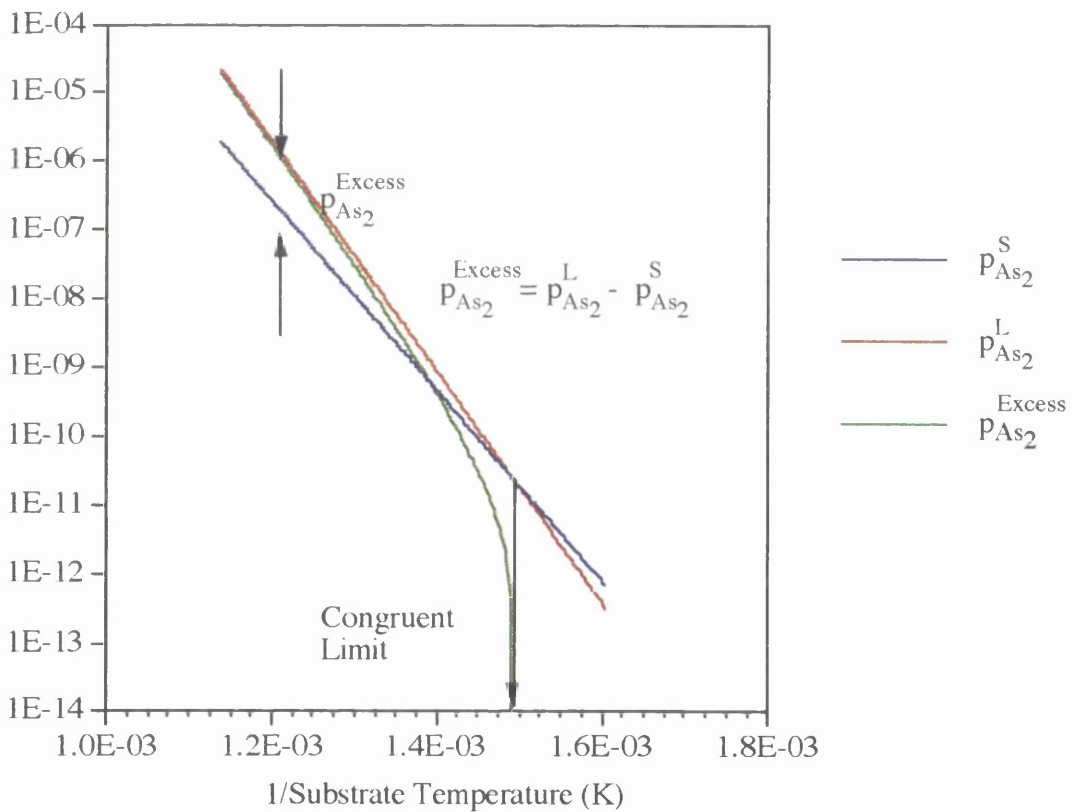
Figure 3.9. Partial arsenic pressures over the solid solution and diphasic liquid/solid phases of InAs. The arsenic pressure needed to stabilise the surface and prevent any droplet formation is given by the difference between the two pressures at temperatures above the congruent limit.

The total incident arsenic pressure necessary for the MBE growth of InAs in the regime where it is necessary to suppress the formation of indium droplets can be considered as consisting of two components :-

$$p_{As_2}^{Incident} = p_{As_2}^{0} + p_{As_2}^{Excess} \qquad (3.11)$$

where $p_{As_2}^{0}$ is a constant representing the minimum arsenic partial pressure necessary for growth at low temperature. Its value can be calculated from the flux necessary for a desired growth rate. $p_{As_2}^{Excess}$ is the extra arsenic required to stabilise the surface and is a function of substrate temperature. The value of $p_{As_2}^{Incident}$ calculated from equation 3.11 is shown in Figure 3.10 as a function of substrate temperature for low temperature growth rates corresponding to 1.0μm/hr and 0.625μm/hr. The experimental points measured using the growth rate transition point are shown superimposed on the theoretical lines. The agreement with theory is excellent.
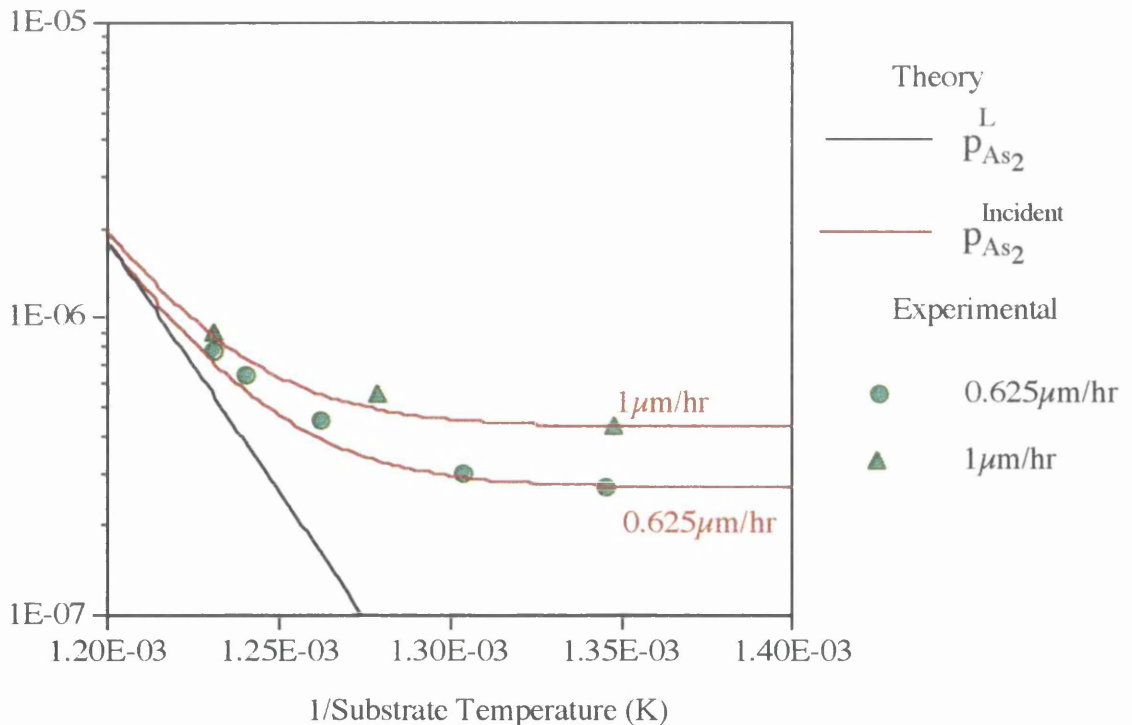
Figure 3.10. Theoretically calculated and experimentally measured minimum arsenic pressures as a function of the inverse of the substrate temperature. The solid lines represent the theoretical predictions of equation 3.11 for the transition between good morphology and indium accumulation on the InAs surface. The circles represent the experimentally measured values of T_C for growth at an initial low temperature rate of 0.625μm/hr and the triangles represent measured values of T_C for an initial growth rate of 1.0μm/hr.

The experimentally measured excess arsenic pressure as a function of the inverse of the substrate temperature is shown in Figure 3.11. It is apparent that the excess arsenic necessary to stabilise the surface and prevent droplet formation is independent of the growth rate, and is a function only of the substrate temperature during growth.
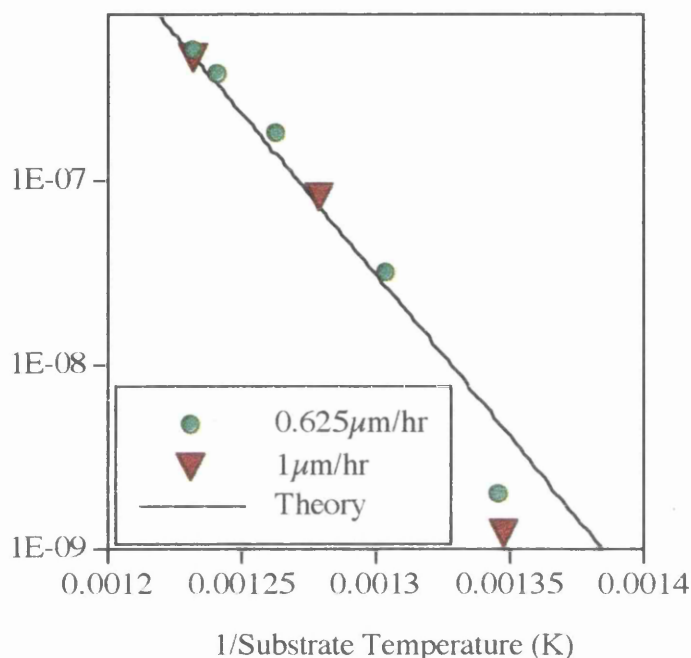
Figure 3.11. Theoretical and experimental values for the excess arsenic partial pressure necessary to stabilise the surface of InAs as a function of the inverse of the substrate temperature.

3.6. Conclusions

The onset of indium accretion on the surface of InAs produces a characteristic drop in the growth rate measured by RHEED oscillations. The drop in growth rate also coincides with a transition from an initial rise to an initial drop in the intensity of the RHEED oscillations at the commencement of growth. The formation of indium droplets on the surface can be suppressed by the use of an arsenic pressure in excess of that needed for growth. The amount of excess arsenic which it is necessary to supply is determined by the substrate temperature and is completely independent of the InAs growth rate used. Experimental measurements of the behaviour of InAs are in good agreement with predictions based on thermodynamic considerations. This implies that the formation of indium droplets is related to the partial pressure of As_2 over the InAs surface. The growth of InAs is normally performed at temperatures well above the limit of congruent evaporation where the equilibrium partial pressure of As_2 over the two phase

phase solid/liquid regime dominates over the partial pressure for congruent evaporation. This is supported by observations of G_r^{max} as a function of substrate temperature which confirm that the activation energy for arsenic desorption (3.4eV) is similar to that for evaporation from the two phase regime (3.3eV).

Metallic droplet formation has also been observed in the growth of InP[31] and the lattice matched ternary $In_{0.53}Ga_{0.47}As$ system[2]. Growth of both of these materials is performed at temperatures considerably higher than their congruent limit. By comparison, the relative insensitivity of GaAs to growth conditions can be explained by the congruent evaporation limit of 650°C being very close to the temperature at which gallium desorption starts to become significant. In this case gallium is evaporated before any droplets are able to accumulate.

3.7 References

1 'Gallium Desorption From (Al,Ga)As Grown By Molecular-Beam Epitaxy At High-Temperatures'
A.H. Kean, C.R. Stanley, M. Holland, J.L. Martin, J.N. Chapman
Journal Of Crystal Growth 1991 Vol.111 No.14 pp.189-193

2 'Incorporation Rates of Gallium and Aluminum on GaAs During Molecular-Beam Epitaxy at High Substrate Temperatures'
R. Fischer, J. Klem, T.J. Drummond, R.E. Thorne, W. Kopp, H. Morkoc, A.Y. Cho
Journal Of Applied Physics 1983 Vol.54 No.5 pp.2508-2510

3 'Molecular-Beam Epitaxy (MBE) of GaAs and (Al,Ga)As on Unoriented GaAs(100) Substrates'
B.Y. Ber, V.P. Evtikhiev, A.B. Komissarov, A.O. Kosogov, D.A. Zushinskii
Pisma V Zhurnal Tekhnicheskoi Fiziki 1992 Vol.18 No.11 p.72-76

4 'Gallium Desorption from GaAs and (Al,Ga)As During Molecular-Beam Epitaxy Growth at High-Temperatures'
E.M. Gibson, C.T. Foxon, J. Zhang, B.A. Joyce
Applied Physics Letters 1990 Vol.57 No.12 pp.1203-1205

5 'Thermodynamic Aspects of Molecular-Beam Epitaxy - High-Temperature Growth in the $GaAs/Al_xGa_{1-x}As$ System'
R. Heckingbottom
Journal Of Vacuum Science & Technology B-Microelectronics Processing and Phenomena 1985 Vol.3 No.2 pp.572-575

6 'Studies of Indium Incorporation into InAs and InGaAs'
M. McElhinney, C.R. Stanley
Presentation to the 7th European Workshop on Molecular Beam Epitaxy 1993 B3

7 'Reduced Indium Incorporation During the MBE Growth of In (Al, Ga) As'
M. McElhinney and C.R. Stanley
Electronics Letters 1993 Vol.29 No.14 pp1302-1304

8 'Growth And Doping Of Gallium-Arsenide Using Molecular-Beam Epitaxy
   (MBE) - Thermodynamic And Kinetic Aspects'
   R. Heckingbottom, G.J. Davies, K.A. Prior
   Surface Science 1983 Vol.132 No.13 pp.375-389

9 'Peak Electron Mobilities Between 2.75 and 3.32×10^5 cm^{2}V^{-1}s^{-1} in GaAs
   Grown by Molecular Beam Epitaxy with As$_2$'
   C.R. Stanley, M.C. Holland, A.H. Kean
   Applied Physics Letters 1990 Vol.57 No.19 pp1992-1994

10 'Interaction Kinetics of As$_2$ and Ga on (100) GaAs Surfaces'
   C.T. Foxon, B.A. Joyce
   Surface Science 1977 Vol.64 No.1 pp293-304

11 'RHEED Oscillations of Arsenic-Controlled Growth-Conditions to Optimize
   MBE Growth of III/V Heterostructures'
   R. Fernandez
   Journal Of Crystal Growth 1992 Vol.116 No.1-2 pp.98-104

12 'Determination of As$_2$ Sticking Coefficients Using Reflection High Energy
   Electron Diffraction Intensity Oscillations on GaAs (001)'
   R. Fernandez, R. Chow
   Materials Research Society Symposium Proceedings: III-V Heterostructures
   for Electronic / Photonic Devices 1989 Vol.145 pp.13-19

13 'Bonding Direction and Surface-Structure Orientation on GaAs (001)'
   A.Y. Cho
   Journal of Applied Physics 1976 Vol.47 No.7 pp2841-2843

14 'Reproducible Growth Conditions by Group III and Group V Controlled
   Incorporation Rate Measurements'
   R. Fernandez
   Journal of Vacuum Science & Technology 1988 Vol.B6 No.2 pp745-748

15 'Relation Between Growth Conditions and Reconstruction on InAs During
   Molecular Beam Epitaxy Using an As$_2$ Source'
   B.R. Hancock and H. Kroemer
   Journal of Applied Physics 1984 Vol.55 No.12 pp4239-4243

16 W.J. Schaffer

Presentation to the 3rd Annual Molecular Beam Epitaxy Workshop

University of California, Santa Barbara 1981

17 'Reflection High-Energy Electron-Diffraction Oscillations From Vicinal
Surfaces'

J.H. Neave, P.J. Dobson, B.A. Joyce, J. Zhang

Applied Physics Letters 1985 Vol.47 No.2 pp.100-102B

18 'Growth And Doping Of Gallium-Arsenide Using Molecular-Beam Epitaxy
(MBE) - Thermodynamic And Kinetic Aspects'

R. Heckingbottom, G.J. Davies, K.A. Prior

Surface Science 1983 Vol.132 No.1-3 Pp.375-389

19 .'Interaction Kinetics of As$_4$ and Ga on (100) GaAs Surfaces Using a
Modulated Beam Technique'

C.T. Foxon, B.A. Joyce

Surface Science 1975 Vol.50 No.2 pp434-450

20 'Interaction Kinetics of As$_2$ and Ga on (100) GaAs Surfaces'

C.T. Foxon, B.A. Joyce

Surface Science 1977 Vol.64 No.1 pp293-304

21 'Growth-Kinetics Of InSb Thin-Films on Si(100) Surfaces by In and Sb$_4$'
Molecular-Beams'

M. Yata

Thin Solid Films 1986 Vol.137 No.1 pp.79-87

22 'The Evaporation of GaAs Under Equilibrium and Non-Equilibrium
Conditions Using a Modulated Beam Technique'

C.T. Foxon, J.A. Harvey, B.A. Joyce

Journal of Physics and Chemistry of Solids 1975 Vol.34 No.10 pp1693-1701

23 'The Identification of Species Evolved in the Evaporation of III-V Compounds'
C.T. Foxon, B.A. Joyce, R.F.C. Farrow, R.M. Griffiths
Journal of Physics 1974 Vol.17 No.17 pp2422-2434

24 'Molecular-Beam Epitaxy of Heterostructures Made of III-V-Compounds'
P.S. Kopev, N.N. Ledentsov
Soviet Physics Semiconductors-USSR 1988 Vol.22 No.10 pp.1093-1101

25 'Thermodynamic of the Molecular Beam Epitaxy of III-V Compounds'
J. Shen and C. Chatillon
Journal of Crystal Growth 1990 Vol.99 No.106 pp553-565

26 'Evaporation from Solids'
Edited by N.B. Hannay
(Plenum, New York, 1967)

27 'Critical Analysis and Optimization of the Thermodynamic Properties and Phase Diagrams of the III-V Compounds'
M. Tmar, A. Gabriel, C. Chatillon and I. Ansara
Journal of Crystal Growth 1984 No.69 pp421-441

28 'Relation Between Growth Conditions and Reconstruction on InAs During Molecular Beam Epitaxy Using an As_2 Source'
B.R. Hancock and H. Kroemer
Journal of Applied Physics. 1984 Vol.55 No.12 pp4239-4243

29 'Thermodynamic Calculations of Congruent Vaporization in III-V Systems; Applications to the InAs, GaAs and GaInAs Systems'
J. Shen and C. Chatillon
Journal of Crystal Growth 1990 Vol.99 No.106 pp543-552

30 'Alloy Growth by Molecular Beam Epitaxy'
C.E.C Wood
GaInAsP Alloy Semiconductors ed. by T.P.Pearsall
(Wiley, New York, 1982) p82

31 C.R. Stanley, V.M. Airaksinen, R.H. Hutchins and M. McElhinney
   Presentation to the 6th European Workshop on Molecular Beam Epitaxy
   Tampere, Finland 1991

Chapter 4

Analysis of the Lattice Matched Growth of $In_{0.53}Ga_{0.47}As$ and $In_{0.52}Al_{0.48}As$ by MBE

4.1 Introduction

The combination of $In_{0.53}Ga_{0.47}As$ and $In_{0.52}Al_{0.48}As$ lattice matched to InP allows various high performance microwave[1,2,3,4] and optoelectronic[5,6,7,8] devices to be realised. The growth of such devices by MBE requires that the group III atoms in the molecular beam are uniformly distributed and precisely controlled to give the desired composition and growth rate. Several methods of achieving composition uniformity in MBE grown $In_{0.53}Ga_{0.47}As$ and $In_{0.52}Al_{0.48}As$ layers have been tried, including the use of premixed In-Ga charges[9], coaxial In-Ga effusion cells[10], and substrate rotation[11]. The rotating substrate holder proved to be the most successful approach, making it possible to grow III-V ternary compounds with extremely uniform epilayer thickness and composition[12]. This technique is now standard in most laboratories.

Precise control of alloy composition and growth rate has, however, been found to be more problematical since the $In_{0.53}Ga_{0.47}As/In_{0.52}Al_{0.48}As$ system presents many problems not found in the GaAs/AlGaAs case. The most accurate method of calibrating group III flux densities for the growth of GaAs/AlGaAs involves the use of reflected high energy electron diffraction (RHEED) intensity oscillations[13] to calculate the growth rate of the group III arsenide e.g. 30% AlGaAs at 1μm/hr can be obtained by setting growth rates of 0.7μm/hr and 0.3μm/hr for GaAs and AlAs respectively on a GaAs substrate. The large mismatch between the binary components of the $In_{0.53}Ga_{0.47}As/In_{0.52}Al_{0.48}As$ system makes it impossible to perform such direct growth rate measurements on an InP substrate. The standard method of flux calibration[14,15] is, therefore, to measure the pressure of the molecular beam from the group III source using a beam equivalent pressure (BEP) gauge in the growth position. Adjusting the ratio between the BEP readings for the group III sources enables the correct alloy composition to be set (the total reading is then used as a guide to the growth rate

of the ternary alloy). This method is relatively inaccurate and normally requires the growth of several calibration layers to improve the accuracy of the calibration which prohibits calibration on a day to day basis. This chapter describes attempts to perform calibration by RHEED intensity oscillations on separate InAs and GaAs binary substrates. This method should be capable of giving accurate and unequivocal values for the flux densities of the relative group III components of the alloys and allow precise control of both the alloy composition and growth rate.

The growth conditions of any ternary alloy are to a large extent determined by the thermal stability of the less stable of the two pseudo-binary compounds of which the alloy is composed. In the case of $In_{0.53}Ga_{0.47}As$ and $In_{0.52}Al_{0.48}As$ the behaviour is dominated by the InAs component. Typical growth temperatures used during $In_{0.53}Ga_{0.47}As$ and $In_{0.52}Al_{0.48}As$ growth are therefore much lower than those used in the growth of the GaAs/AlGaAs system, and even at these reduced temperatures, a large arsenic overpressure is needed to prevent a degradation of the surface morphology[16]. This has been assumed to be due to indium and gallium segregation which is controlled by the surface arsenic coverage[17]. In the previous chapter the stability of InAs was explored and a theoretical model for the observed behaviour was presented. In this chapter the ternary alloys are investigated and it is shown that a model for their behaviour can be extrapolated from the InAs case.

4.2 Experimental

All samples were grown using arsenic dimers (As_2). Substrates were etched in $5H_2SO_4 + H_2O_2 + H_2O$ and rinsed in deionised water prior to being indium bonded to 2" silicon wafers and loaded into standard spring mounting wafer holders. Si wafers were used in preference to the solid molybdenum blocks since better temperature controllability and uniformity were obtained. The heater stage temperature measured by a thermocouple gave a temperature reading very close to the sample temperature measured by an optical pyrometer, eliminating the possibility of large temperature differences across the sample caused by variations in the thermal contact between the substrate and the block. Sample temperatures were measured using an Ircon series V low temperature infra-red optical pyrometer.

4.3 Group III Flux Calibration

The unit cell of the zincblende lattice structure is shown in Figure 4.1. Each monolayer of this structure contains, on average, 2 group III atoms and 2 group V atoms in an area equal to a^2 where a is the lattice constant material.
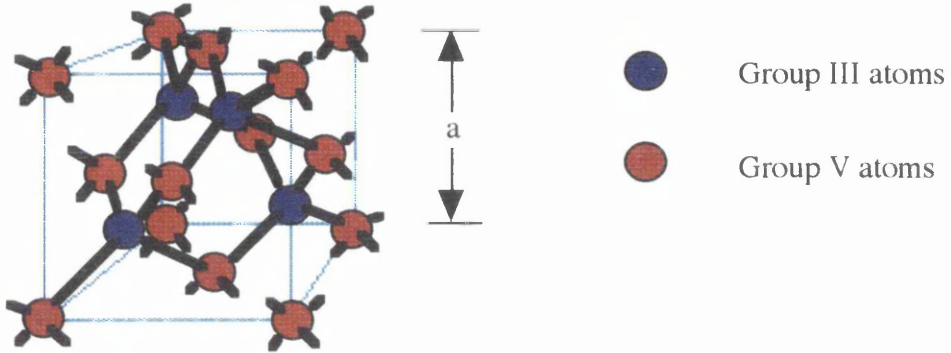
Figure 4.1 Unit cell of Zincblende structure.

For lattice matched growth on a given binary III-V substrate, the RHEED oscillation frequency (i.e. the growth rate expressed in monolayers per seconds) R, is related to the incident group III flux density D by the equation :-

$$D = \frac{2R}{a^2} \qquad (4.1)$$

where a is the material lattice constant.

The total group III flux density required to grow $In_{0.53}Ga_{0.47}As$ on InP at $1\mu m/hr$ is therefore given by :-

$$D = \frac{4}{\left(0.36 \times a_{InP}^3\right)} \qquad (4.2)$$

The indium flux density required for lattice matched growth is therefore :-

$$D_{In} = 0.533 \times \frac{4}{\left(0.36 \times a_{InP}^3\right)} \qquad (4.3)$$

and similarly the gallium flux density is given by :-

$$D_{Ga} = 0.467 \times \frac{4}{\left(0.36 \times a_{InP}^3\right)} \qquad (4.4)$$

These flux densities can be converted, by using equation (4.1), into growth rates for the growth of InAs on InAs and GaAs on GaAs. The calibration points for the growth of $In_{0.52}Al_{0.48}As$ can be calculated in a similar fashion. However in order that the growth of the $In_{0.52}Al_{0.48}As$ material should be compatible with $In_{0.53}Ga_{0.47}As$ growth, the indium flux density is held constant, and the aluminium flux density is calculated so that the correct indium fraction ($x = 0.521$) is obtained. This gives an alloy growth rate of $1.023\mu m/hr$ which is slightly larger than that for $In_{0.53}Ga_{0.47}As$.

This approach has the potential to give the same systematic control to the composition of InGaAs/AlInAs as is normally obtained with the GaAs/AlGaAs system. There are, however, a number of factors which complicate the relationship between the incident indium flux and the measured growth rate and which must be taken into account during the calibration of the indium flux.

The accuracy of this technique depends on the precise knowledge of the lattice constants of GaAs and InAs and the variation of these lattice constants with temperature. Published values for the thermal expansion coefficients of GaAs and InAs give a required growth rate for InAs on InAs of $0.592\mu m/hr$ at a substrate temperature of around $460°C$, and $0.422\mu m/hr$ for the growth rate of GaAs on GaAs at a calibration temperature of $\approx580°C$. In practice, these values produce layers which are slightly gallium rich when the composition is measured by double crystal X-ray diffractometry (DCXD). Equally important, the growth rate of the ternary alloy measured by RHEED is found to be less than $1\mu m/hr$.

To determine the correct In calibration point, several layers were grown with increasing InAs growth rates during calibration. In addition, sample #B253 containing 6 layers with In cell temperatures corresponding to InAs growth rates in the $0.60 - 0.65\mu m/hr$ range was grown. The structure is shown schematically in Figure 4.2. The substrate temperature during the growth of this sample was $520°C$. The substrate temperature during the growth of the individual layers was between $520°C$ and $530°C$. The Ga cell was held at a constant temperature corresponding to a growth rate of $0.422\mu m/hr$ for GaAs on GaAs for all of the samples.
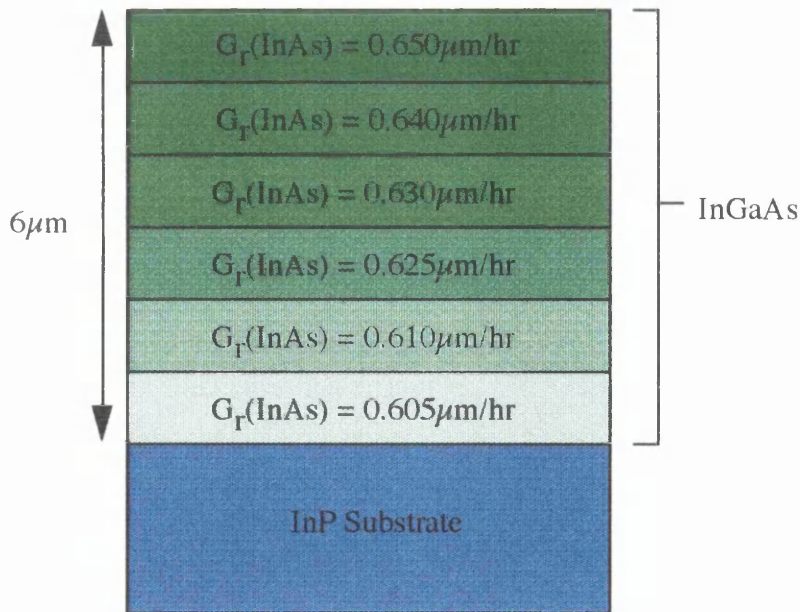
Figure 4.2. Schematic diagram of #B253. The sample contains six layers with InAs on InAs calibration growth rates in the range 0.60 - 0.65μm/hr. The thickness of each layer was 0.5μm.

The DCXD rocking curve for sample #B253 is shown in Figure 4.3. Only 5 peaks are visible around the main substrate peak, indicating that one of the layers is exactly lattice matched. The calculated compositions from both the individual layers and the composite structure are plotted as a function of InAs on InAs growth rate in Figure 4.4. Data for both individual 1μm thick InGaAs layers and the composite layer #B253 appear to be in good agreement.

The growth rate for lattice matching suggested by the data in Figure 4.4 is 0.625μm/hr. In$_{0.52}$Al$_{0.48}$As layers which were grown with an InAs calibration of 0.625μm/hr were also found to be lattice matched and the measured growth rate was 1.023μm/hr as predicted. The InAs calibration point is considerably higher than the predicted value of 0.592μm/hr. The difference is too large to be accounted for by an error in the thermal expansion coefficient, since it would represent an expansion 10 times larger than the published values. The explanation must therefore lie with a decrease in In incorporation during growth. The increase in the calibration growth rate corresponds to an In desorption rate of $\approx$0.015μm/hr from the In$_{0.53}$Ga$_{0.47}$As layer.
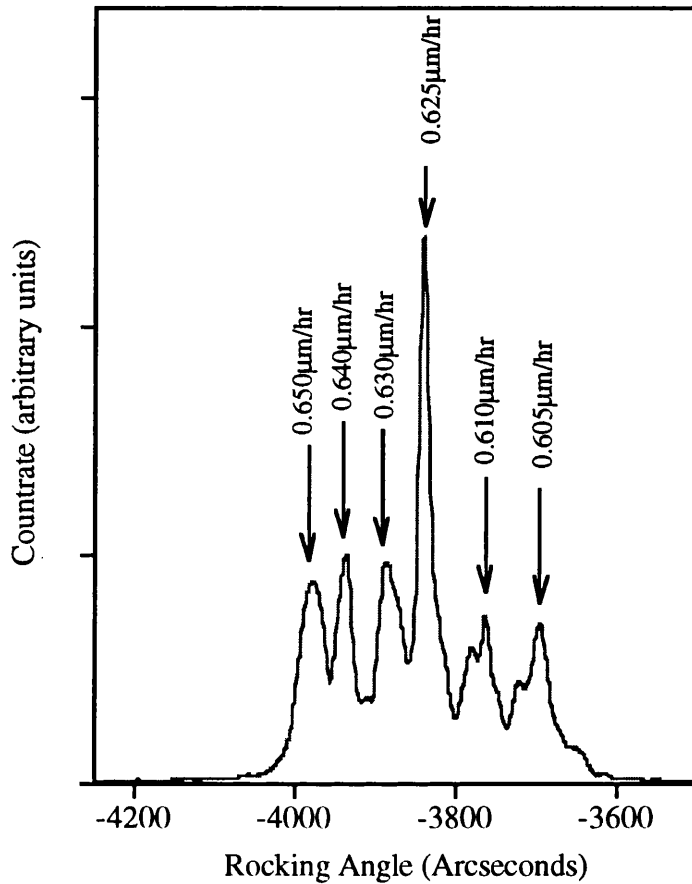
Figure 4.3 DCXD rocking curve for InGaAs composite layer grown with 6 different indium cell temperatures corresponding to growth rates for InAs on InAs of between 0.59 and 0.64μm/hr. The Ga cell was held at a constant temperature corresponding to a growth rate of 0.422μm/hr for GaAs on GaAs. Only 5 peaks are visible, indicating that one of the layers is exactly lattice matched. The calculated composition is plotted as a function of InAs on InAs growth rate in Figure 4.4
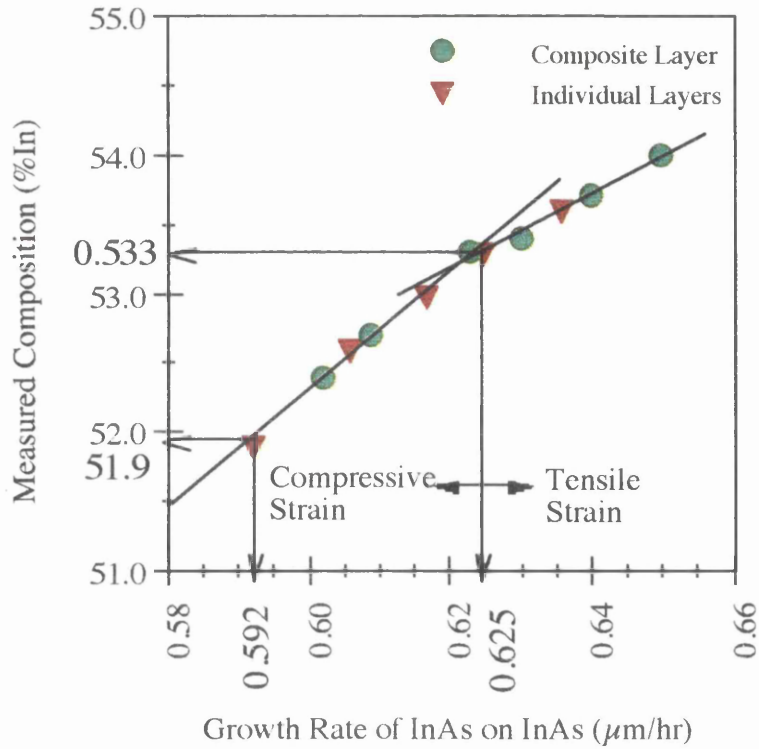
Figure 4.4. Composition measured by DCXD vs calibration growth rate of InAs on InAs. The Ga flux was held constant at a value corresponding to a growth rate of 0.422μm/hr GaAs on GaAs. Change in slope of graph represents influence of strain on In desorption rate. It should be noted that the relationships are not linear and the lines are included only as a guide to the eye.

There is a change in the slope of the data plotted in Figure 4.4 between the regions on either side of the lattice matched condition. This is probably due to the influence of strain on the In desorption rate. The effect of strain is to reduce the activation energy required for the desorption process, producing an increase in the desorption rate, which further reduces the indium composition and hence the amount of strain in the layer. If the incident indium flux density is smaller than that necessary for lattice matched growth ($G_{r_{InAs}} < 0.625\mu$m/hr), the compositional change produced by a variation in indium flux density will be larger than expected since the change in the rate of indium incorporation is enhanced by strain. In contrast, for the case where the incident In flux density is larger than that necessary for lattice matched conditions ($G_{r_{InAs}} > 0.625\mu$m/hr), the feedback mechanism between In desorption and strain tends to reduce any change in composition produced by an increase in the incident In flux density, since the strain induced desorption rate is now proportional to the indium content of the layer.

65
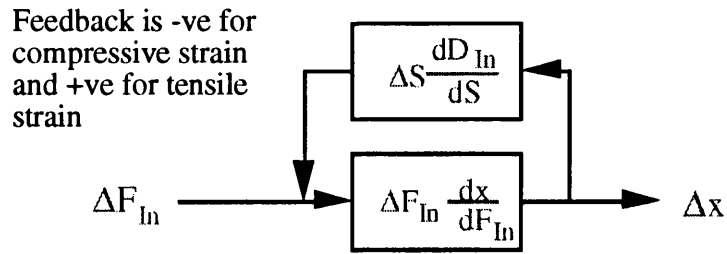
F_{In} = Incident indium flux density

S = Strain energy

D_{In} = Desorbing indium flux density

Figure 4.5. 'Feedback mechanism' for the influence of strain on the relationship between incident indium flux and bulk composition.

A switch in the sign of ΔS at the lattice matched condition produces a change in the sign of the feedback, giving the change in slope observed in Figure 4.4. It should be noted that the relationship between composition and incident indium flux is not linear and the lines shown in Figure 4.4 are intended only as a guide to the eye.

If the desorbing indium flux density produced by the strain feedback effect can be increased until it is similar to the change in incident flux density then the system can, in theory, be made to 'self-lock' to the lattice constant of the InP substrate. This is considered in more detail in section 4.6.

4.4 Growth Conditions

It has been shown in chapter 3 that the growth of InAs at substrate temperatures above the maximum temperature for congruent evaporation (T_{ce}) produces preferential arsenic vaporisation which leads to the appearance of metallic droplets on the InAs surface. These can be suppressed by increasing the arsenic overpressure. During growth, the onset of droplet formation coincides with a drop in the growth rate measured by RHEED intensity oscillations and the disappearance of an initial increase in the intensity of the RHEED specular spot. The RHEED diffraction pattern, however, remains an arsenic stable (2×4) during growth in the regime where droplets are forming.

The step-like drop in growth rate has also been observed for the growth of the indium containing ternary alloys. Figure 4.6 shows the variation of growth rate

for InAs on InAs, and $In_{0.53}Ga_{0.47}As$ and $In_{0.52}Al_{0.48}As$ grown on an InP substrate with an identical As_2 partial pressure of 2.7×10^{-7} Torr.
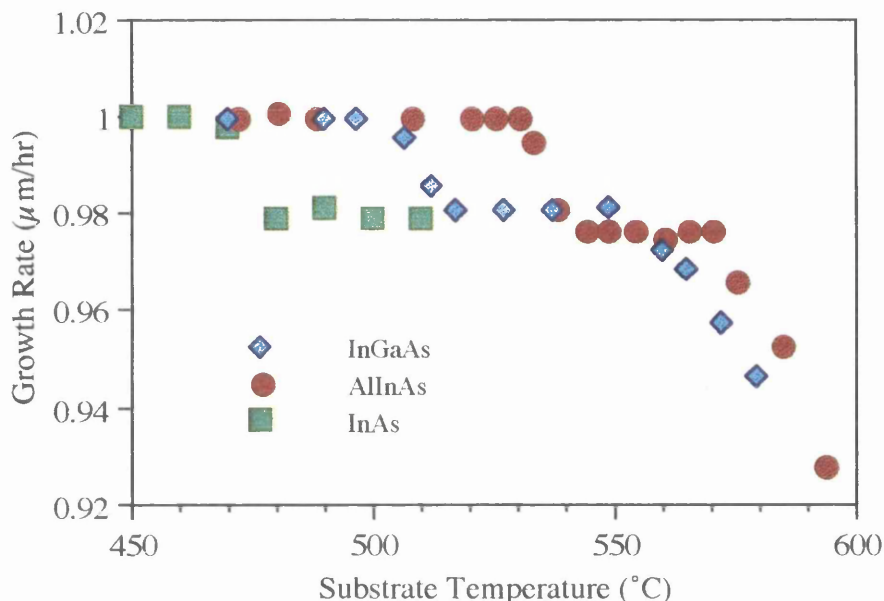
Figure 4.6. Growth rates determined by RHEED oscillations for InAs, $In_{0.53}Ga_{0.47}As$ and $In_{0.52}Al_{0.48}As$ as a function of substrate temperature for a constant arsenic dimer flux.

The general behaviour of the ternary alloys is similar to that of InAs, but the transition temperature (T_c) between the two plateau regions is higher for $In_{0.53}Ga_{0.47}As$ and higher still for $In_{0.52}Al_{0.48}As$. This is similar to the relationship between the congruent evaporation temperatures, T_{ce}, for the materials with T_{ce} InAs $< T_{ce}$ $In_{0.53}Ga_{0.47}As < T_{ce}$ $In_{0.52}Al_{0.48}As$. The size of the step is approximately the same for each material. At $\approx 555^{\circ}C$ the growth rate of $In_{0.53}Ga_{0.47}As$ becomes a strong function of substrate temperature as the indium desorption starts to vary rapidly for a small change in substrate temperature. This occurs at the slightly higher temperature of $\approx 570^{\circ}C$ for $In_{0.52}Al_{0.48}As$. In both cases the onset of measurable desorption occurs at substrate temperatures well removed from T_c. The curves are repeatable for both increasing and decreasing substrate temperatures. The initial rise in the intensity of RHEED specular spot observed for InAs, also correlates with T_c for the lattice matched ternary alloys.

Figure 4.7 shows Normaski phase contrast images of two InGaAs layers, one grown on the upper ($T < T_c$) plateau and the other grown on the lower ($T > T_c$) plateau.

67
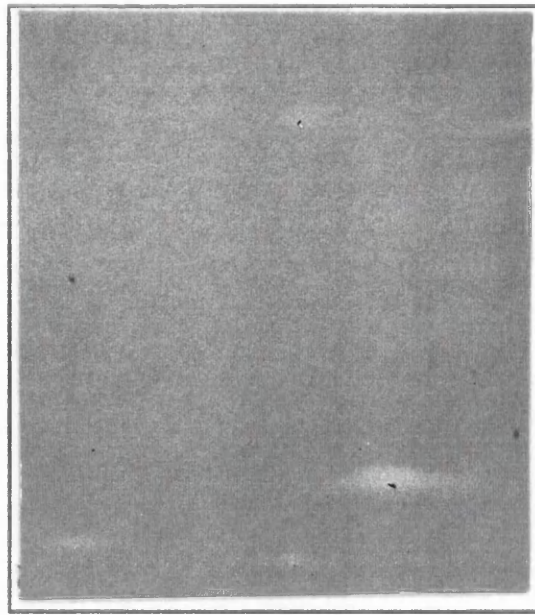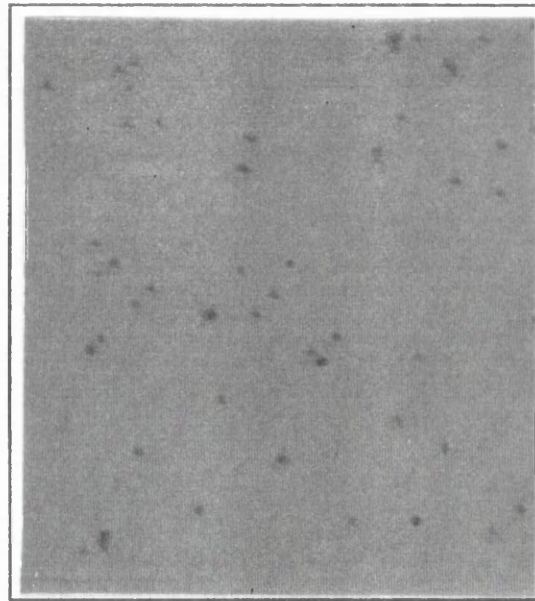
Figure 4.7. Normaski phase contrast image for InGaAs layers grown on (a) the upper (T<T$_C$) plateau of Figure 4.6 and (b) the lower (T>T$_C$) plateau of Figure 4.6. The InGaAs layer grown on the upper, higher growth rate region has a mirror finish, while the layer grown above T$_C$ contains many surface defects.
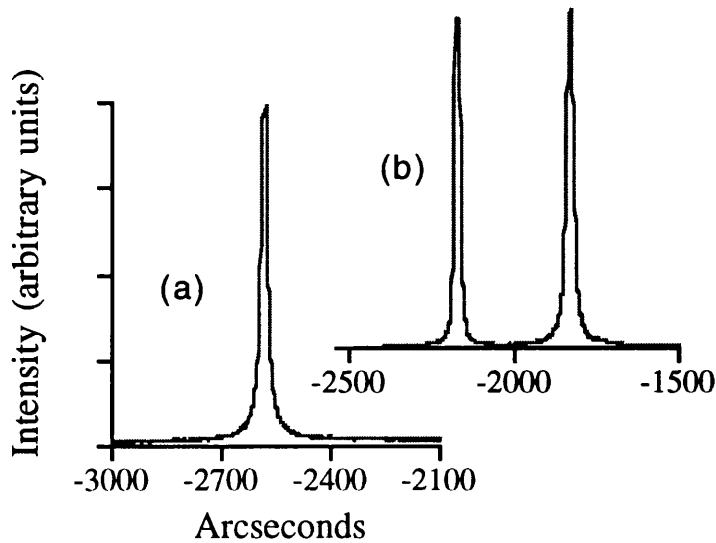
Figure 4.8. DCXD rocking curves for (a) InGaAs sample grown on upper (<T_C) plateau of growth rate curve (b) InGaAs sample grown on lower (>T_C) plateau of growth rate curve.

The InGaAs layer grown in the upper, higher growth rate region has excellent morphology with only the usual oval defects. This contrasts sharply with the layer grown at a substrate temperature just above T_C where a reduction in growth rate has occurred. The surface of this sample contains many globular defects. Energy Dispersive Analysis by X-ray (EDAX) shows these defects to be indium rich. The DCXD rocking curves of the two layers are shown in Figure 4.8. The lower temperature sample contains only one peak indicating that the layer is lattice matched. The rocking curve for the higher temperature sample contains separate layer and substrate peaks indicating a slight mismatch between the lattice constants of the $In_xGa_{1-x}As$ and the InP substrate. The spacing of the peaks corresponds to a layer composition of x=0.512 which agrees very well with the growth rate reduction of 0.019μm/hr measured immediately before growth of this layer (refer to figure 4.6). This leads to the conclusion that the measured drop corresponds to the onset of the formation of metallic droplets which are composed almost exclusively of liquid indium. The creation of these droplets appears to stabilise the surface and prevent further increases in the rate of indium loss, keeping the proportion of indium which incorporates into the lattice relatively constant until higher temperatures where desorption becomes measurable. The RHEED reconstruction observed at T_s > T_c remains a (2×4) pattern of the type normally seen during the growth of As-stable (100)-GaAs, until the onset of measurable desorption when the pattern switches to a metal-stable (4×2) reconstruction.

4.5 Thermodynamic Analysis

4.5.1 Congruent Evaporation

The thermodynamic treatment of InAs growth in chapter 3 has shown that the relationship between the atomic flow rates for the congruent vaporisation of InAs is given by :-

$$\frac{F_{In}}{F_{As}} = 1 \qquad (4.5)$$

The atomic flow is related to the partial pressure of a species by the Hertz-Knudsen relation[18] :-

$$F_j = \frac{\sum_j (v_j^i p_j \alpha_j)}{\sqrt{2\pi M_j RT}} \qquad (4.6)$$

where v_j^i is the stoichiometric coefficient of the element i in any gaseous species j, M_j is the molar mass, p_j is the partial pressure and α_j is the evaporation coefficient. Therefore applying equation 4.5 for the InAs binary compound gives :-

$$\frac{p_{As_2}}{p_{In}} = \frac{1}{2}\sqrt{\left(\frac{M_{As_2}}{M_{In}}\right)} = 0.571 \qquad (4.7)$$

For congruent evaporation from a III_A-III_B-As alloy, which conserves the composition of the alloy, the ratios between the atomic flows for the congruent vaporisation are given by[19]:

$$\frac{F_{III_A} + F_{III_B}}{F_{As}} = 1 \qquad (4.8)$$

$$\frac{F_{III_A}}{F_{III_B}} = x \qquad (4.9)$$

where x is the alloy composition. In the case of the $In_{0.52}Al_{0.48}As$ and $In_{0.53}Ga_{0.47}As$ systems, the difference in volatilities of the group III components

70

means that equation 4.9 is never satisfied over any temperature range. The composition of the alloy is never conserved and the initial ternary composition will always move towards GaAs or AlAs by preferential desorption of indium, however degradation of the surface is avoided if equation 4.8 is satisfied. The conditions for the congruent vaporisation of $In_{0.52}Al_{0.48}As$ and $In_{0.53}Ga_{0.47}As$ therefore reduce to equation 4.7 and the ratio of the desorbing indium and arsenic partial pressures is identical to the ratio in the binary InAs case.

4.5.2 $In_{0.53}Ga_{0.47}As$

If strain effects are ignored, then the indium partial pressure over the InGaAs and AlInAs solid solutions can be estimated by treating the ternary alloy as a mixture of two binaries[20] e.g. in the case of InGaAs :-

$$In_xGa_{(1-x)}As = xInAs + (1-x)GaAs \qquad (4.10)$$
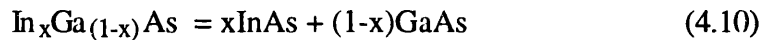
At substrate temperatures below 600°C the assumption can be made that all the Ga condenses as GaAs and it is only necessary to consider the behaviour of the InAs component of the pseudobinary material. The equilibrium equation is therefore given by :-

$$p_{As_2}^{\frac{1}{2}} p_{In} = \alpha_{InAs} K_{InAs} \qquad (4.11)$$

where α_{InAs} is the activity of InAs in the ternary solid solution. In general, the activity of a solute in a given solution is a constant whose value depends on the nature of the solute and the solvent. For an ideal solution there is no interaction between solute atoms and the activity is given by the fraction of the solution comprised by the solute i.e. :-

$$\alpha = x \qquad (4.12)$$

Experimental mass spectrometric measurements[21] performed on the InGaAs solid solution show that the value of α_{InAs} does not behave ideally, but is instead a function of both composition and temperature. For the case of x = 0.5 the activity is given by :-

$$\log(\alpha_{InAs}) = \frac{-383.1}{T} - 0.053 \qquad (4.13)$$

71

The activity coefficient calculated from equation 4.13 is shown as a function of temperature in Figure 4.9.
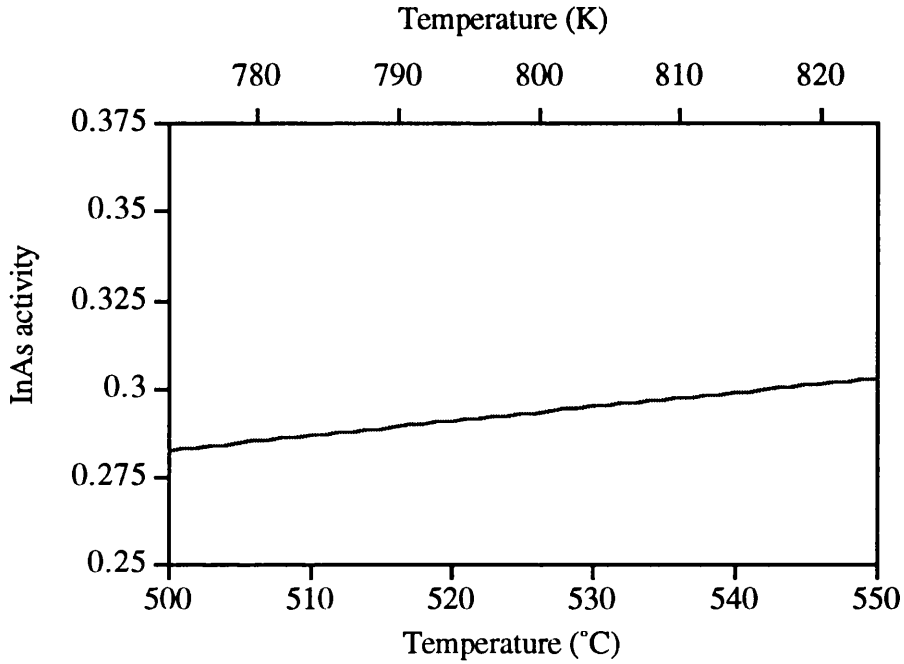
Temperature (K)

Figure 4.9. InAs activity in the $In_{0.5}Ga_{0.5}As$ solid solution as a function of temperature (from reference 21).

The value of the activity of InAs in the $In_{0.53}Ga_{0.47}As$ solid solution changes very little across the range of interest ($500\text{-}550°C$) so the assumption can be made that α_{InAs} is constant at a value 0.29. The relationship between the equilibrium partial pressures of In and As_2 over the $In_{0.53}Ga_{0.47}As$ solid solution is therefore given by :-

$$p_{As_2}^{\frac{1}{2}} p_{In} = 0.29 K_{InAs} \qquad (4.14)$$

The condition for congruent evaporation given in equation 4.7 can be combined with equation 4.14 to give the partial pressures of arsenic and indium for congruent evaporation from an $In_{0.53}Ga_{0.47}As$ surface :-

$$\ln p_{As_2}^S \ (atm) = -31798 / T + 16.40 + 2 / 3\ln 0.29$$
$$= -31798 / T + 15.57 \qquad (4.15)$$

$$\ln p_{In}^S \ (atm) = -31798 / T + 16.13 \qquad (4.16)$$

The activity of InAs in the InGaAs diphasic mixture has been measured[22,23] and found to resemble the ideal relationship given by equation 4.12. By substituting into equation 4.11, the In and As_2 partial pressures can be obtained from the InAs behaviour shown in Figure 3.7, giving :-

$$\ln p_{In}^{L} \text{ (atm)} = -28336 / T + 11.67 \qquad (4.17)$$

and

$$\ln p_{As_2}^{L} \text{ (atm)} = -38166 / T + 26.15 \qquad (4.18)$$

The values of p_{In}^{S} and p_{In}^{L} can be converted to In desorption rates expressed in μm/hr. The growth rate of $In_{0.53}Ga_{0.47}As$ as a function of substrate temperature calculated from these desorption rates is shown in Figure 4.10, together with experimental data for comparison.
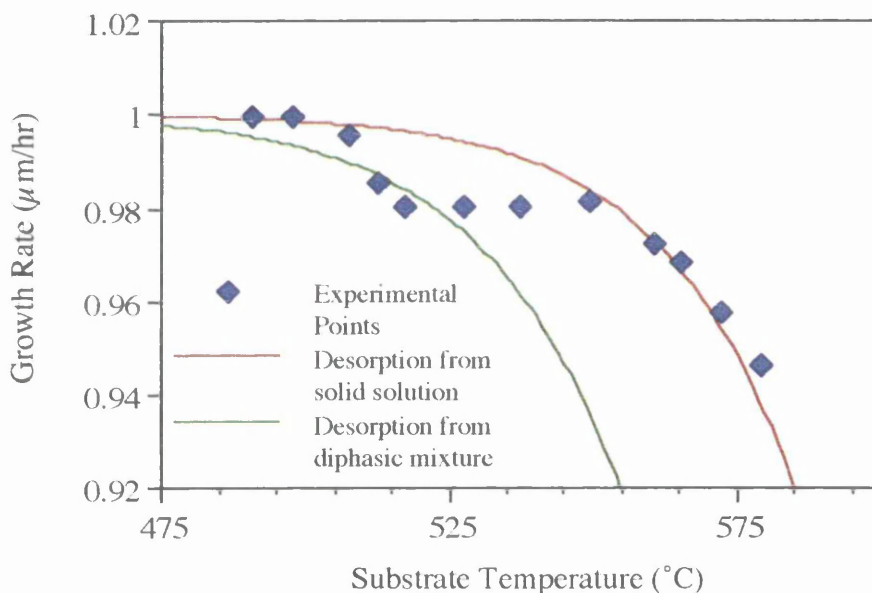
Figure 4.10. Theoretical curves for growth rate as a function of substrate temperature calculated from desorption rates from the $In_{0.53}Ga_{0.47}As$ solid solution and diphasic mixture. Experimental data from Figure 8 is included for comparison.

The agreement between the curve representing desorption from the solid solution and the experimental data is excellent, indicating that, in the region monitored by the RHEED intensity oscillations, the indium loss from the bulk can be calculated from the indium partial pressure over the solid solution. The presence of measurable indium desorption does not, however, mean that the indium droplets on the surface have begun to desorb, since only the droplet free areas of the surface are probed by the RHEED beam. To prevent droplet formation

entirely, it is necessary for the indium partial pressure along the liquidus to be greater than the incident indium partial pressure[24] i.e. :-

$$p_{In}^{L} > p_{In}^{Incident}$$ (4.19)

Figure 4.11 shows the incident and desorbing indium partial pressures as a function of the inverse of the substrate temperature according to equation 4.17. The partial pressure from a droplet does not become greater than the beam equivalent pressure of the incident indium flux until a temperature of approximately 575°C is reached. Droplet formation occurs therefore in the range given by $T_C < T_S < 575°C$. The surface morphology of samples grown at 565°C (in the regime of measurable desorption from the solid solution) and 600°C is shown in Figure 4.12. The sample grown at 565°C shows the presence of indium droplets while the sample grown at 600°C has a mirror-like surface. It should be noted, however, that the higher temperature sample was not lattice matched, due to the large In desorption rate from the solid solution at this temperature.
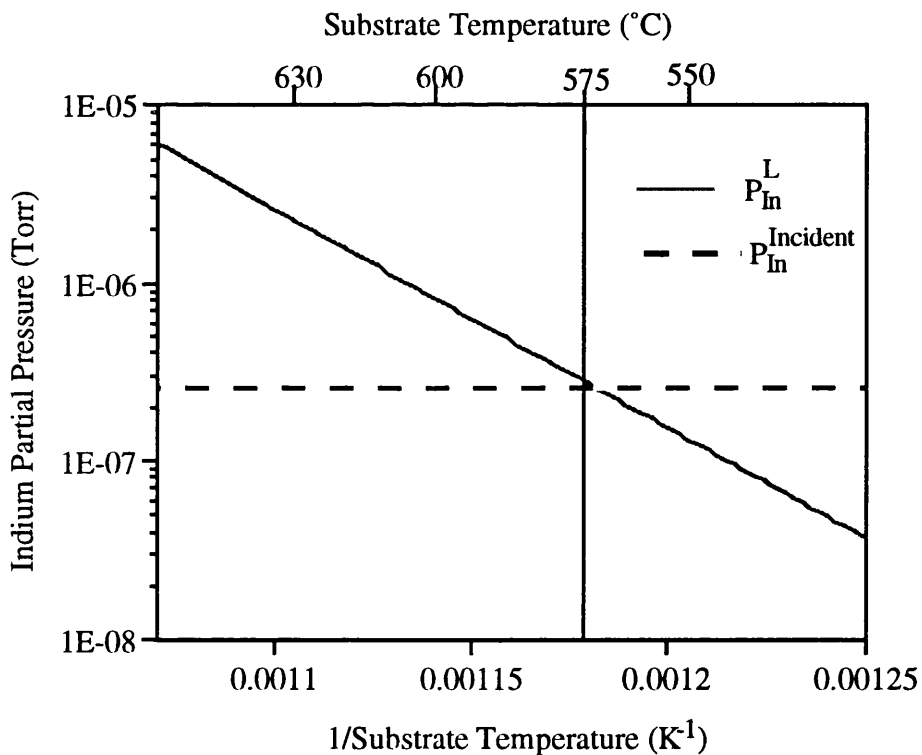
Figure 4.11. Indium partial pressure above the In-InGaAs liquidus as a function of $1/T_S$. The intercept with the incident partial pressure represents the maximum temperature at which indium droplets are stable on the InGaAs surface.

74

50μm

(a)
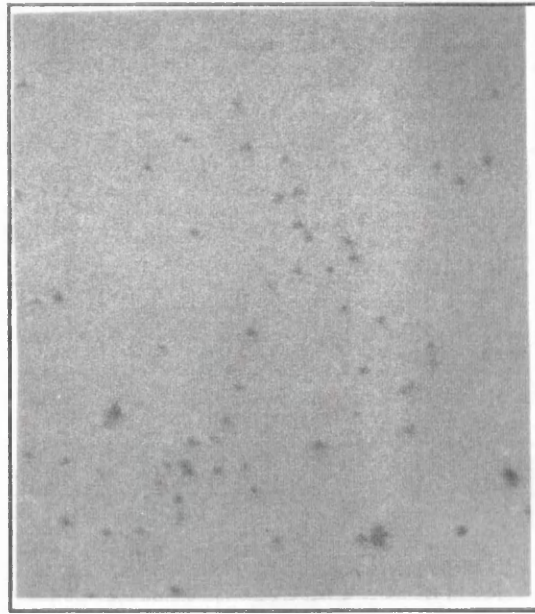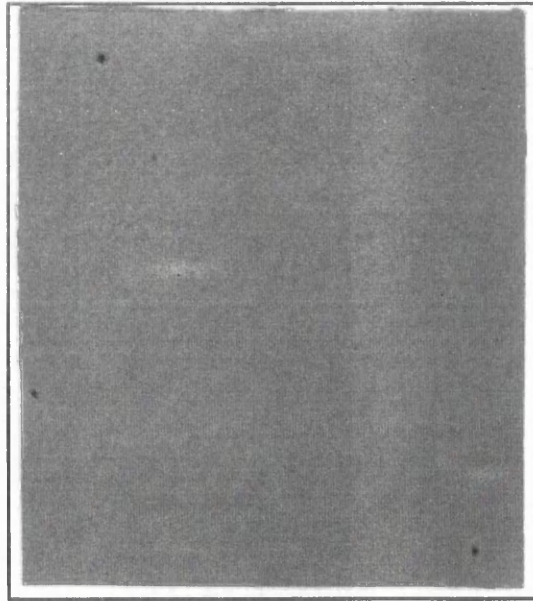
50μm

(b)

Figure 4.12. Normaski phase contrast image for InGaAs layers grown at substrate temperatures of (a) 565˚C and (b) 600˚C. The InGaAs layer grown at the higher substrate temperature has a mirror finish, while the layer grown at 565˚C contains many surface defects.

It has been shown in the previous chapter that the congruent limit of a material can be calculated from the point at which $p_{As_2}^L = p_{As_2}^S$ and that, for substrate temperatures above this congruent limit, preferential arsenic vaporisation leads to the production of metallic droplets on the surface. The excess arsenic partial pressure which has to be supplied in order to suppress the formation of indium droplets is thus given by :-

$$p_{As_2}^{Excess} = p_{As_2}^L - p_{As_2}^S \qquad (4.20)$$

The total arsenic partial pressure ($p_{As_2}^0 + p_{As_2}^{Excess}$) which is necessary for the growth of $In_{0.53}Ga_{0.47}As$ with no metallic droplet formation is shown in Figure 4.13 as a function of $1/T_S$.
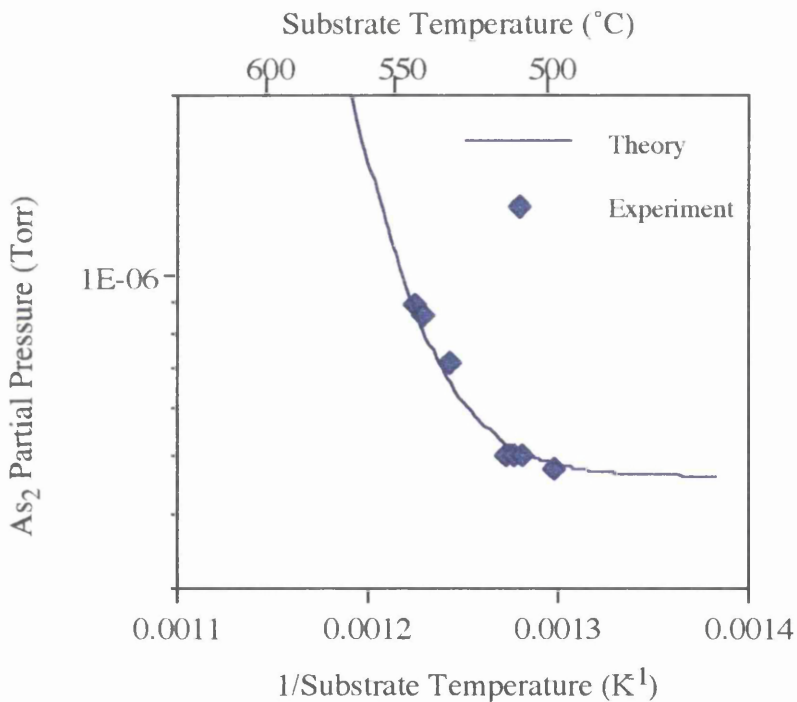
Figure 4.13. Theoretical and experimental As_2 partial pressures necessary for the growth of $In_{0.53}Ga_{0.47}As$ at $1\mu m/hr$ without surface indium droplet formation as a function of $1/T_C$.

The experimental points on this graph represent the transition temperature (T_c) between the upper and lower plateaux of the growth rate vs T_S curve as illustrated in Figure 4.4. Extremely good agreement is obtained between the theoretical prediction and the experimental results. The stabilising As_2 flux can therefore be accurately predicted for any substrate temperature.

4.5.3 In$_{0.52}$Al$_{0.48}$As

The partial pressure over the AlInAs solid solutions can be calculated as in the case of InGaAs, by treating the ternary alloy as a mixture of two binaries :

$$In_xAl_{(1-x)}As = xInAs + (1-x)AlAs \qquad (4.21)$$

For substrate temperatures below 700°C it is only necessary to consider the behaviour of the InAs component so the equation relating the partial pressures for the solid solution becomes, as before :

$$p_{As_2}^{\frac{1}{2}} p_{In} = \alpha_{InAs} K_{InAs} \qquad (4.22)$$

where α_{InAs} is the activity of InAs in the In$_{0.52}$Al$_{0.48}$As solid solution. No experimental data for this activity is available but, by comparison with In$_{0.53}$Ga$_{0.47}$As, it is possible to derive a figure from the high temperature indium desorption curve for In$_{0.52}$Al$_{0.48}$As. Figure 4.14 shows the experimental curves for the desorption of indium from In$_{0.52}$Al$_{0.48}$As and In$_{0.53}$Ga$_{0.47}$As together with the theoretical curves for activities of 0.29 and 0.15. The value of 0.15 is the best fit to the experimental In$_{0.52}$Al$_{0.48}$As data.
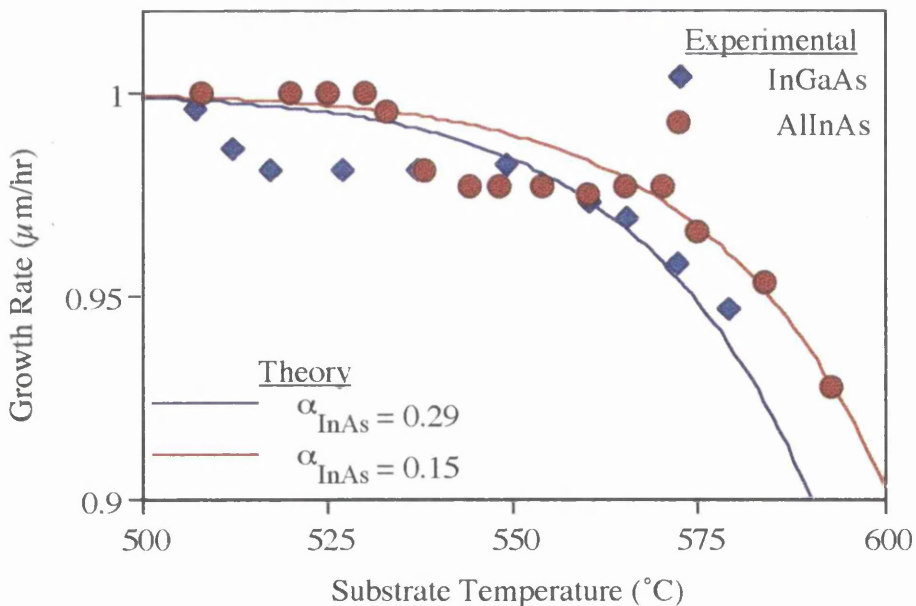
Figure 4.14. Growth rates of In$_{0.52}$Al$_{0.48}$As and In$_{0.53}$Ga$_{0.47}$As as a function of substrate temperature. The lines represent calculated desorption rates assuming an activity of 0.15 and 0.29.

The indium and arsenic partial pressures over the $In_{0.52}Al_{0.48}As$ solid solution calculated assuming an InAs activity of 0.15 are :

$$\ln p^S_{As_2} \text{ (atm)} = -31798 / T + 15.14 \qquad (4.23)$$

$$\ln p^S_{As_2} \text{ (atm)} = -31798 / T + 15.51 \qquad (4.24)$$

The overpressure of As_2 necessary to prevent the formation of indium droplets is given by equation 4.20. The dominant component of this excess pressure is the As_2 partial pressure over the diphasic mixture, however there is again no experimental data available for the activity of InAs in this mixture. The experimental results given in Figure 4.15 show that the As_2 overpressure necessary to stabilise an $In_{0.52}Al_{0.48}As$ surface is significantly less than that required for an $In_{0.53}Ga_{0.47}As$ surface. A fit to the $In_{0.52}Al_{0.48}As$ data gives an activity of 0.18 for InAs in the diphasic mixture. It should be noted that the value of α_{InAs} is the only adjustable parameter in the theoretical curve shown in Figure 4.15 and the fit to the experimental data obtained is excellent. Scott *et al* [25] have calculated, using Auger profiling techniques, that the In loss from $In_{0.53}Ga_{0.47}As$ was 3.3 times greater than that in $In_{0.52}Al_{0.48}As$. This value should be compared with the ratio between the diphasic activity of InAs in $In_{0.53}Ga_{0.47}As$ and the activity in $In_{0.52}Al_{0.48}As$ derived above :-

$$\frac{\alpha_{InAs}(InGaAs)}{\alpha_{InAs}(InAlAs)} = \frac{0.53}{0.18} = 2.94 \qquad (4.25)$$
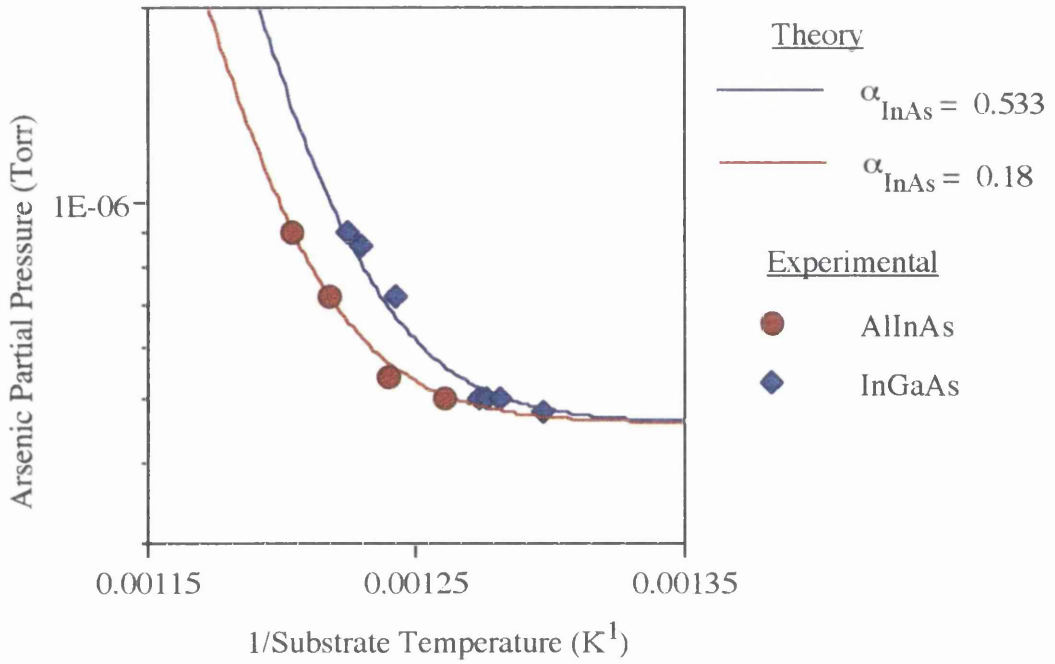
Figure 4.15. As$_2$ partial pressure necessary for growth of In$_{0.52}$Al$_{0.48}$As and In$_{0.53}$Ga$_{0.47}$As at 1μm/hr vs 1/T$_S$.

This value gives arsenic and indium partial pressures in the diphasic regime of :-

$$\ln p^L_{As_2} \ (atm) = -38166 \ / \ T + 25.43 \qquad (4.26)$$

and

$$\ln p^L_{In} \ (atm) = -28336 \ / \ T + 10.95 \qquad (4.27)$$
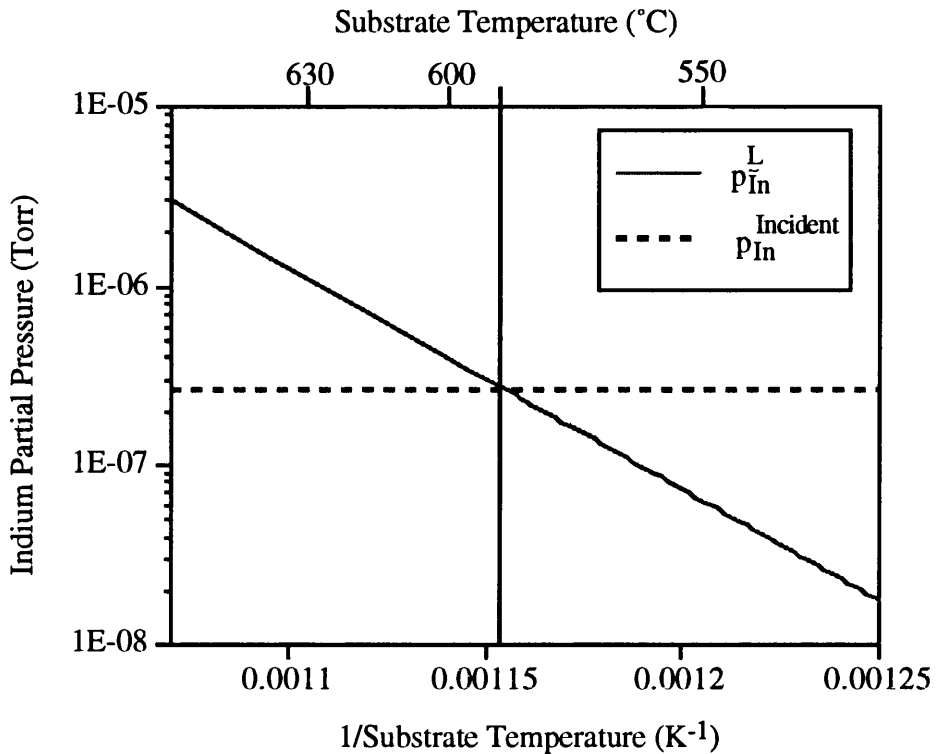
Figure 4.16. Indium partial pressure above the In-InAlAs liquidus as a function of $1/T_S$. The intercept with the incident partial pressure represents the maximum temperature at which indium droplets are stable on the InAlAs surface.

The incident In partial pressure and the partial pressure of In over the liquidus are shown as a function of $1/T_s$ in Figure 4.16. The intersection of these two lines gives a temperature of $590°C$ for the upper temperature limit of droplet formation during the growth of $In_{0.52}Al_{0.48}As$ at $1\mu m/hr$. This value is slightly higher than the value of $575°C$ previously calculated for $In_{0.53}Ga_{0.47}As$.

4.6 Growth of $In_{0.52}Al_{0.48}As$ at High Substrate Temperatures

The quality of MBE grown Al-containing alloys is very sensitive to the presence of contaminants in the growth environment. Oxygen, in particular, bonds very strongly with Al and has been identified as the main non-radiative recombination impurity in AlGaAs[26]. The incorporation of oxygen into AlGaAs can be minimised by using high (>650°C) substrate temperatures during growth. At high temperatures oxygen desorption aided by Ga desorption prevents oxygen accumulation on the surface and the resulting incorporation into the bulk[27]. It would be desirable to grow $In_{0.52}Al_{0.48}As$ layers at such high temperatures to

improve the quality of material, and take advantage of the absence of surface indium droplets and the potential for the 'self-locking' effect discussed previously.

The incident As_2 partial pressure for growth under such circumstances should be close to the minimum for low temperature growth, and the incident In partial pressure larger than that necessary to compensate for desorption from the solid solution. In addition, the substrate temperature must be above the point at which droplets are stable and in the regime where good surface morphology is obtainable.

To calculate the minimum permissible substrate temperature, it is necessary to take account of the additional In partial pressure required to compensate for In desorption. The criterion for droplet instability given in equation 4.19 must therefore be modified to include desorption from the solid solution, giving :-

$$p_{In}^{L} > p_{In}^{Growth} + p_{In}^{S} \qquad (4.28)$$

where p_{In}^{Growth} is the incident In partial pressure required for low temperature growth at the desired rate. This condition is shown graphically in Figure 4.17.
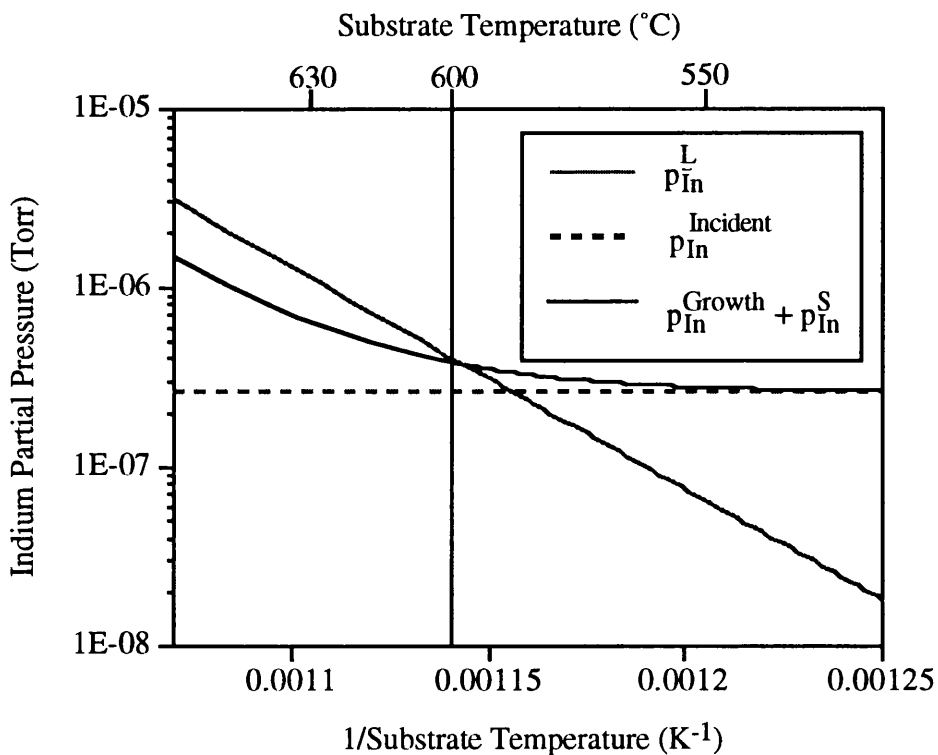
Figure 4.17. Indium partial pressure above the In-InAlAs liquidus as a function of $1/T_S$ The incident partial pressure includes a component to compensate for In desorption. The intercept represents the maximum temperature at which indium droplets are stable on the InAlAs surface.

The intercept between p_{In}^L and the total incident In flux ($p_{In}^{Growth} + p_{In}^S$) gives an upper temperature limit of $600°C$ for the stability of free In droplets.

The structure used for the growth of $In_{0.52}Al_{0.48}As$ at high T_S is shown in Figure 4.18. A thin buffer layer was first grown in the normal growth regime to protect the substrate from thermal decomposition. This was followed by 3ML of GaAs to prevent surface contamination and droplet formation during the interrupt necessary to raise T_S to $600°C$ and increase the In cell temperature to provide the additional In flux needed at this temperature. The In furnace setpoint temperature had previously been calibrated using RHEED intensity oscillations to provide an In flux of 10% in excess of that necessary to compensate for In desorption. An In calibration setpoint of $\approx 0.75\mu m/hr$ was used to give the required In partial pressure. $2\mu m$ of AlInAs were then grown at a T_S of $600°C$. The structure was completed by a 3ML GaAs interrupt protection layer followed by an $In_{0.53}Ga_{0.47}As$ cap grown at $525°C$.

100Å InGaAs Ts = 525°C	
	3ML GaAs
2μm AlInAs Ts≈600°C	
	3ML GaAs
0.1μm AlInAs Ts=525°C	
InP Substrate	
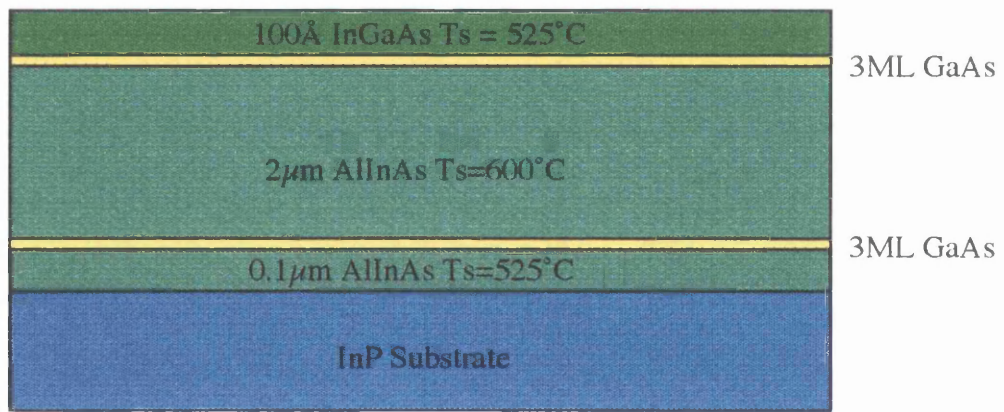
Figure 4.18. Schematic diagram of the structure used for the high temperature growth of $In_{0.52}Al_{0.48}As$

The surface morphology of the high temperature sample was completely smooth and featureless. The DCXD rocking curve for the sample is shown in Figure 4.19.
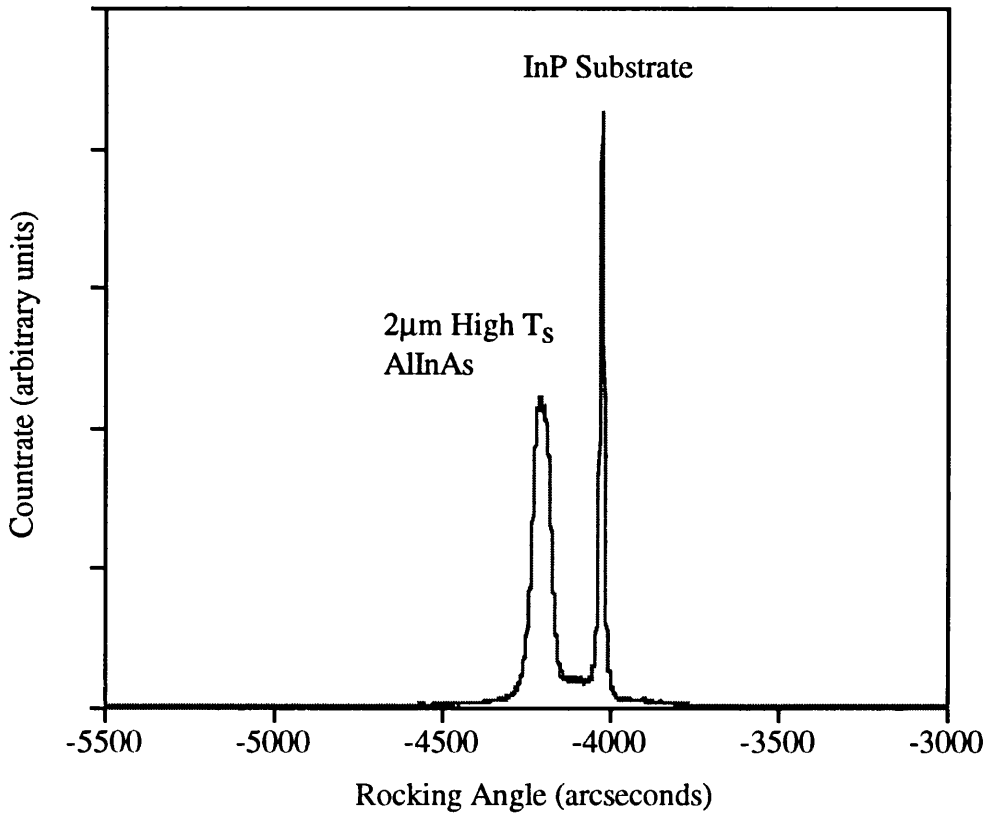
Figure 4.19. DCXD rocking curve for high T_S AlInAs sample.

The splitting between the substrate peak and the AlInAs peak is 188sec which corresponds to a composition of x=0.512. This is close to the room temperature lattice-matched composition of x=0.522. The small discrepancy may be due to thermal expansion of the InP substrate at the growth temperature of 600°C.

4.7 Conclusions

RHEED intensity oscillations can be used to calibrate the incident In, Ga and Al flux densities for the growth of $In_{0.53}Ga_{0.47}As$ and $In_{0.52}Al_{0.48}As$. The calibration points are found by converting the required flux densities into growth rates on InAs and GaAs substrates. The evaporation of indium from the ternary alloys appears to be influenced by the strain between the layer and the substrate which produces a slight shift from the expected calibration points and causes a change in the slope of the composition as a function of incident indium flux density around the lattice matched condition. If this effect is taken into account then reliable and repeatable control of the composition to a lattice mismatch of ±150ppm can routinely be achieved.

The onset of indium accretion on the surface of $In_{0.53}Ga_{0.47}As$ and $In_{0.52}Al_{0.48}As$ produces a drop in the growth rate measured by RHEED oscillations of the type seen for InAs. The drop in growth rate also coincides with a transition from an initial rise to an initial drop in the intensity of the RHEED oscillations at the commencement of growth. The formation of indium droplets on the surface can be suppressed by the use of an arsenic pressure in excess of that needed for growth. Calculations using existing thermodynamic data for $In_{0.53}Ga_{0.47}As$ are in good agreement with experimental measurements of the amount of excess arsenic which it is necessary to supply to prevent metallic droplet formation. In the case of $In_{0.52}Al_{0.48}As$, the lack of detailed thermodynamic data means that the activity of InAs in this material must be deduced from a fit to the experimental data. This yields an activity of 0.15 in the solid solution and 0.18 in the liquidus.

The desorption characteristics of $In_{0.52}Al_{0.48}As$ and $In_{0.53}Ga_{0.47}As$ suggest that there is an upper temperature limit above which droplets are not stable, and good morphology material can be grown. This is confirmed by experimental layers which have been grown at temperatures as high as 600°C with 'mirror' surfaces. There is also some evidence of a 'self-locking' effect at these temperatures caused by strain-induced In desorption.

4.8 References

1   'Characterisation of Insulated Gate $In_{0.53}Ga_{0.47}As/In_{0.52}Al_{0.48}As$
    Heterojunction Field-Effect Transistors'
    T.P. Leonard, J. Bregman, M. Pepper, G.J. Davies, E.G. Scott
    Journal Of Applied Physics 1991 Vol.70 No.9 pp.5090-5094

2   'High-Performance $In_{0.52}Al_{0.48}As/In_{0.53}Ga_{0.47}As$ HFETs'
    H. Dambkes, P. Marschall, Y.H. Zhang, K. Ploog
    Electronics Letters 1990 Vol.26 No.7 pp.488-490

3   '$In_{0.52}Al_{0.48}As/In_{0.53}Ga_{0.47}As$ Resonant Tunnelling Diodes with Large
    Current Peak Valley Ratio'
    A.A. Lakhani, R.C. Potter, D. Beyea, H.H. Hier, E. Hempfling, L. Aina and
    J.M. O'Connor
    Electronics Letters 1988 Vol.24 No.3 pp.153-154

4 "The Effect of Interface and Alloy Quality on the DC and RF Performance of
$In_{0.53}Ga_{0.47}As$-$In_{0.52}Al_{0.48}As$ HEMTs'
A.S. Brown, U.K. Mishra, S.E. Rosenbaum
IEEE Transactions On Electron Devices 1989 Vol.36 No.4 pp.641-645

5 'High-Performance $In_{0.52}Al_{0.48}As$/$In_{0.53}Ga_{0.47}As$ MSM-HEMT Receiver
OEIC Grown By MOCVD on Patterned InP Substrates'
W.P. Hong, G.K. Chang, R. Bhat, J.L. Gimlett, C.K. Nguyen, G. Sasaki
and M. Koza
Electronics Letters 1989 Vol.25 No.23 pp.1561-1563

6 'Double Junction $In_{0.52}Al_{0.48}As$/$In_{0.53}Ga_{0.47}As$ Multiquantum Well
Avalanche Photodiodes
Y. Lebellego, J.P. Praseuth, A. Scavennec
Electronics Letters 1991 Vol.27 No.24 pp.2228-2230

7 'New High-Speed Long-Wavelength $In_{0.52}Al_{0.48}As$/$In_{0.53}Ga_{0.47}As$
Multiquantum Well Avalanche Photodiodes'
K. Mohammed, F. Capasso, J. Allam, A.Y. Cho, A.L. Hutchinson
Applied Physics Letters 1985 Vol.47 No.6 pp.597-599

8 '1.5-1.6μm $In_{0.53}Ga_{0.47}As$/$In_{0.52}Al_{0.48}As$ Multiquantum Well Lasers Grown
by Molecular-Beam Epitaxy'
H. Temkin, K. Alavi, W.R. Wagner, T.P. Pearsall, A.Y. Cho
Applied Physics Letters 1983 Vol.42 No.10 pp.845-847

9 'Growth of $In_{0.53}Ga_{0.47}As$/InP Heterostructures by Molecular Beam Epitaxy'
B.I. Miller and J.H. McPhee
Journal of the Electrochemical Society 1978 Vol.125 No.8 pp1310-1317

10 'Molecular-Beam Epitaxial-Growth of Uniform $In_{0.53}Ga_{0.47}As$ on InP with a
Coaxial In-Ga Oven'
K.Y. Cheng, A.Y. Cho, W.R. Wagner, W.A. Bonner
Journal Of Applied Physics 1981 Vol.52 No.2 pp.1015-1021

11 'Molecular-Beam Epitaxial-Growth of Uniform $In_{0.53}Ga_{0.47}As$ with a
Rotating Sample Holder
K.Y. Cheng, A.Y. Cho, W.R. Wagner
Applied Physics Letters 1981 Vol.39 No.8 pp.607-609

12 'Growth of Extremely Uniform Layers by Rotating Substrate Holder with
Molecular-Beam Epitaxy for Applications to Electro-Optic and Microwave
Devices'
A.Y. Cho, K.Y. Cheng
Applied Physics Letters 1981 Vol.38 No.5 pp.360-362

13 'Temporal Intensity Variations in RHEED Patterns During Film Growth of
GaAs by MBE'
P.J. Dobson, N.G. Norton, J.H. Neave, B.A. Joyce
Vacuum 1983 Vol.33 No.10 pp.593-596

14 'Molecular-Beam Epitaxial Group III Arsenide Alloys'
C.E.C. Wood, D.V. Morgan, L. Rathbun
Journal of Applied Physics 1982 Vol.53 No.6 pp4524-4526

15 'Physics of Thin Films'
Edited by G. Haas and M. Francombe
(Academic, New York, 1980) p35

16 'Optical-Quality GaInAs Grown by Molecular-Beam Epitaxy'
G. Wicks, C.E.C. Wood, H. Ohno, L.F. Eastman
Journal Of Electronic Materials 1982 Vol.11 No.2 pp.435-440

17 'Molecular Beam Epitaxial Growth and Structural Design of
$In_{0.52}Al_{0.48}As/In_{0.53}Ga_{0.47}As/InP$ HEMTs'
Yi-Ching Pao and J.S. Harris
Journal Of Crystal Growth 1991 Vol.111 No.14 pp.489-494

18 'Evaporation from Solids'
Edited by N.B. Hannay
(Plenum, New York, 1967)

19 'Thermodynamic Analysis Of Molecular-Beam Epitaxy Of III-V Compounds
-Application To The $Ga_xIn_{1-x}as$ Multilayer Epitaxy'
J.Y. Shen, C. Chatillon
Journal Of Crystal Growth 1990 Vol.106 No.4 pp.553-565

20 'Thermodynamic Aspects of Molecular-Beam Epitaxy - High-Temperature
Growth in the $GaAs/Al_xGa_{1-x}As$ System'
R. Heckingbottom
Journal of Vacuum Science Technology 1985 Vol.3 No.2 pp572-575

21 'Mass-Spectrometric Evidence Of Instability In $In_xGa_{1-x}As$ Compounds
-Activity Measurements Of InAs'
M. Tmar and C. Chatillon
Journal of Crystal Growth 1988 Vol.89 No.4 pp.501-510

22 'Thermodynamical Properties of Indium and Gallium Arsenides from
Measurements of Electromotive Forces'
E.M. Solopai, V.B. Ufimtsev and A.N. Krestovnikov
Russian Journal of Physics 1971 Vol.45 No.10 pp1504-1507

23 'Thermodynamical Properties of InAs-GaAs Solid Solutions'
A.N. Krestovnikov, V.B. Ufimtsev
Doklady Akademii Nauk SSSR 1973 Vol.208 pp365-368

24 'Thermodynamic analysis of Segregation Effects in MBE of A^{III}-B^V
Compounds'
S.V. Ivanov, P.S. Kop'ev and N.N. Ledentsov
Journal of Crystal Growth 1991 Vol. 111 No.12 pp151-161

25 'MBE Growth Of Ga-Al-In-As Ternary And Quaternary Alloy Compositions'
E.G. Scott, D.A. Andrews, G.J. Davies
Journal Of Crystal Growth 1987 Vol.81 No.1-4 pp.296-297

26 'Photoluminescence Killer Center in AlGaAs Grown By Molecular-Beam
Epitaxy'
K. Akimoto, M. Kamada, K. Taira, M. Arai and N. Watanable
Journal of Applied Physics 1986 Vol.59 No.8 pp.2833-2836

27 'Role of substrate temperature in molecular-beam epitaxial growth of high-power GaAs/AlGaAs lasers'

S.V. Iyer, H.P. Meier, S. Ovadia, C. Parks, D.J. Arent and W. Walter

Applied Physics Letters 1992 Vol.60 No.4 1992 pp416-418

Chapter 5

The Optical and Electrical Properties of Undoped $In_{0.53}Ga_{0.47}As$ and $In_{0.52}Al_{0.48}As$ Grown by MBE

5.1 Optical Properties

5.1.1 Introduction

Photoluminescence (PL) spectroscopy[1,2] is a method which is frequently employed to assess the optical properties of MBE grown layers and identify low level impurities present in the layers[3]. Samples are illuminated (normally with a laser) to produce excess carriers in the semiconductor material by photon absorption. The excess carriers subsequently recombine and, if the material has a direct bandgap, then the recombination process may result in the emission of a photon. Residual impurities in the layer produce states within the forbidden energy gap of the material which can bind electrons, holes, or excitons (electron-hole pairs held together by coulombic interaction). The recombination of such bound carriers gives rise to a sharp peak in the PL spectrum at an energy which is characteristic of the impurity atoms involved in the transition. The most important types of transition are:-

(1) *Excitonic emission*, due to the recombination of an electron hole pair. The highest energy transition is produced by the recombination of free excitons, followed by transitions involving the recombination of excitons bound to neutral or ionized donor and acceptor impurities.

(2) *Free-to-bound emission*, due to the recombination of a conduction band electron with an acceptor-bound hole or alternatively to the recombination of a donor-bound electron with a valence band hole.

(3) *Donor-acceptor emission*, due to the recombination of an electron bound to a donor atom with a hole bound to an acceptor atom. The donor and acceptor atoms are both ionized by this transition.

There are, in addition to the near-bandedge transitions mentioned above, quite frequently transitions at much lower energies which are produced by either deep impurity levels close to the middle of the bandgap or structural imperfections in the crystal. These transitions are, in general, less well understood than shallower transitions and peak assignment is much less certain.

5.1.2 Experimental Setup

PL measurements were used to assess the optical quality of the bulk material. A schematic of the experimental apparatus is shown in Figure 5.1. The specimens were mounted on a cold finger inside a vacuum system and illuminated with the 4876Å line of an argon ion laser. The incident power of the laser beam was typically 13mW (corresponding to an intensity of $\approx 1.5 Wcm^{-2}$). The emitted luminescence was filtered to exclude the excitation wavelength and focused onto the entrance slits of a Monospek 2 metre grating monochromator. The slit size used was, in most cases, 0.05mm giving an energy resolution of <1meV. The light was detected by a liquid nitrogen cooled germanium photodetector. The incident beam was chopped at a frequency of 40Hz, enabling a lock-in amplifier system to be used to suppress noise. A PC was used to control the lock-in amplifier and acquire the amplified photodetector signal. The software for the acquisition, manipulation and plotting of the data from the lock-in amplifier was written during the course of this PhD. Hardware was also constructed to enable the PC to control the motor drive of the monochromator. The monochromator wavelength was ramped continuously during a spectrum acquisition cycle and the wavelength corresponding to an amplifier reading was calculated from the ramp speed and the elapsed time. This method eliminated the effects of whiplash in the monochromator drive mechanism. The number of sample points was fixed at 2000 points for each spectrum.
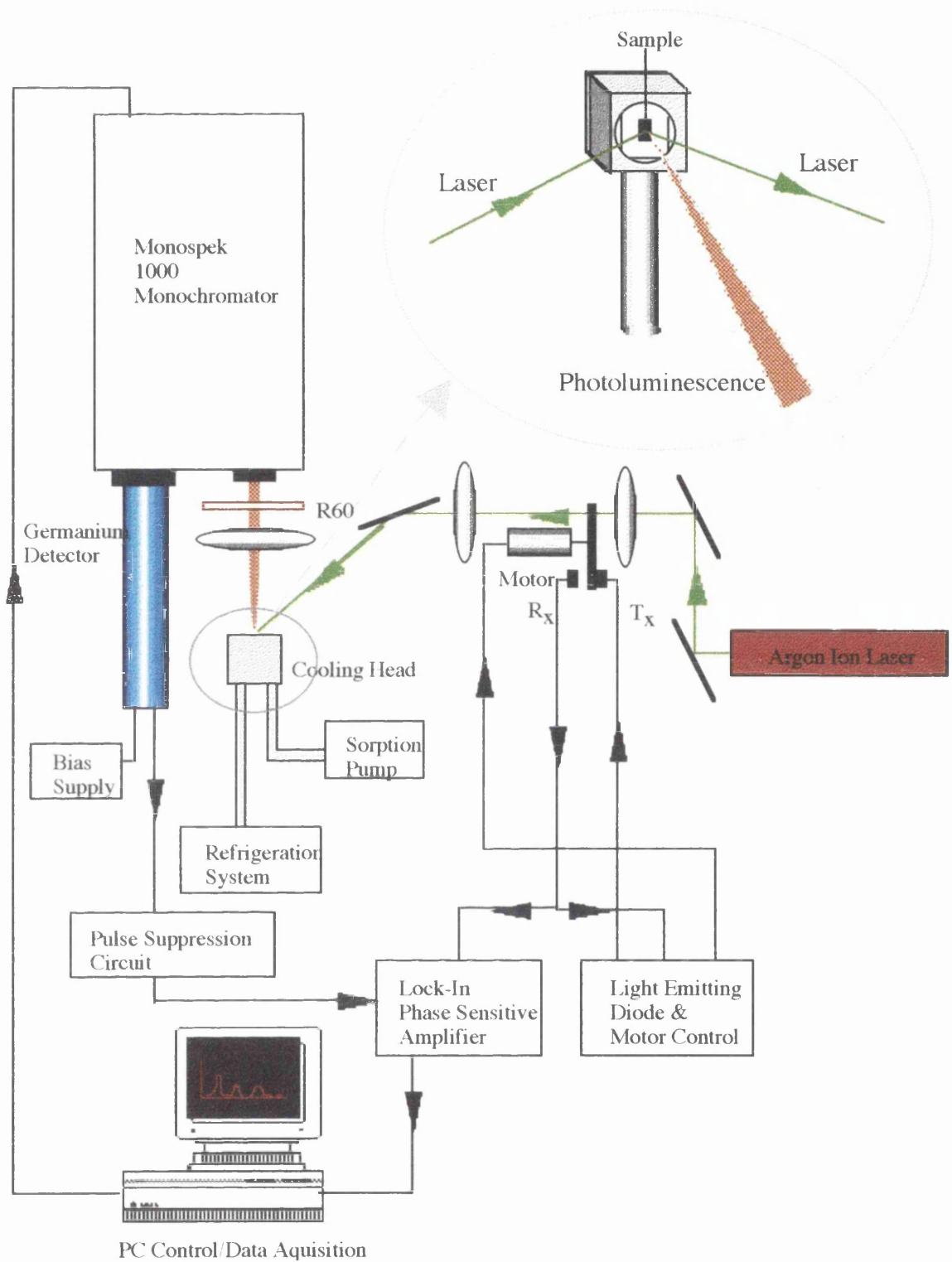
Figure 5.1. Experimental apparatus used to examine photoluminescence properties of epitaxial layers.

5.1.3 In$_{0.53}$Ga$_{0.47}$As PL Spectra

Figure 5.2 shows a typical example of the PL spectra obtained for initial attempts at the growth of In$_{0.53}$Ga$_{0.47}$As samples lattice matched to InP substrates. These samples were grown with V:III pressure ratios of approximately 25:1, which is at the lower end of the values commonly used in the literature[4,5,6] but is significantly higher than the subsequently discovered minimum possible flux ratio. Three distinct peaks were present in the PL spectra. These have been labelled 1, 2 and 3.
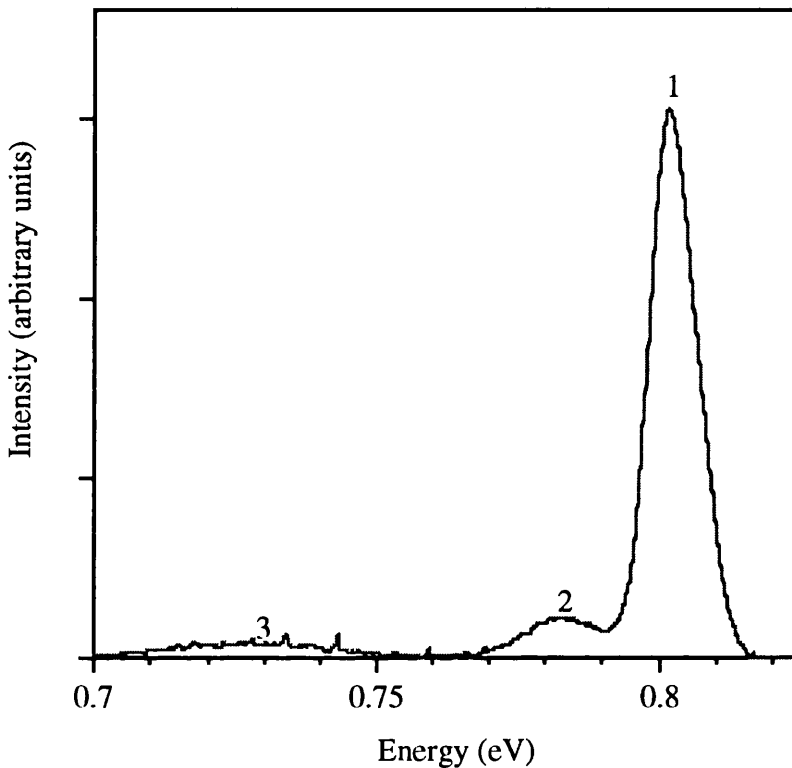
Figure 5.2. Typical PL spectrum obtained for initial attempts at the growth of In$_{0.53}$Ga$_{0.47}$As lattice matched to InP.

The spectrum is dominated by a donor bound exciton peak (Peak 1) at around 0.8eV with a linewidth of ≈5meV. The lattice mismatch measured by DCXD is shown as a function of the energy of the main peak in Figure 5.3 for a series of layers. Data obtained by Bassignana *et al*[7] for the luminescence from InGaAs grown on S-doped InP substrates is also shown on this graph. The two sets of data are in good agreement.

92
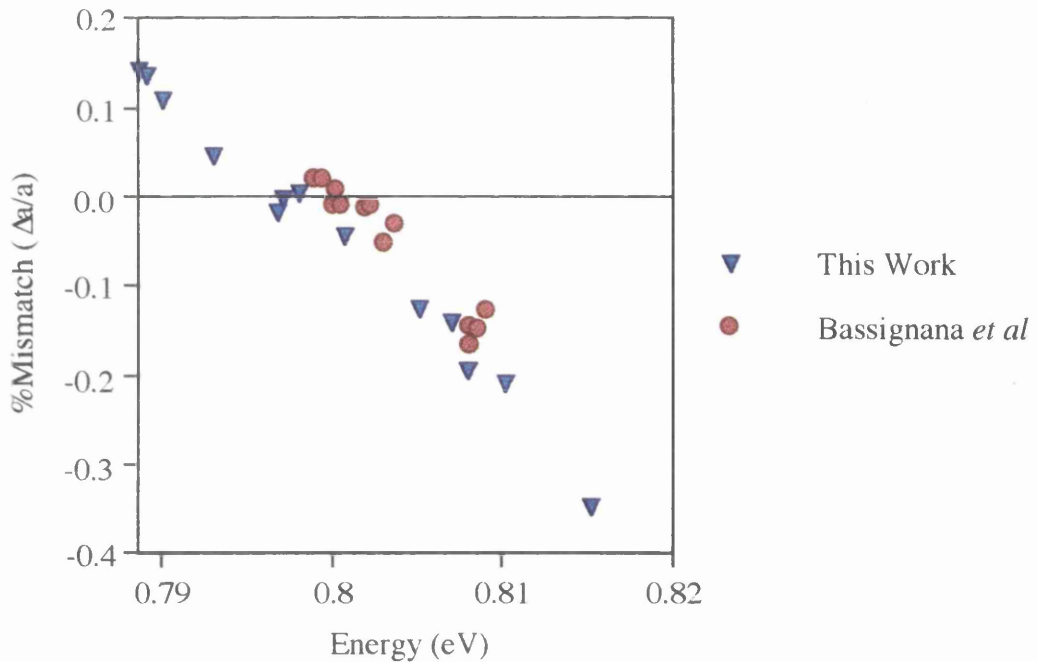
Figure 5.3. Relative mismatch percentage vs main PL peak energy for InGaAs on InP at 9K. The solid circles represent data from Bassignana *et al* for 1μm InGaAs on S-doped InP.

The peak at ≈0.73eV (Peak 3) was not found in all of the samples and is thought to be related to the process used to remove the surface oxide as the intensity of the peak was found to vary with the de-oxidisation method employed before growth was commenced.

Three methods of pre-growth oxide desorption were employed. The first used a slow ramp of the substrate temperature in the growth chamber while stabilising the surface with an arsenic flux. A weak (2x1) reconstruction was obtained at temperatures above ≈420°C. This became a (2x3) or less frequently a (2x4) reconstruction when a temperature of ≈ 520°C was reached. The oxide desorption did not take place abruptly as is the case with oxide desorption under a P_2 flux, rather the (2x3) or (2x4) reconstruction appeared slowly as the substrate remained at the oxide desorption temperature. There was no sharp transition and it was not therefore possible to determine conclusively by RHEED at which point the surface oxide was completely gone. This method of oxide desorption was found to be a little uncertain, and the PL spectrum for samples grown using this method frequently contained a large deep level peak.

The second method again used a slow substrate temperature ramp however the temperature was raised until the surface reconstruction became a clear (4x2) pattern at ≈560°C. At this point the substrate temperature was immediately lowered to the desired growth temperature and growth was commenced as soon as the substrate temperature had stabilised. This method is widely used in the literature and has been shown to give improvements in substrate cleanliness. It was found that

this technique had a tendency to produce irreversible decomposition of the InP substrate and caused the appearance of metallic droplets before the commencement of growth. This may have been due to the use of much lower arsenic fluxes than those commonly quoted in the literature.

The method of heat cleaning which was found to be the most reliable was to leave the substrate at a temperature of 400°C without an arsenic overpressure for an extended period of time. This was normally carried out on the buffer chamber high temperature degas (HTD) stage. The substrate was typically heated for a period of 4 hours or more. When transferred to the growth chamber, a good (2×4) reconstruction was immediately obtained. The PL spectra for $In_{0.53}Ga_{0.47}As$ layers grown on InP substrates treated in this way did not contain the deep level peak.

The energy of the remaining peak (Peak 2) varied quite markedly from sample to sample. The energy difference (ΔE) between this peak and the main bound exciton peak appeared to scale with the amount of lattice mismatch between the layer and the substrate. This is illustrated in Figure 5.4. Two spectra are shown for samples with In proportions (measured by DCXD) of 0.528 and 0.523. The spectra have been normalised with respect to the main donor-bound exciton peak, to show more clearly the energy difference between the main and subsidiary peak.
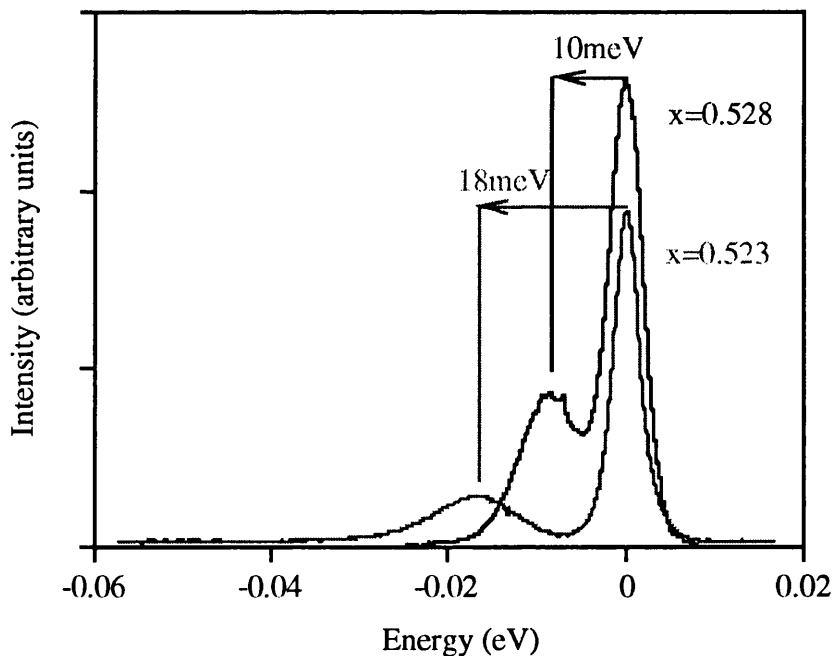
Figure 5.4. Spectra for two slightly mismatched $In_xGa_{(1-x)}As$ samples grown on InP. The spectra have been normalised with respect to the main donor-bound exciton peak.

Wicks et al [8] have reported the presence of secondary peaks in the PL spectrum of InGaAs at energies between 15 and 50meV below the exciton peak.

The peaks were only obtained for V:III pressure ratios ≤ 30:1 and were attributed to radiative transitions involving arsenic vacancy complexes. This explanation is, however, unsatisfactory since the RHEED reconstruction during $In_{0.53}Ga_{0.47}As$ growth has been observed to remain an As-stable (2×4) pattern at pressure ratios much smaller than 30:1.

An alternative explanation for the secondary peaks is that they are due to a indium enhancement of the surface composition produced by segregation. Sobiesierski et al [9] have demonstrated the presence of luminescence from a surface quantum well on InP substrates which had been heat-cleaned under a stabilising arsenic flux. Oxide removal in such circumstances results in the the exchange of P for As atoms, leading to the formation of a thin pseudomorphic InAs layer[10,11] which produces a well-defined peak in the PL spectrum of the material. The possibility that the secondary peak was produced by an analagous segregation enhancement of the surface In composition was investigated by etching an InGaAs sample for 30s in H_3PO_4:8 H_2O_2: $60H_2O$ which has an $In_{0.53}Ga_{0.47}As$ etch rate of $0.2\mu m/min$[12]. A PL spectra was taken for the etched material and an immediately adjacent piece of the material which remained unetched. The PL spectra obtained for the two adjacent InGaAs samples, one etched and the other unetched, are shown in Figure 5.5. The secondary peak is not present in the etched sample confirming that the peak was due to a surface layer which was removed by the etch. This suggests that the subsidiary peak is due to the formation of an indium rich surface segregation layer on top of the InGaAs layer. The use of very high arsenic overpressures reduces the surface mobility of In atoms and suppresses the formation of a segregation layer; when the arsenic overpressure is reduced the In surface mobility increases and a segregation layer becomes measurable. The presence of the secondary peak is therefore a consequence of the relatively low As_2 overpressure used for the growth of the alloys. This does not, however give us the complete picture. There is, as is shown in Figure 5.5, a very strong relationship between ΔE and the mismatch between the InGaAs layer and the InP substrate.
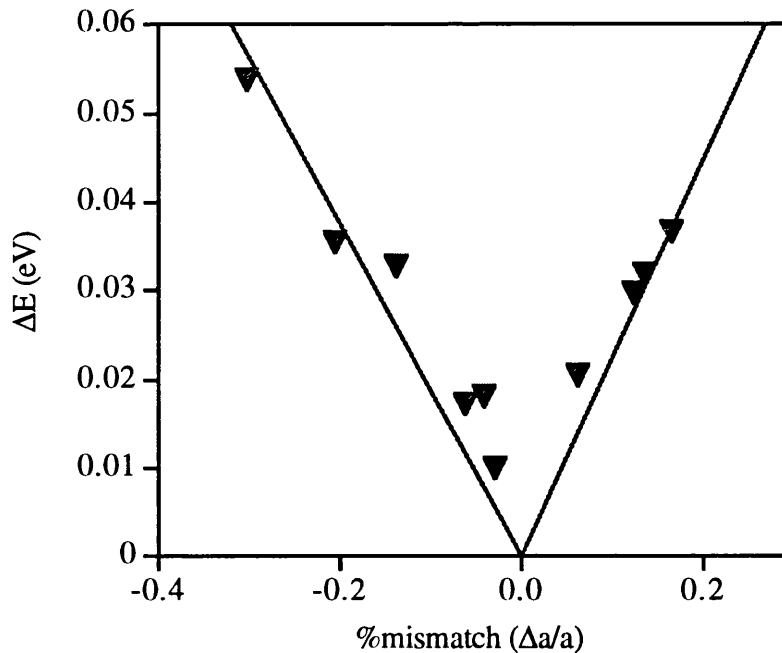
Figure 5.5. Difference in energy (ΔE) between main bound exciton and adjacent peak vs diffference between measured indium composition and lattice matched condition.

The splitting between the main and subsidiary peaks varies linearly with the layer-substrate mismatch. At very low mismatch values (<0.05%) no secondary peak was observed in the PL, indicating that the segregation layer is either :-

a) no longer present.

b) too narrow to provide confinement.

c) too close to the bulk composition to provide confinement.

d) a combination of b) and c)

In any case it is apparent that the amount of segregating indium is significantly influenced by the existence of even very small amounts of strain in the MBE layer.
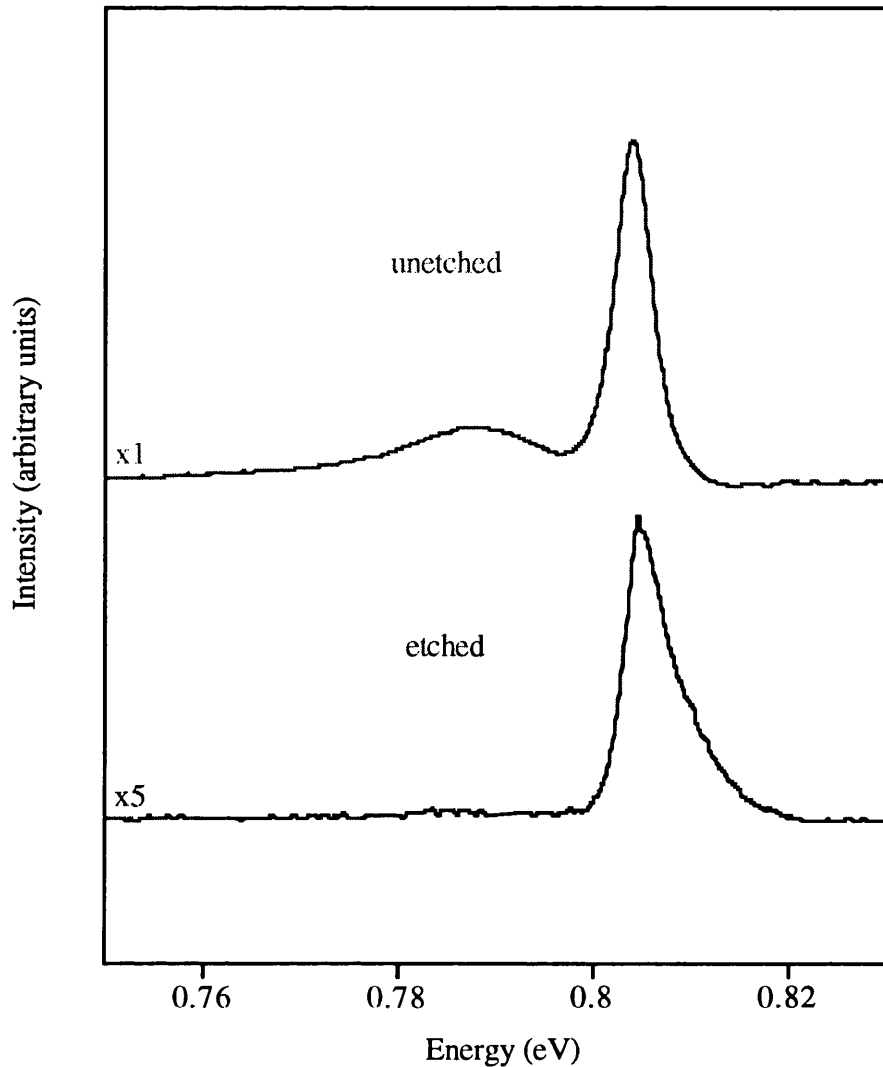
Figure 5.6. PL spectra for two adjacent InGaAs samples. The sample corresponding to the bottom spectrum has been etched to remove the top $0.1\mu m$ of the MBE material.

Many authors have shown the existence of surface segregation processes which produce surface compositions which are Ga enriched for the growth of $Al_xGa_{(1-x)}As$, and In enriched for the growth $In_xGa_{(1-x)}As$. These processes can, in some cases, result in the formation of purely binary surfaces[13,14]. Gerard[15] has measured the indium content of the surface monolayer of strained $In_xGa_{(1-x)}As$ and $In_xAl_{(1-x)}As$ on GaAs and demonstrated that the indium content rises sharply during the initial few monolayers of growth, confirming that the indium enrichment of the surface layer is produced at the expense of these first monolayers. The commencement of growth produces a gradient between a composition which is initially indium deficient and one which corresponds to the ratio of the impinging group III fluxes. After the growth of this graded layer the surface composition is in equilibrium with the bulk and the fluxes incorporating into the bulk are identical to

the impinging fluxes. The surface layer is, at this point, In-rich in comparison with the bulk and subsequent growth occurs through this In-rich layer. The variation of In-composition with depth of a bulk InGaAs layer is shown schematically in Figure 5.7.
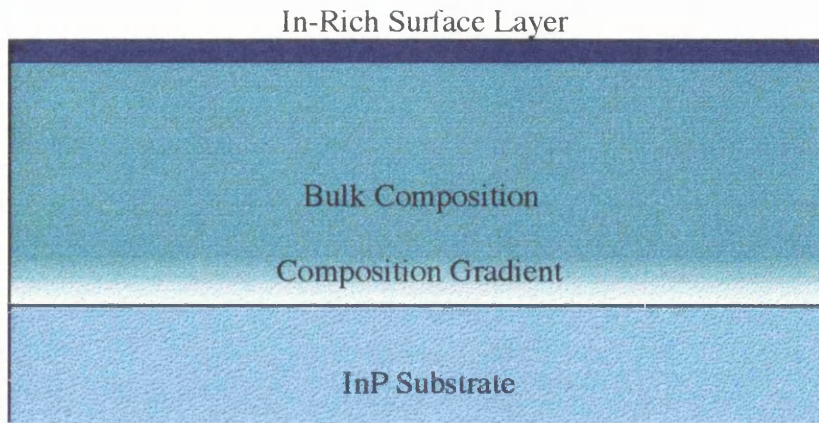
Figure 5.7. Schematic diagram of the variation in composition produced by In segregation during growth of a bulk InGaAs layer .

The thickness of the surface segregation layer of the MBE-grown $In_xGa_{(1-x)}As$ was estimated from the energy of the secondary peak. The assumptions were made that the surface layer was composed of InAs and the shape of the potential well formed by the surface layer could be approximated by a square well shape. The calculated well thicknesses corresponding to the measured secondary peak energies are shown in Figure 5.8 as a function of the percentage mismatch between the bulk composition and the InP substrate. The calculated layer thicknesses vary between 4.5Å at -0.05% mismatch and 10.5Å at 0.17% mismatch. These values demonstrate that the surface segregation layers are not confined to the topmost surface monolayer as many segregation models assume, but are in fact composed of several monolayers.
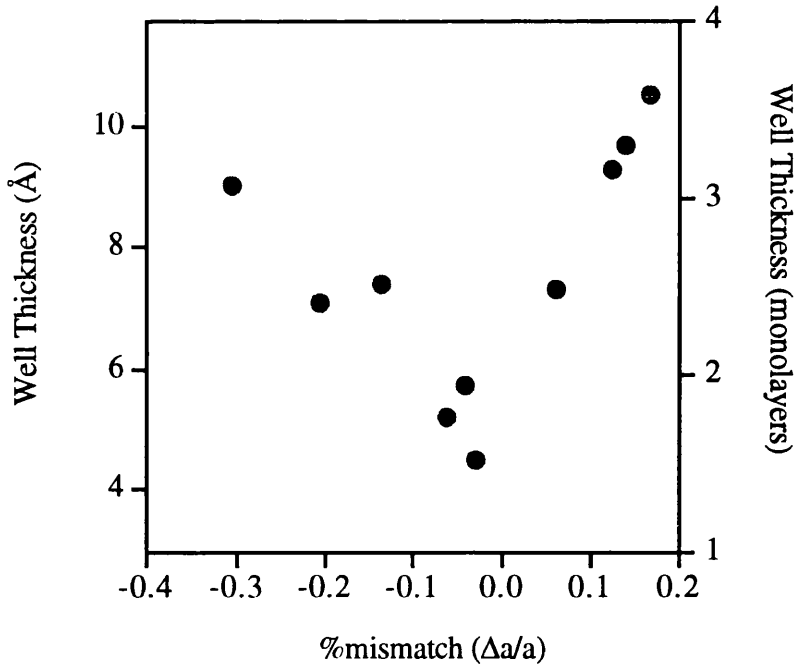
Figure 5.8. Thickness calculated from secondary peak energies of well formed by In surface segregation during InGaAs growth on InP. The segregation layers were assumed to be composed of InAs and to have an approximately square shape.

It should be noted that the thickness of the surface segregation layer does not tend to zero at the lattice matched composition. The intersection of the slopes on either side of lattice match suggests that a segregation layer ≈4Å thick is present even for 0% mismatch. This is in good agreement with X-ray photoemission spectroscopy (XPS) results obtained by Massies *et al* [16] who have reported an $In_xGa_{(1-x)}As$ segregation layer corresponding to 2ML of InAs. It seems likely that the explanation for the disappearance of the secondary peak in the PL spectrum at the lattice matched condition is the lack of confinement produced by such a narrow well width rather than the complete absence of any segregation layer.

Figure 5.9 shows a typical luminescence spectrum for an exactly lattice matched $In_{0.53}Ga_{0.47}As$ layer grown using the optimised oxide removal process and minimum As_2 flux. The spectrum contains only one peak corresponding to a neutral donor bound exciton transition. The FWHM linewidth of the peak is 3.2meV which is comparable with the best reported value of 1.2meV[17]. There is no evidence of the segregation layer seen on slightly strained InGaAs samples.

99
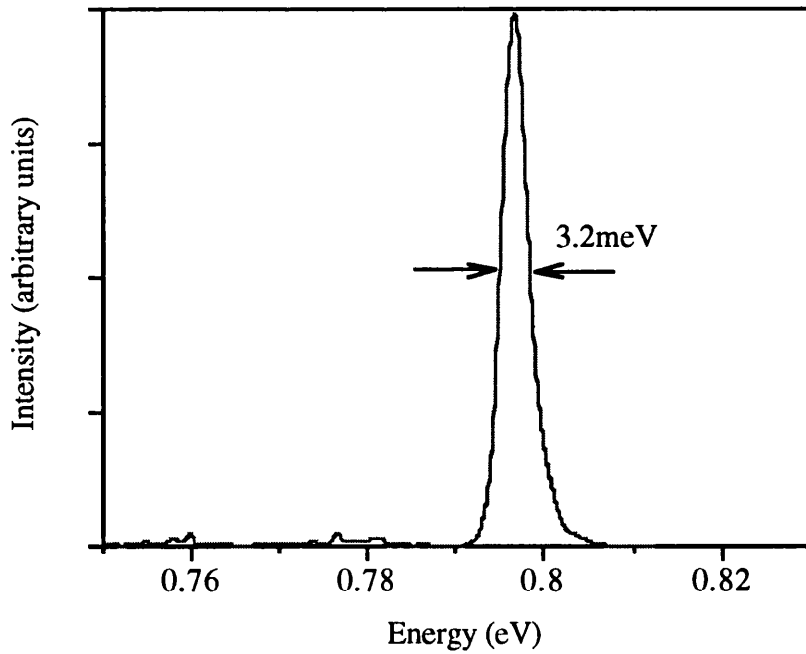
Figure 5.9. Photoluminescence spectrum for $In_{0.53}Ga_{0.47}As$ lattice matched to InP.

The preceding samples were grown under conditions where there was no accumulation of indium droplets on the surface. The formation of an indium segregation layer is therefore a separate effect which can occur even in material which has a mirror finish. The segregation layer is not, however, confined to the good morphology regime: growth in the In accumulation regime also results in the formation of an In rich surface layer. Figure 5.10 shows the $In_{0.53}Ga_{0.47}As$ growth rate as a function of substrate temperature for an As_2 partial pressure of 2.7×10^{-7} Torr. Immediately after this measurement was performed, a $1\mu m$ thick InGaAs sample was grown at a substrate temperature of 565°C - well into the indium accumulation regime.
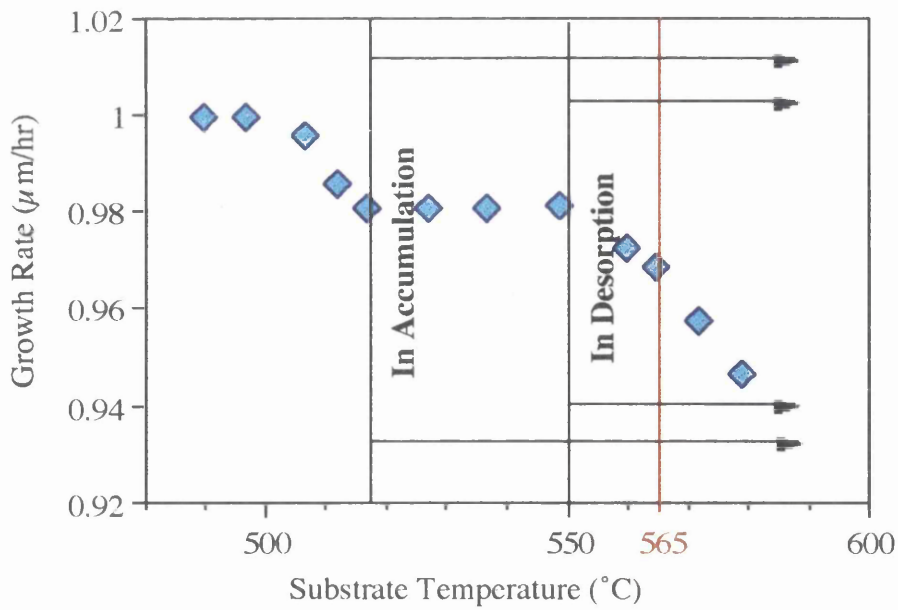
Figure 5.10. InGaAs growth rate as a function of substrate temperature for an As$_2$ pressure of 2.7 × 10^{-7} Torr.
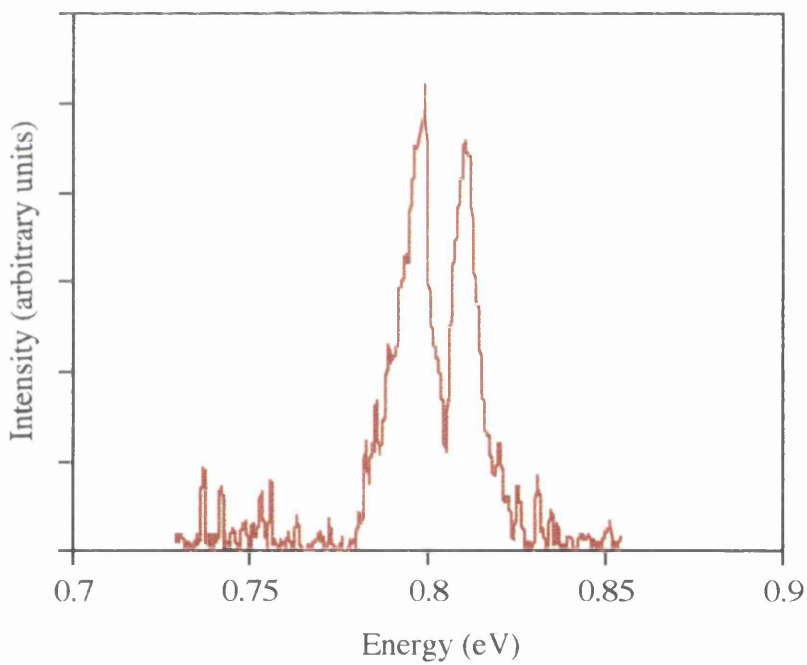
Figure 5.11. PL spectrum for InGaAs grown in the indium droplet accumulation regime.

The PL spectrum obtained for this sample is shown in Figure 5.11. The intensity of the PL signal was considerably smaller than that for samples with good morphology, but it can be seen that 2 peaks were obtained at energies of 0.795eV and 0.810eV. The lower energy peak indicates the presence of an In-rich surface layer. The mismatch between the bulk material and the InP substrate was measured by DCXD and found to be 0.2%, corresponding to a composition of x=0.502. This value is identical to the mismatch derived from Figure 5.3 using the measured peak energy of 0.810eV. There is, however a discrepancy between the measured position of the secondary peak and the position predicted from Figure 5.5. The expected value of ΔE for a mismatch of 0.2% is 35meV while the measured value is only 15meV. The difference is probably due to the desorption of InAs from the surface segregation layer. From Figure 4.6 it is apparent that, at a substrate temperature of 565°C, significant In desorption is taking place. This will lower the amount of surface In, producing a reduced segregation layer thickness and hence a smaller than expected value of ΔE.

5.1.4 In$_{0.52}$Al$_{0.48}$As PL Spectra

The PL spectra of In$_{0.52}$Al$_{0.48}$As indicated poorer quality material than had been obtained for In$_{0.53}$Ga$_{0.47}$As. The main peak obtained was broad in comparison to the sharp excitonic peak observed in In$_{0.53}$Ga$_{0.47}$As spectra, with linewidths of 25-35meV. A typical PL spectrum is shown in Figure 5.12.
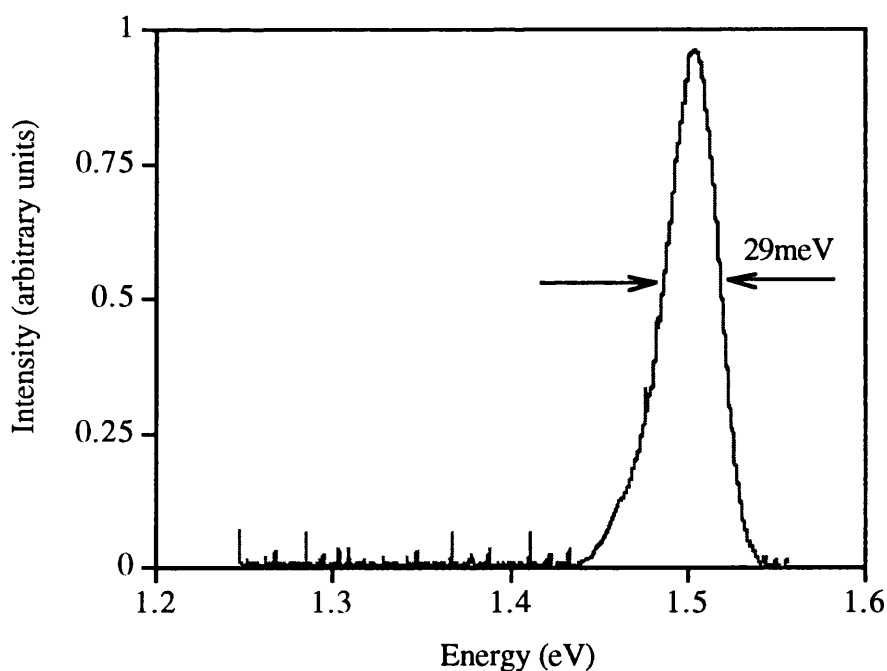
Figure 5.12. Photoluminescence spectrum for 2µm of In$_{0.52}$Al$_{0.48}$As lattice matched to InP.

The reduction in layer quality is presumed to be due to the presence of Al in the alloy and the resultant increase the incorporation of impurities, especially oxygen. Several studies have shown that the presence of Al in alloy layers results in the degradation of the optical and electrical quality of the material. In the case of $Al_xGa_{(1-x)}As$ this problem has been addressed by performing growth at substrate temperatures of $700°C$ or above in order to desorb impurities bound to Al atoms and prevent their incorporation into the bulk. $In_{0.52}Al_{0.48}As$ is normally grown at a substrate temperature of $\approx530°C$ which is considerably lower than is desirable.

The PL peak energy as a function of the composition measured by DCXD is shown in Figure 5.13. The data is in good agreement with a cathodoluminescence study performed by Davies et al [18]. The PL peak energy obtained for the lattice matched condition was 1.50eV.
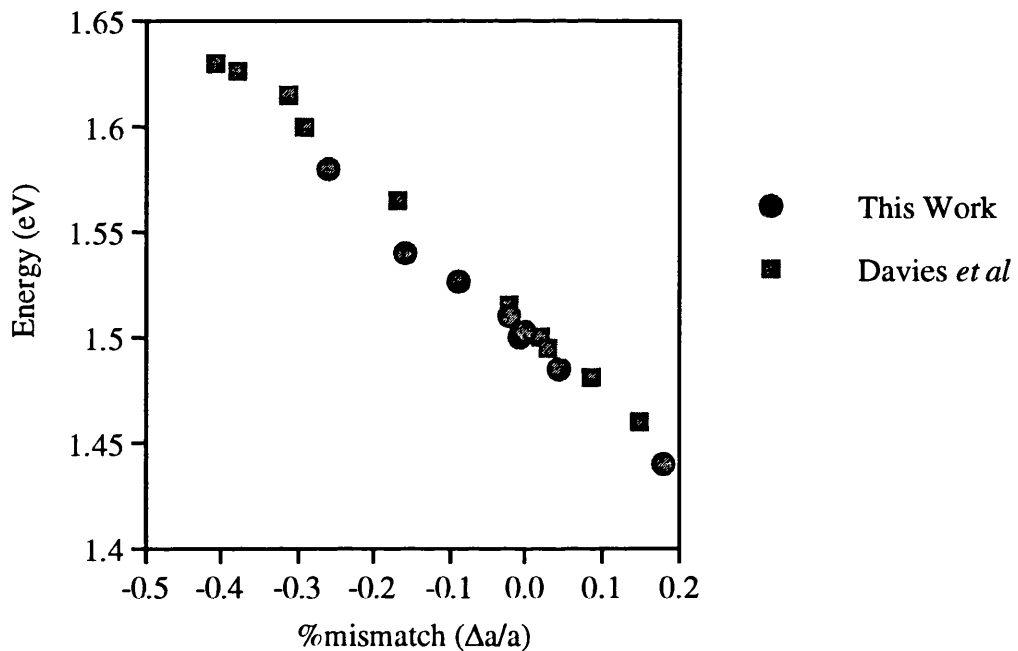
Figure 5.13. Energy of PL peak as a function of mismatch derived from DCXD rocking curves for AlInAs on InP.

No secondary peaks were observed in all but one of the InAlAs PL spectra. This cannot however be taken as an indication of the absence of any significant segregation layer since the InAlAs samples were routinely capped with a 100Å thick $In_{0.53}Ga_{0.47}As$ layer which may have prevented the observation by PL of any segregation layer which had been formed. The exception to this was a sample grown under 'self-locking' conditions ie the incident indium flux was higher than that necessary to compensate for indium desorption in the absence of strain. The PL spectrum for this sample is shown in Figure 5.14. Two distinct peaks are present,

the weaker of which is produced by bulk AlInAs luminescence. The mismatch calculated from Figure 5.13 using the peak energy of 1.45eV is 0.1%. This value corresponds very well with the DCXD measurement which also gives a mismatch of 0.1%. The peak appears to contain some structure and there is evidence of more than one transition involved. The linewidth is 14meV which is significantly smaller than was obtained for growth at lower temperatures.
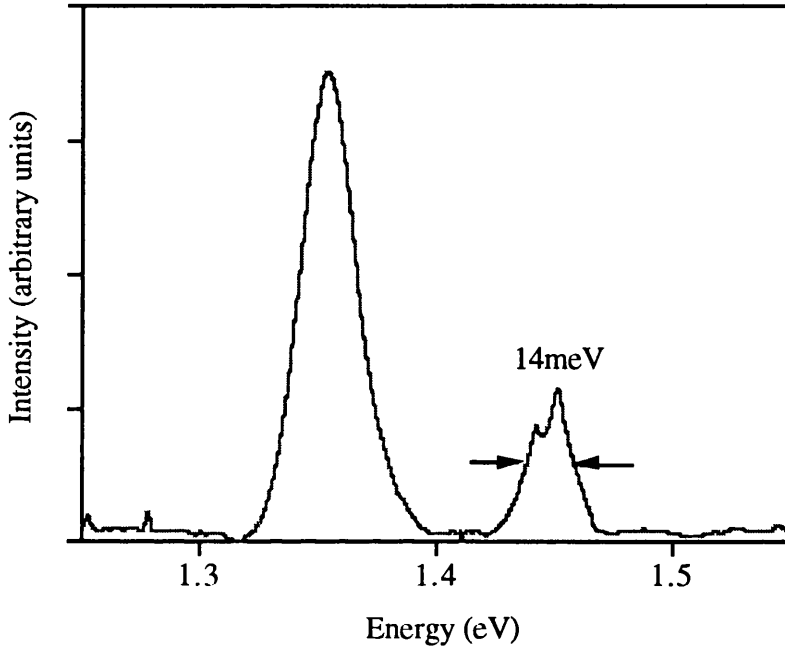
Figure 5.14. PL spectrum for AlInAs sample grown at 620°C.

The larger of the two peaks does not resemble anything previously seen in the literature. It is thought that this produced by the presence of a segregation layer. The structure of the sample is shown schematically in Figure 5.15. A 0.1μm low temperature InAlAs layer was first grown at $T_S = 525°C$. This was capped with a 3 ML thick GaAs layer, the purpose of which was to prevent decomposition of the surface during the growth interrupt used to raise the substrate temperature to 620°C. 2μm of InAlAs was then grown at this elevated temperature followed by another GaAs layer to protect the surface during the lowering of the substrate temperature to 525°C prior to growth of an $In_{0.53}Ga_{0.47}As$ cap. It is suggested that the upper of the 2 GaAs layers provides confinement for an InAs segregation layer which forms a well between the GaAs and the high temperature InAlAs. The energy of the secondary peak (1.35eV) corresponds to a well thickness of $\approx7.5Å$, if the assumption of a square InAs well is again made.
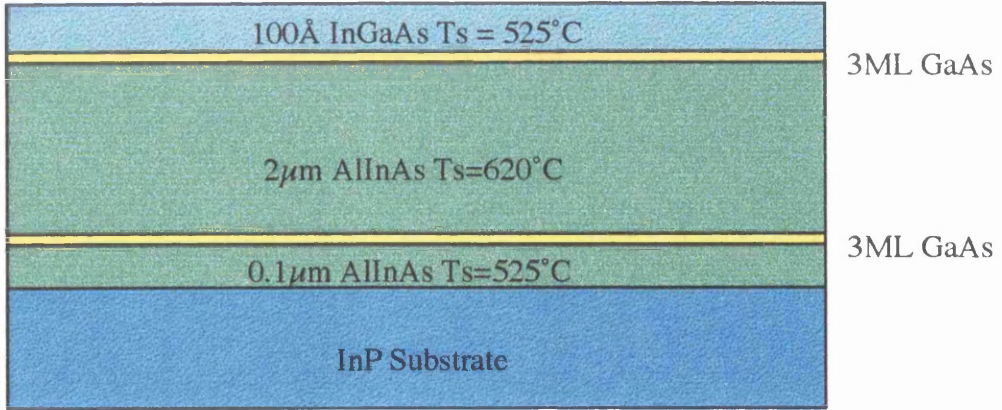
Figure 5.15. Schematic of structure of InAlAs sample grown at 620°C.

5.2 Electrical Properties

5.2.1 Introduction

The Hall measurement[19,20,21] is the most widely used test of the electrical quality of semiconductor materials. It can be used to distinguish whether a semiconductor is n- or p-type and to measure the majority carrier concentration and mobility. The Hall effect is a consequence of the Lorentz force which acts on charges moving in magnetic fields. The Lorentz force on a particle having a charge q and moving in a magnetic field B is given by :-

$$F = qv \times B \tag{5.1}$$

where the cross product is taken between v and B so that the Lorentz force vector is perpendicular to both the velocity and the magnetic field.

A schematic representation of a Hall experiment on an n-type semiconductor is given in Figure 5.16. The measurement current I is in the x-direction and the magnetic field is applied in the z-direction. The Lorentz force produces a sideways deflection of electrons in the y-direction causing an accumulation of electrons on one side of the test structure. This gives rise to an electric field E_H called the *Hall field*, which acts to counterbalance the Lorentz force and produces a terminal voltage V_H, called the *Hall voltage*. Since E_H balances the Lorenz force, its value becomes :-

$$E_H = \frac{JB}{-nq} = R_H JB \qquad \text{where } R_H = -\frac{1}{nq} \tag{5.2}$$

Thus the Hall field is proportional to the product of the current density and the magnetic field. The proportionality constant R_H is known as the *Hall coefficient*. Measurement of the V_H for a known test current and magnetic field can therefore be used to obtain the electron concentration of the sample since :-

$$n = -\frac{1}{qR_H} = \frac{JB}{qE} = \frac{IB}{qtV_H} \qquad (5.3)$$

where t is the electrical thickness of the sample material.

If a measurement of the voltage V in the direction of the test current is made then the sample resistivity ρ can be calculated since :-

$$\rho = \frac{V/I}{L/Wt} \qquad (5.4)$$

where L is the distance between the voltage probes and w is the width of the test sample. The mobility can then be calculated simply from the ratio of the Hall coefficient and the resistivity :-

$$\mu = \frac{1}{nq\rho} = -\frac{R_H}{\rho} \qquad (5.5)$$

Although this discussion has been related to n-type material, similar results can be obtained for p-type material, with the exception that the Hall voltage and Hall coefficient are negative. The Hall effect can thus be used to give the carrier type, and accurate values for both the carrier concentration and mobility of semiconductor materials.
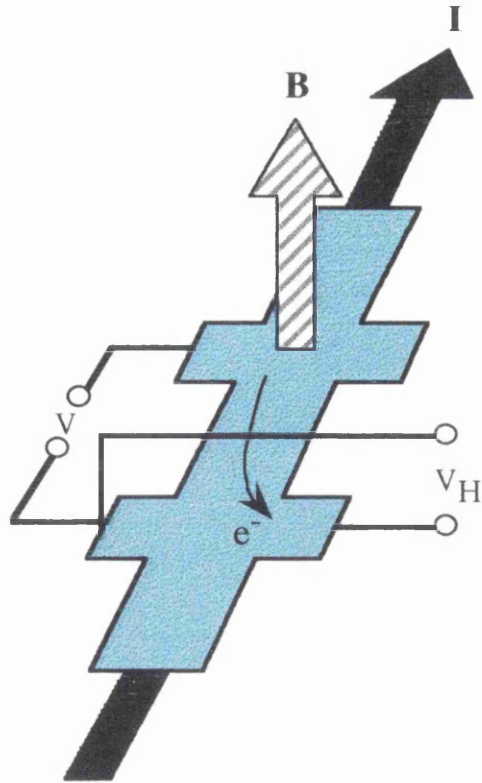
Figure 5.16. Schematic representation of a Hall experiment. Electrons (e⁻) are deflected by the Lorenz force until a counterbalancing voltage (V_H) is established.

5.2.2 Experimental

Hall mobilities and electron concentration characteristics were measured by the conventional van der Pauw[22] method at 300K and 77K. The van der Pauw four-contact technique is normally used for epitaxial films since it has the advantage of keeping the current lines away from the Hall contacts. A schematic diagram of the test structure used is given in Figure 5.17. The 'clover leaf' shape was defined by powder etching. The samples were then deoxidised in HCl:H_2O 1:1 and ohmic contacts were formed by annealing indium beads into the surface at ≈420°C. The test current was passed through diametrically opposite pairs of contacts and V_H was measured across the remaining contact pair. The resistivity was found by passing the current through an adjacent pair of contacts and measuring the voltage across the other adjacent pair. Measurement inaccuracies were minimised by taking appropriate averages of all possible contact combinations and by reversing the magnetic field. Depletion layer thicknesses at the surface and interface were calculated assuming a surface potential of 0.27eV.
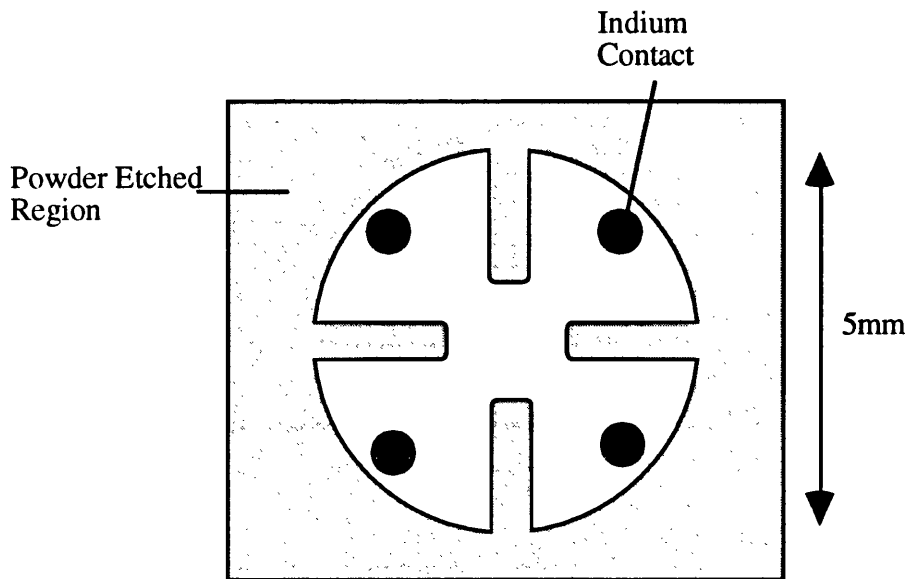
Figure 5.17. Schematic diagram of the test structure used to perform Hall measurements.

5.2.3 $In_{0.53}Ga_{0.47}As$ Hall Mobility Results

The measured $In_{0.53}Ga_{0.47}As$ mobilities as a function of carrier density at 300K and 77K are shown in Figures 5.16 and 5.17 respectively. The 300K residual free carrier concentration was typically around $1 \times 10^{15}cm^{-3}$ with a mobility of around $8500cm^2V^{-1}s^{-1}$. Typical 77K values were $7 \times 10^{14}cm^{-3}$ and $20000cm^2V^{-1}s^{-1}$. The highest measured mobility was $8696cm^2V^{-1}s^{-1}$ at 300K and $47794cm^2V^{-1}s^{-1}$ at 77K. These mobility values are significantly lower than the best reported values of $15200cm^2V^{-1}s^{-1}$ at 300K and $104000cm^2V^{-1}s^{-1}$ at 77K[23].

No relationship between mobility and substrate temperature or As_2 flux has been found. The measured mobility figures appear, in general, to be uncorrelated with the growth conditions used. It is also apparent from Figures 5.16 and 5.17 that the carrier density has little effect on the measured mobility, and there is considerable disagreement between the actual results and theoretical values given by Takeda[24].

108
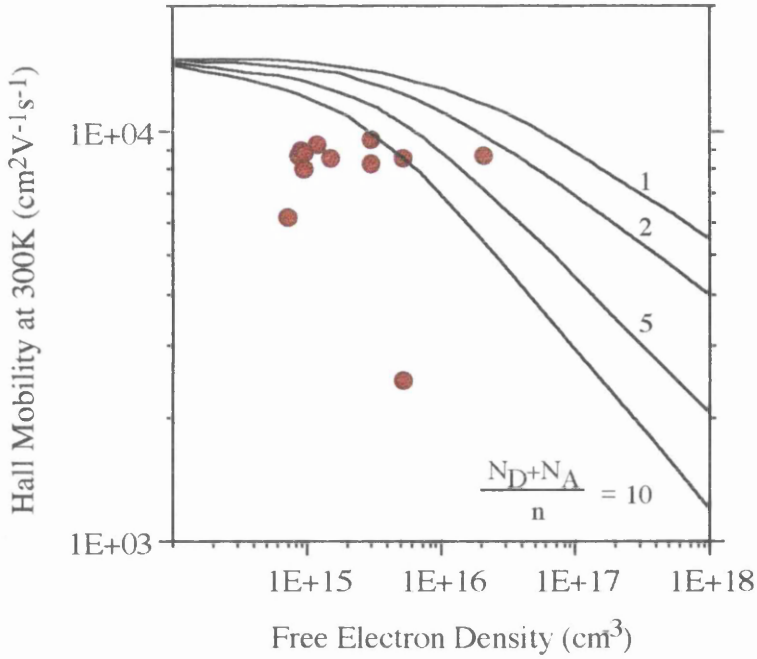
Figure 5.18. Hall mobility at 300K vs carrier density of nominally undoped $In_{0.53}Ga_{0.47}As$ samples. The solid lines represent theoretical predictions by Takeda (Reference 24).
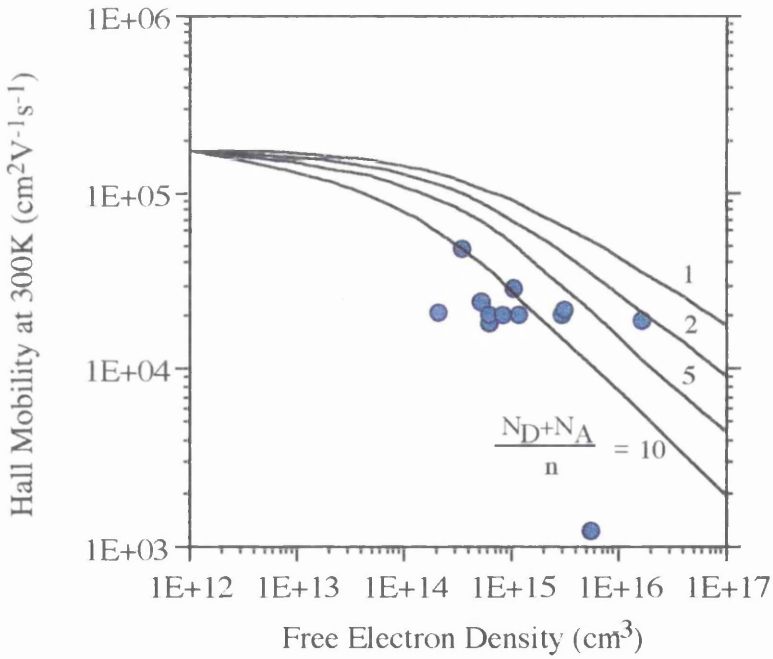
Figure 5.19. Hall mobility at 77K vs carrier density of nominally undoped $In_{0.53}Ga_{0.47}As$ samples. The solid lines represent theoretical predictions by Takeda (Reference 24).

The discrepancy is probably due to parallel conduction at the sample surface, or the substrate/layer interface, or both. Several authors have pointed out

the existence of such effects in hetero-epitaxial films. It has, for example, been reported that films of InSb on GaAs change from n-type to p-type as the interface is approached and a two-dimensional electron gas (2DEG) has also been observed at such an interface[25]. Parallel conduction has also been measured in InAs epilayers grown on GaAs[26] although it is not clear whether this is caused by the substrate/layer interface or the high concentration of surface states which is known to exist on InAs films. It will be shown in chapter 6 that a sheet charge density as high as $4 \times 10^{11} cm^{-2}$ is present at nominally undoped $In_{0.53}Ga_{0.47}As/In_{0.52}Al_{0.48}As$ interfaces and it is therefore reasonable to expect a similar effect at an $InP/In_{0.53}Ga_{0.47}As$ interface. The existence of InAs segregation layers, demonstrated in this chapter may also contribute to parallel conduction.

This explanation for the low $In_{0.53}Ga_{0.47}As$ mobilities obtained is supported by Hall measurements performed on two consecutive $In_{0.53}Ga_{0.47}As$ samples grown under exactly the same growth conditions but with different thicknesses. The Hall results for these samples, one $2\mu m$ and the other $5\mu m$ thick, are given in Table 5.1.

Sample Thickness (μm)	μ (300K) ($cm^{-2}v^{-1}s^{-1}$)	n (300K) (cm^{-3})	μ (77K) ($cm^{-2}v^{-1}s^{-1}$)	n (77K) (cm^{-3})
2	8612	5.2×10^{15}	21768	3.2×10^{15}
5	9430	1.9×10^{15}	28389	1.0×10^{15}

Table 5.1. Measured mobilities and carrier concentrations for two consecutive $In_{0.53}Ga_{0.47}As$ epilayers.

The rise in measured mobility and drop in measured carrier concentration for the thicker of the two samples is consistent with parallel conduction.

5.2.4 $In_{0.52}Al_{0.48}As$ Hall Mobility Results

It was not found possible to perform mobility measurements on $In_{0.52}Al_{0.48}As$ samples grown under standard growth conditions. This was not unexpected since it has been found impossible to obtain mobility measurements from undoped AlGaAs grown in the same reactor. The presence of Al in the alloy increases the incorporation of impurities in the layer, which act as traps and suppress carrier transport. This occurs in AlGaAs layers even at substrate

temperatures of $\approx 630^\circ$C so such problems were expected in $In_{0.52}Al_{0.48}As$ layers which are grown at $\approx 530^\circ$C.

Mobility measurements were, however, successfully made on the sample grown at 620°C in the 'self-locking' regime. The measured mobility and carrier density values for this sample were $948cm^2V^{-1}s^{-1}$ and $2.9 \times 10^{15}cm^{-3}$ at 300K. These values are comparable with the best reported values in the literature.

5.3 References

1   E.C. Lightowlers in 'Growth and Characterisation of Semiconductors'
    Edited by R.A. Stradling and P.C. Klipstein
    (Hilger, Bristol, 1990)

2   'Characterisation of Epitaxial Semiconductor Films'
    Edited by H. Kressel
    (Amsterdam, Oxford, 1976)

3   'Technology and Physics of Molecular Beam Epitaxy'
    Edited by E.H.C. Parker
    New York, London, 1985)

4   'The Behavior of Unintentional Impurities $In_{0.53}Ga_{0.47}As$ Grown by MBE'
    A.S. Brown, S.C. Palmateer, G.W. Wicks, and L.F. Eastman
    Journal Of Electronic Materials 1985 Vol.14 No.3 pp 367-378

5   'Optical-Properties of High-Quality InAlAs/InGaAs SQWs Grown by MBE
    Using Specially Refined In and Al Sources'
    T. Mishima, J. Kasai, Y. Uchida, and S. Takahashi
    Journal Of Crystal Growth 1989 Vol.95 No.14 pp.338-342

6   'Electrical and Structural Characterization of Highly Perfect Semi-Insulating
    InAlAs Grown By Molecular-Beam Epitaxy'
    A.T. Macrander, S.J. Hseih, F. Ren and J.S. Patel
    Journal Of Crystal Growth 1988 Vol.92 No.12 pp.83-87

7   'Photoluminescence and Double-Crystal X-Ray Study of InGaAs/InP -Effect
    Of Mismatch Strain on Band-Gap'
    I. C. Bassignana, C. J. Miner, and N. Puetz
    Journal Of Applied Physics 1989 Vol.65 No.11 pp.4299-4305

8   'Optical-Quality GaInAs Grown by Molecular-Beam Epitaxy'
    G. Wicks, C.E.C. Wood, H. Ohno, L.F. Eastman
    Journal Of Electronic Materials 1982 Vol.11 No.2 pp.435-440

9   'Observation of Photoluminescence From InAs Surface Quantum Wells Grown
    on InP(100) by Molecular Beam Epitaxy'
    Z. Sobiesierski, S.A. Clark, R.H. Williams, A. Tabata, T. Benyattou,
    G. Guillot, M. Gendry, G. Hollinger, and P. Viktorovitch
    Applied Physics Letters 1991 Vol.58 No.17 pp1863-1865

10 'Epitaxial Regrowth of an InAs Surface on InP - an Example of Artificial
    Surfaces'
    J.M. Moison, M. Bensoussan and F. Houzay
    Physical Review B-Condensed Matter 1986 Vol.34 No.3 pp.2018-2021

11 'Structural and Chemical-Properties of InAs Layers Grown on InP(100)
    Surfaces by Arsenic Stabilization'
    G. Hollinger, D. Gallet, M. Gendry, C. Santinelli and P. Viktorovitch
    Journal of Vacuum Science & Technology B-Microelectronics Processing and
    Phenomena 1990 Vol.8 No.4 pp.832-837

12 'Chemical Etching Characteristics of InGaAs/InP and InAlAs/InP
    Heterostructures'
    A. Stano
    Journal Of The Electrochemical Society 1987 Vol.134 No.2 pp.448-452

13 'Surface Segregation of Third-Column Atoms in Group III-V Arsenide
    Compounds: Ternary Alloys and Heterostructures'
    J. M. Moison, C. Guile, F. Houzay, F. Barthe, and M. Van Rompay
    Physical Reveiw B 1989 Vol.40 No.9 pp6149-6161

14 'Surface Segregation in III-V Alloys'

J.M. Moison, F. Houzay, F. Barthe, J.M. Gérard, B. Jusserand, J. Massies and F.S. Turco-Sandroff

Journal of Crystal Growth 1991 Vol. 111 No. 22 pp141-150

15 'In Situ probing at the growth temperature of the surface composition of (InGa)As and (InAl)As'

J. Gerard

Applied Physics Letters 1992 Vol.61 No.17 pp2096-2098

16 'Experimental-Evidence Of Difference In Surface And Bulk Compositions Of $Al_xGa_{1-x}As$, $In_xAl_{1-x}As$ And $In_xGa_{1-x}As$ Epitaxial Layers Grown By Molecular-Beam Epitaxy'

J. Massies, F. Turco, A. Saletes and J.P. Contour

Journal Of Crystal Growth 1987 Vol.80 No.2 pp.307-314

17 'Growth of InGaAs and InAlAs for Laser Diodes'

R. Sivertsen, K. Øvsthus, D. Wang, P.I. Jensen, S.I. Hansen, K. Pettersen, A. Sudbø, L. Hafskjær and K. Gjønnes

Presentation to the 7th European Workshop on MBE

Bardonecchia, Italy 1993

18 'The Growth and Characterization of Nominally Undoped $In_xAl_{1-x}As$ Grown by Molecular-Beam Epitaxy'

G.J. Davies, T. Kerr, C.G. Tuppen, B. Wakefield, D.A. Andrews

Journal Of Vacuum Science & Technology B-Microelectronics Processing And Phenomena 1984 Vol.2 No.2 pp.219-223

19 H. Weiss in 'Semiconductors and Semimetals' Vol.4

Edited by R.K. Willardson and A.C. Beer

(New York, London Academic Press, 1966)

20 R.A. Stradling in 'Growth and Characterisation of Semiconductors'

Edited by R.A. Stradling and P.C. Klipstein

(Hilger, Bristol, 1990)

21 'Semiconductor Devices : Physics and Technology'
    S. M. Sze
    (New York, Chichester, 1985)

22 L. van der Pauw
    Philips Research Reports 1958 Vol.13 No.1

23 'Very High Purity $In_{0.53}Ga_{0.47}As$ Grown by Molecular Beam Epitaxy'
    T. Mishima, M. Takahama, Y. Uchida, T. Tanoue and S. Takahashi
    Journal of Electronic Materials 1991 Vol.20 No.1 pp113-116

24 'Low-field Transport Calculations'
    Y. Takeda
    Chapter 9 of 'GaInAsP Semiconductors'
    edited by T.P. Pearsall, pp 213-241 1982

25 'Insitu Contacts to GaAs Based on InAs'
    S.L. Wright, R.F. Marks, S. Tiwari, T.N. Jackson, H. Baratte
    Applied Physics Letters 1986 Vol.49 No.22 pp.1545-1547

26 'Magneto-optical and Transport Studies of Ultrahigh Mobility Films of InAs
    Grown on GaAs by Molecular Beam Epitaxy'
     S. Holmes, R.A. Stradling, P.D. Wang, R. Droopad, S.D. Parker,
    R.L. Williams
    Semiconductor Science and Technology 1989 Vol.4 No.4 pp303-308

Chapter 6

Photoluminescence Properties of $In_{0.53}Ga_{0.47}As/In_{0.52}Al_{0.48}As$ Quantum Wells

6.1 Introduction

$In_{0.53}Ga_{0.47}As/In_{0.52}Al_{0.48}As$ quantum wells have important applications, in particular for devices operating at wavelengths from 1.65μm to 1.0μm which span the 1.3μm minimum dispersion and 1.55μm minimum loss windows of silica fibres.

Structural disorder and chemical impurities at the interfaces of quantum wells have a strong influence on the optical properties of the wells[1] and can limit the performance of devices based on such structures[2]. It has been shown that variations in well thickness (L_z) can cause a broadening of the luminescence and a reduction in the efficiency of the wells. The growth conditions used for the production of quantum well optical devices should therefore be tailored to minimise the influence of interface effects on the device operation. A frequently used technique to obtain smooth interfaces is the addition of a growth interrupt[3,4] to increase the size of the island-like structures[5] formed during MBE growth and hence improve the flatness of the interface. The advantage of increased interface smoothing using growth interrupts is, however, mitigated by enhanced trap and impurity incorporation. It would be preferable to obtain comparable interface quality by manipulating the growth parameters and hence avoiding the need to interrupt growth. This chapter discusses the influence of growth conditions on the quality of $In_{0.53}Ga_{0.47}As/In_{0.52}Al_{0.48}As$ interfaces.

6.2 Experimental Procedures and Growth Conditions

All quoted wafer temperatures were measured with an Ircon series V optical pyrometer. Growth was performed on epi-ready semi-insulating (100)-InP substrates. Quarter wafer samples were indium mounted onto silicon wafers and then loaded into standard indium-free wafer holders.

The quantum well samples were grown using dimeric arsenic. The samples typically contained 4 or 5 $In_{0.53}Ga_{0.47}As$ single quantum wells separated by 200Å thick $In_{0.52}Al_{0.48}As$ barriers. The quantum well thicknesses used varied between 15 and 120Å. The sample was capped with 100Å of $In_{0.53}Ga_{0.47}As$ to prevent oxidation of the $In_{0.52}Al_{0.48}As$. A typical structure is shown in Figure 6.1.
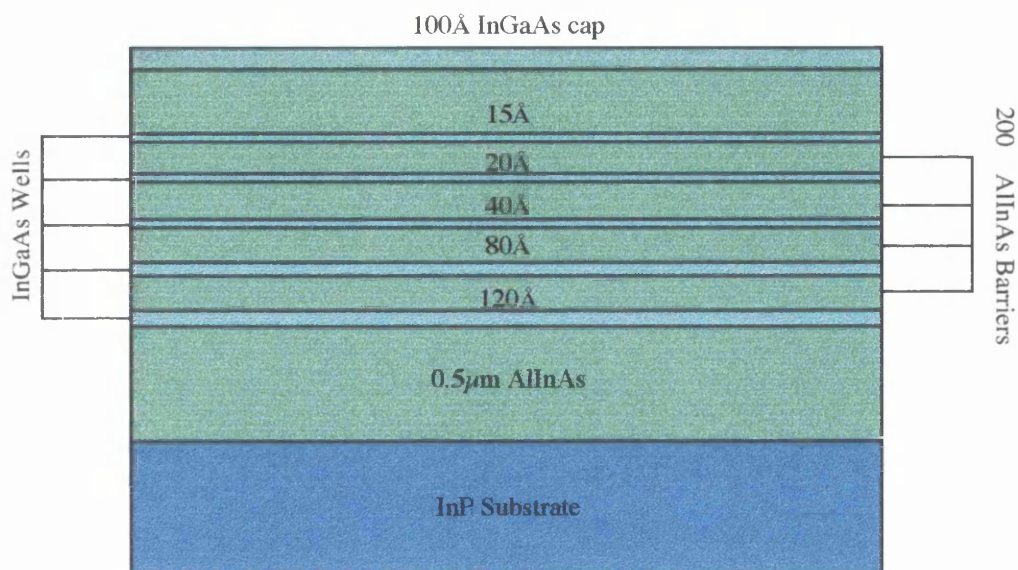
Figure 6.1. Schematic diagram (not to scale) of the structure of one of the single quantum well structures grown.

6.3 Calibration of Incident Flux Densities

Calibration for the growth of $In_{0.53}Ga_{0.47}As/In_{0.52}Al_{0.48}As$ quantum wells is normally carried out using test structures which are examined by TEM[6], SEM[7] or PL[1] to accurately determine the $In_{0.53}Ga_{0.47}As$ growth rate. The $In_{0.53}Ga_{0.47}As$ and $In_{0.52}Al_{0.48}As$ growth rates and compositions for this study were, in contrast, calibrated by RHEED intensity oscillations using the method previously described in Chapter 4. Before the commencement of growth, the growth rate of $In_{0.53}Ga_{0.47}As$ was calibrated to a value of 1.00μm/hr and the $In_{0.52}Al_{0.48}As$ to a value of 1.023μm/hr. The desired well and barrier thicknesses were obtained by controlling the timing of the shutter operations based on these growth rates. It should be noted that no attempt was made to restrict the thickness of the wells to an integral number of monolayers: the target well thicknesses were arbitrarily chosen to provide a spread of well confinement energies. Substrate temperatures were kept constant throughout the growth of the structures and the

arsenic flux was, unless otherwise stated, kept close to the minimum value for growth of $In_{0.53}Ga_{0.47}As$ without indium droplet formation on the surface. The method for determining the minimum flux necessary for each substrate temperature is as described in Chapter 4. A summary of the growth conditions for four samples used in this study is given in Table 6.1.

Sample No.	Well Widths (Å)	Growth Temperature	As$_2$ Flux
#B290	120, 80, 40, 20	515°C	minimum
#B291	120, 80, 40, 20	525°C	minimum
#B227	120, 80, 40, 20	525°C	2 x minimum
#B303	80, 60, 40, 20, 15	535°C	minimum

Table 6.1. Well widths, substrate temperatures and arsenic flux densities for the four samples used in this study.

6.4 Substrate Temperature Dependence

Three samples were grown with substrate temperatures of 515°C, 525°C and 535°C with the arsenic flux in each case set to the minimum value consistent with good morphology. Sample #B290 was grown at 515°C, which was the lowest of the three growth temperatures used.
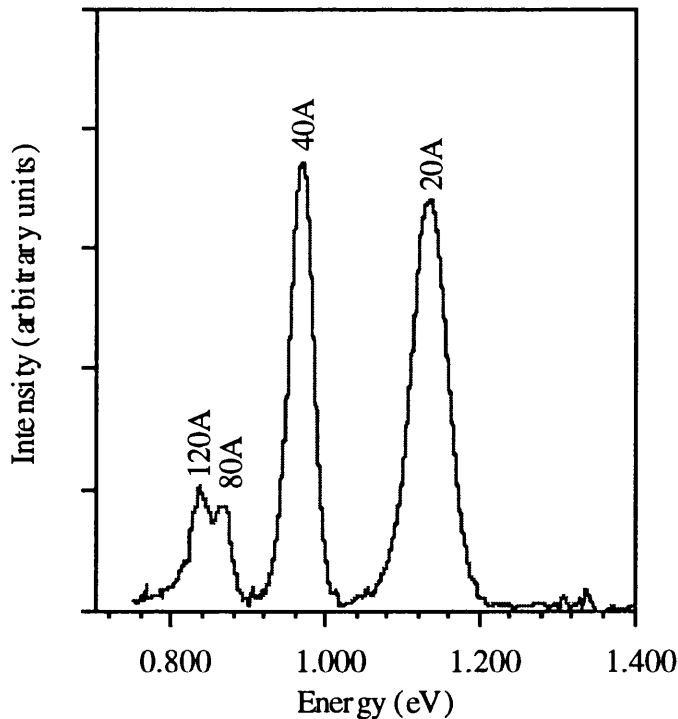
Figure 6.2. 9K PL spectrum for sample #B290.

The photoluminescence (PL) spectrum obtained for this sample is given in Figure 6.2. The spectrum of sample #B290 shows the presence of all of the wells, however the linewidths and the luminescence intensities are poor in comparison to those found in the literature. The linewidths of the peaks in the spectrum of #B290 are shown as a function of well width in Figure 6.3.
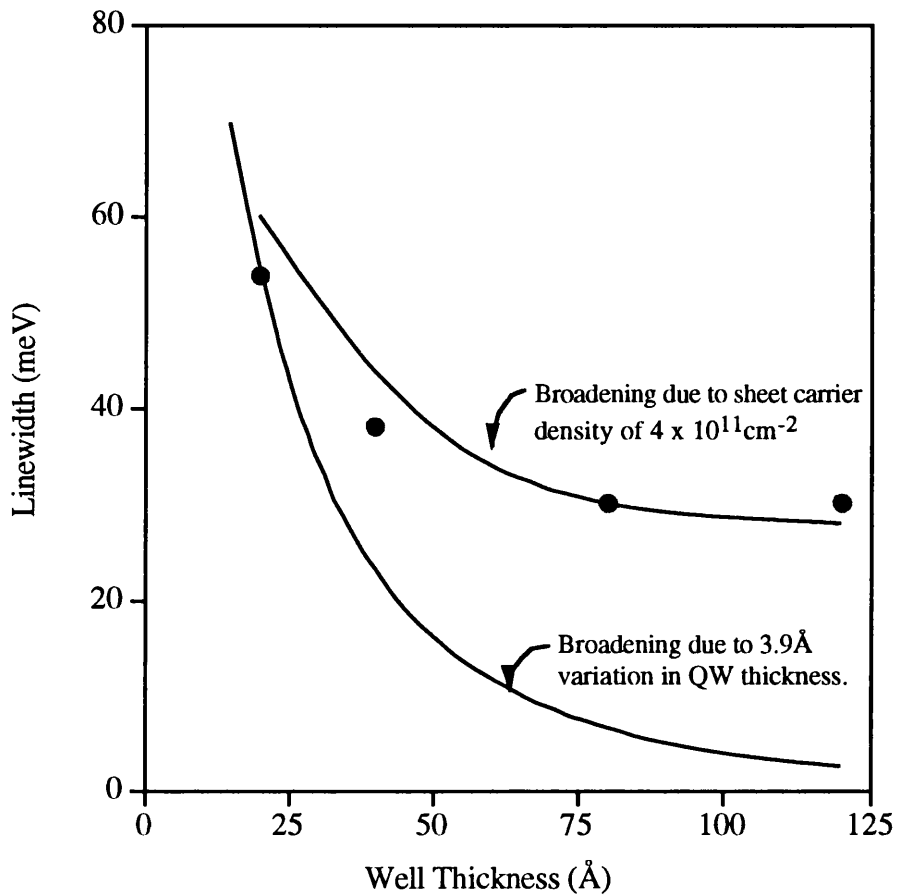
Figure 6.3. Linewidth as a function of well width for sample #B290 (which was grown with minimum arsenic flux at a substrate temperature of 515°C).

Welch *et al* [8] have shown that the dominant broadening mechanisms of the photoluminescence linewidth of $In_{0.53}Ga_{0.47}As/In_{0.52}Al_{0.48}As$ quantum wells are :-

    (a) Variations in the well thickness.

    (b) Band filling due to high carrier concentrations within the quantum well produced by unintentional donors in the $In_{0.52}Al_{0.48}As$.

    (c) Structural defects at the interface.

Thickness variations of lateral extent less than the in-plane Bohr radius of the exciton cause broadening of PL linewidths which can be calculated from[9,10] :-

$$\Delta E = \frac{dE}{dL_z} \Delta L_z \qquad (6.1)$$

The change in emission energy as a function of well width is larger for thin wells than thick wells, so the value of ΔE increases as the well width decreases for a constant variation in well thickness. The experimental results for #B290 give a linewidth of 54meV for the 20Å well, corresponding to a variation of 3.9Å if entirely due to thickness variations. The theoretical curve for a thickness variation of 3.9Å is shown in Figure 6.3. For wells larger than 20Å, the linewidths obtained experimentally are markedly larger than those predicted by the curve, suggesting that the dominant broadening method is unlikely to be changes in well thickness.

PL linewidths of $In_{0.53}Ga_{0.47}As/In_{0.52}Al_{0.48}As$ quantum well structures can also be broadened by the transfer of electrons produced by deep donors in the $In_{0.52}Al_{0.48}As$, which have an ionisation energy less than the conduction band discontinuity at the $In_{0.53}Ga_{0.47}As/In_{0.52}Al_{0.48}As$ interface, from the $In_{0.52}Al_{0.48}As$ into the $In_{0.53}Ga_{0.47}As$ wells. The extra carriers fill up the available states so that the Fermi level is well above the conduction band minimum of the $In_{0.53}Ga_{0.47}As$. This band-filling allows electrons from a range of energies in the conduction band to recombine, producing a broadening of the linewidth.

The energy spread in the PL spectrum (ΔE) produced by this effect is given by[11] :-

$$\Delta E = \frac{n_s \pi^2 \hbar^3}{L_z m_e^* \sqrt{\left(2m_e^* E_e\right)}} \qquad (6.2)$$

where n_s is the sheet carrier concentration at the interface, m_e^* is the electron effective mass, E_e is the energy of the electron relative to the conduction band edge, and L_z is the well thickness.

People et al [12] have measured a sheet charge density of $4 \times 10^{11}cm^{-2}$ at the $In_{0.53}Ga_{0.47}As/In_{0.52}Al_{0.48}As$ interface. Griem et al [13] have measured a similar value for the minimum possible sheet carrier density of $In_{0.53}Ga_{0.47}As/In_{0.52}Al_{0.48}As$ HEMT structures. A slightly smaller value of $2 \times 10^{11}cm^{-2}$ was measured by Welch et al for a SQW structure. The theoretically calculated variation in linewidth caused by a sheet carrier concentration of

$4 \times 10^{11} \text{cm}^{-2}$ is shown as a function of well width in Figure 6.3 and the theoretical line is in reasonably good agreement with the experimental data.

Samples #B291 and #B303 were grown at substrate temperatures of 525°C and 535°C respectively. The luminescence intensity of the samples was found to increase significantly as the growth temperature was increased as shown in Figure 6.4. The maximum intensity for sample #B303, grown at 535°C, was an order of magnitude larger than that measured for #B290 grown at 515°C.
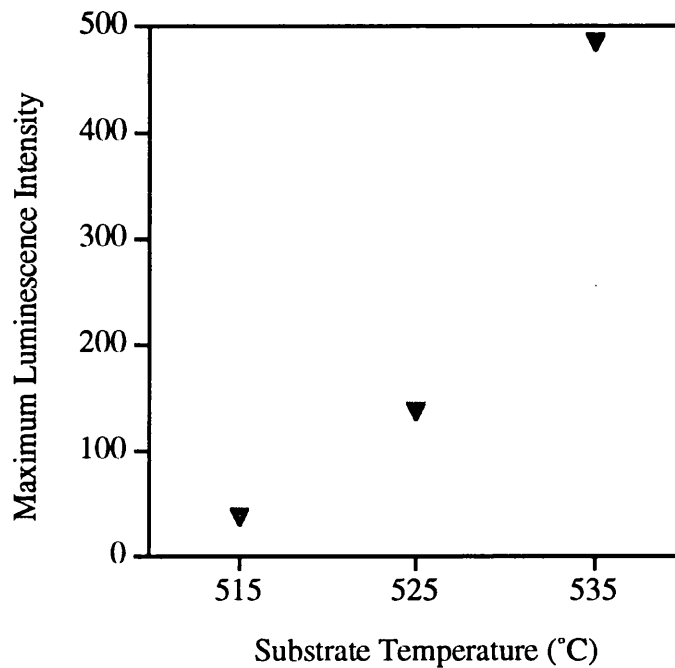
Figure 6.4. Maximum luminescence intensity as a function of growth temperature.

Figure 6.5 shows the PL spectra for #B290, #B291 and #B303. The vertical scale on this figure has been kept constant to allow comparison of the luminescence intensity between samples. There is a very clear improvement in the linewidths and intensities of the well luminescence as the substrate temperature is increased above 515°C.
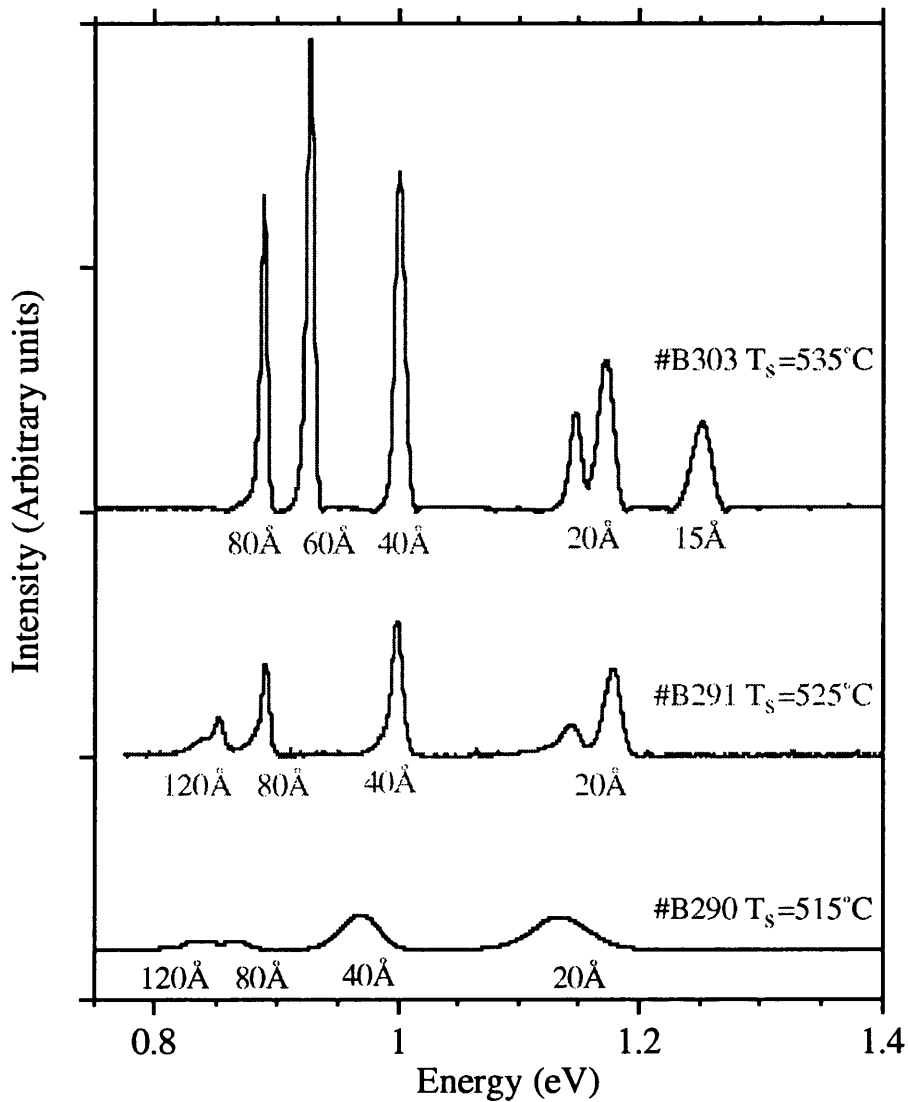
Figure 6.5. PL spectra for #B290, #B291 and #B303. The same vertical scale has been used in each case.

The linewidth as a function of well width for sample #B291 and #B303 is shown in Figure 6.6. Linewidth broadening due to a sheet charge density of $1 \times 10^{11} cm^{-2}$ gives a reasonable fit to the experimental data. This is much lower than the value of $4 \times 10^{11} cm^{-2}$ obtained for #B290, and it agrees well with Hall measurements made at nominally undoped $In_{0.53}Ga_{0.47}As/In_{0.52}Al_{0.48}As$ interfaces for material grown at a substrate temperature of 535°C.
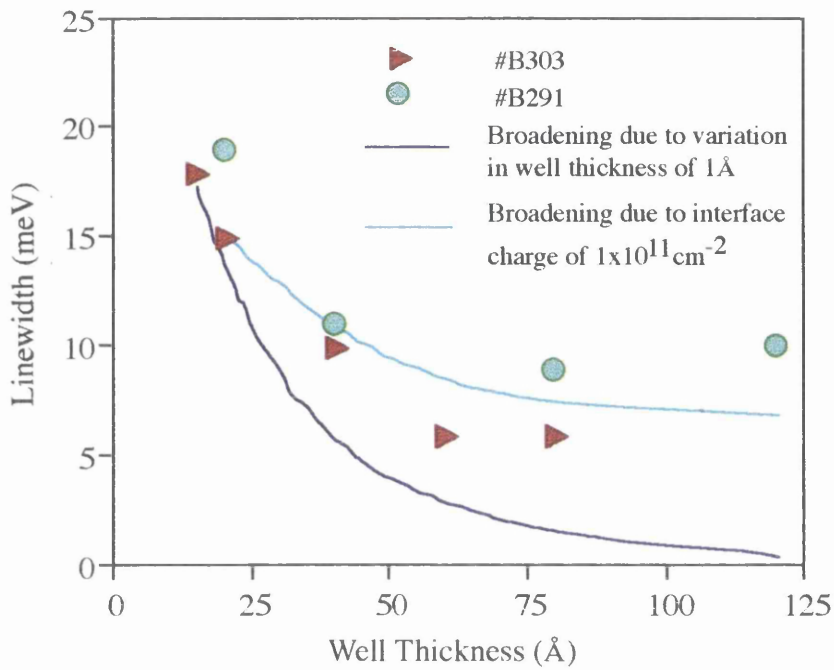
Figure 6.6. Linewidth as a function of well width for samples B291 and B303, which were grown with minimum arsenic flux at substrate temperatures of 525°C and 535°C respectively.

The luminescence of the 20Å wells from samples #B291 and #B293 clearly shows two distinct peaks. The peak associated with the 20Å well of sample #B293 is shown in Figure 6.7.

Theoretical calculations show that the energy of the main peak corresponds to a well thickness of 20.7Å and that the spacing between this peak and the second smaller peak corresponds to a thickness difference of exactly one monolayer. This suggests that the peak splitting is due to small variations in the well thickness. Broadly speaking, such variations fall into two categories :-

(a) Microroughness which occurs on an atomic scale much smaller than the free-exciton Bohr radius.

(b) extended monolayer flat islands which are larger than the free-exciton Bohr radius.
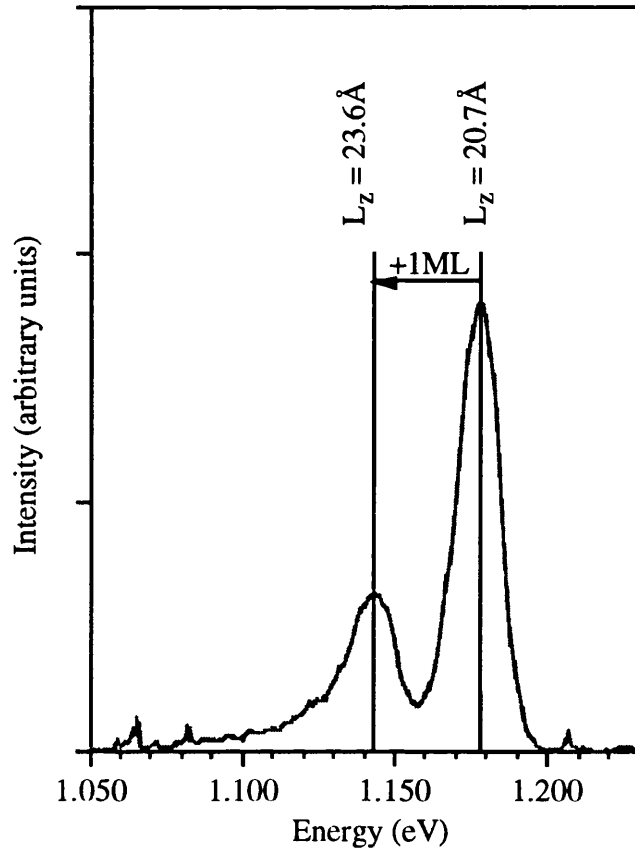
Figure 6.7. Photoluminescence spectrum for the nominally 20Å well of sample #B291. The main peak in fact corresponds to a well thickness of 20.7Å. The secondary peak corresponds to a well thickness of 23.6Å - exactly one monolayer wider than the main peak

A recombining exciton is relatively insensitive to microroughness and emits a photon with an energy corresponding to the width of the quantum well averaged over several exciton diameters[14]. This averaging effect means that the energy of the emitted photon is not constrained to a value produced by a well width corresponding to an integral number of monolayers. For the case of extended monolayer flat islands, an exciton can be considered as being confined to an area of discrete quantum well thickness. This can result in 'monolayer splitting' in the luminescence spectrum. Figure 6.8 shows schematically the effects of monolayer thickness vibrations on the photoluminescence spectra. The spectra of sample #B293 and #B303 have two peaks associated with the well nominally 20Å thick, indicating that the monolayer flat islands are restricted to only one of the interfaces. This is most likely to be the upper of the two interfaces, where there is a transition from the growth of $In_{0.53}Ga_{0.47}As$ to the growth of $In_{0.52}Al_{0.48}As$.
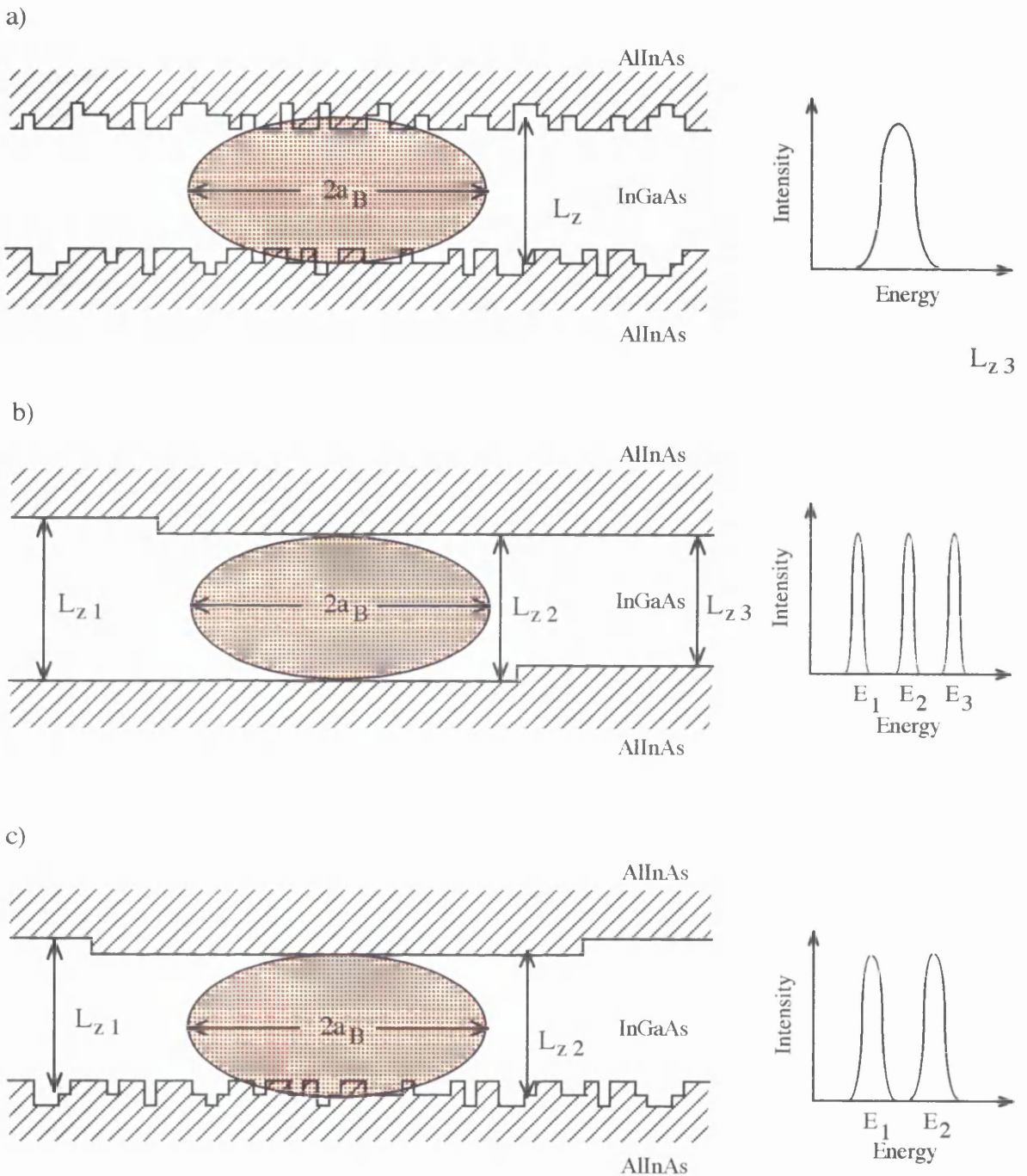
Figure 6.8 - Effect of interface disorder on the PL spectrum of single quantum wells.

 a) Microroughness at both interfaces produces a single broad peak since the scale of the interface roughness is much smaller than the Bohr radius of the exciton. The linwidth is increased by thickness variations within the area of the exciton.

b) Extended monolayer flat islands at both interfaces produces 3 discrete peaks associated with well thickness differences of ± 1 monolayer. The size of individual islands is greater than the lateral dimensions of the exciton. This results in very narrow linewidths.

c) A combination of microroughness and extended monolayer flat islands produces 2 discrete peaks with linewidths intermediate between those of examples a) and b)

The relatively low surface mobility of Al adatoms on the growth surface means that the growth of $In_{0.52}Al_{0.48}As$ is likely to become distributed over several monolayers producing a rough interface at the first well interface. This effect has been seen in the GaAs/AlGaAs system[15] where the first interface, switching from the growth of AlGaAs to GaAs has been shown to be much poorer than the second, GaAs to AlGaAs, interface.

The lateral size of the exciton in a quantum well varies as the inverse of the exciton binding energy E_X[16]. Calculations by Thoai $et\ al$ [17] have shown that the exciton binding energy in $In_{0.53}Ga_{0.47}As/In_{0.52}Al_{0.48}As$ quantum wells goes through a maximum at a well thickness of ≈ 10Å as shown in Figure 6.9.
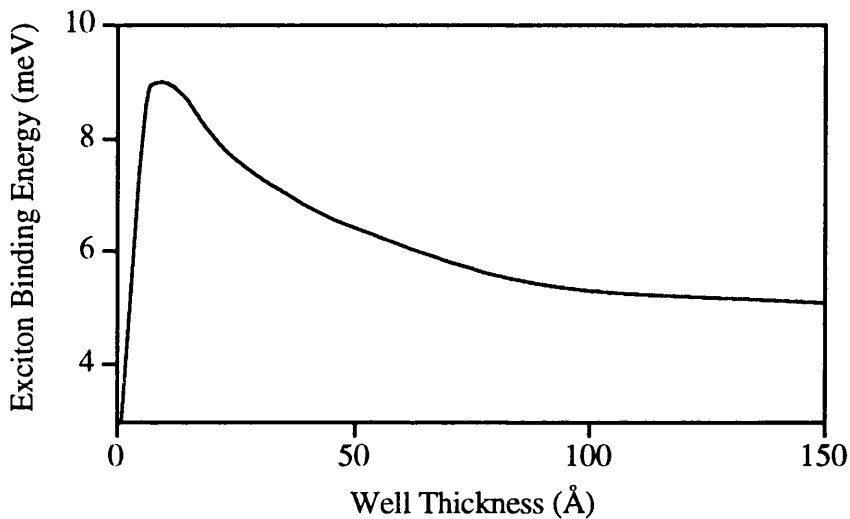
Figure 6.9 Exciton binding energy vs quantum well width for heavy holes in $In_{0.53}Ga_{0.47}As/In_{0.52}Al_{0.48}As$ quantum wells (from Reference 11)

This maximum should therefore represent the minimum exciton size in the plane of the well. The PL spectrum of #B303 does not, however, show the presence of monolayer splitting in the luminescence from the 15Å well, suggesting that the actual maximum binding energy may occur closer to a well thickness of 20Å. The binding energy for a 20Å well can be used to calculate the Bohr radius of the 2D exciton, from which an estimate of ≈ 180Å can be made for the average island size at the $In_{0.53}Ga_{0.47}As/In_{0.52}Al_{0.48}As$ interface for growth with minimum arsenic overpressure at a substrate temperature of 525°C.

6.5 Effect of Arsenic Overpressure

Sample #B227 was grown using the same growth conditions as #B291 but with an arsenic pressure of twice the minimum necessary to suppress In droplet formation. The photoluminescence spectrum of B227 is shown, together with B291 for comparison, in Figure 6.10. The monolayer splitting present in the sample B291, grown using the minimum possible arsenic pressure, is not present when the arsenic flux density is doubled. This is probably due to a reduction in the surface mobilty of the group III species, which shrinks the average size of the monolayer islands at the interface.

The linewidths of the individual peaks in the spectrum of sample #B227 are similar to those obtained for #B291 and #B303. The intensity of the photoluminescence peaks of sample #B227 is approximately half that of #B291. This suggests that an improvement in interface quality is obtained by using the minimum As_2 overpressure.
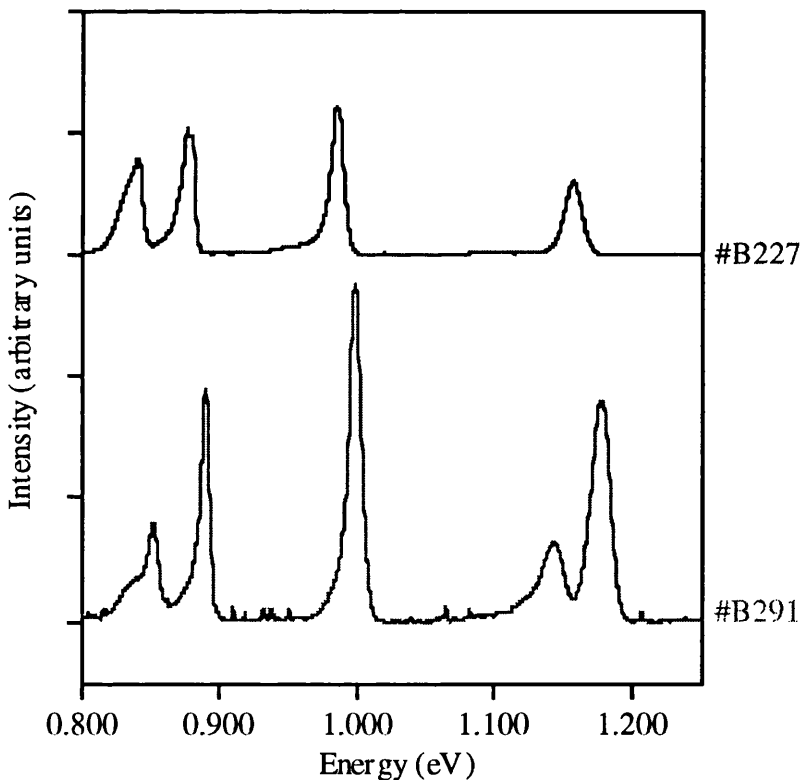
Figure 6.10. Photoluminescence spectra of #B227 and #B291. The vertical scale has been kept constant for both samples.

6.6 Comparison of Experimental Peak Energies with Theoretical Predictions

The values shown in Table 6.2 (taken from Kopf *et al* [18] and modified to take into account non-parabolicity[19] in the well) were used in iterative software based on the model of Kawai *et al* [20] to calculate the conduction and valence band confinement energies for $In_{0.53}Ga_{0.47}As$ quantum wells in $In_{0.52}Al_{0.48}As$.

E_g (eV)	m_n^* / m_0	m_p^* / m_0	$\Delta E_c/\Delta E_g$	$\Delta E_v/\Delta E_g$
0.792	0.0427	0.41	0.65	0.35

Table 6.2. Parameters used in the calculation of QW confinement energies.

Figure 6.11 shows a comparison of the theoretically predicted energies with those obtained experimentally.
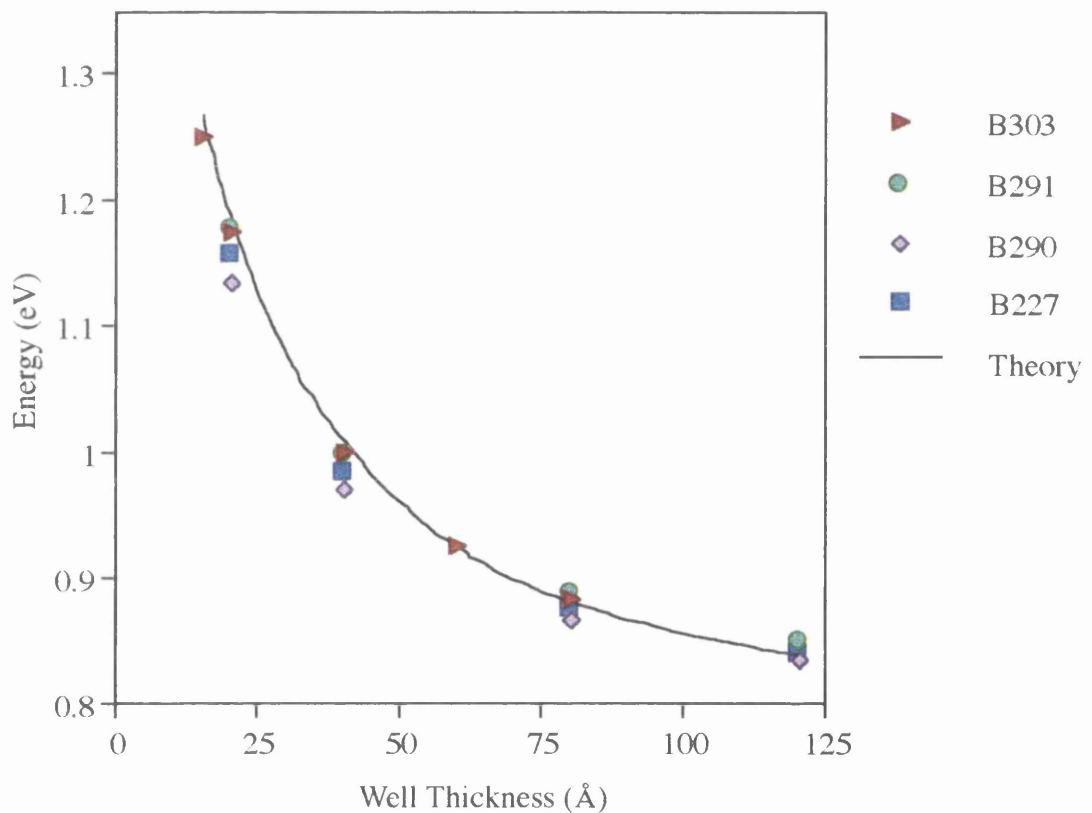
Figure 6.11. Comparison of measured peak energies for the quantum wells in sample #B227, #B290, #B291 and #B303 with theoretical calculations based on Kawai.

The measured confinement energies are, in general, close to the theoretically predicted values. There is, in particular, very good agreement between the predicted and experimental results for sample #B291 and #B303,

which had the most intense photoluminescence output and monolayer splitting on the 20Å well peak.

The well thicknesses calculated from the confinement energies measured for sample #B303 are shown in Table 6.3. The difference between the target and calculated thickness is very small for all of the wells. The well widths calculated from the measured PL energies are in every case within one monolayer of the target widths.

Target Thickness (Å)	Calculated Thickness (Å)	Error (Å)	Error (monolayers)
80	78.6	1.4	0.48
60	59.5	0.5	0.17
40	41.5	1.5	0.51
20	21.1	1.1	0.37
15	16	1	0.34

Table 6.3. Well thicknesses calculated from measured confinement energies for sample #B303.

6.7 Conclusions

High quality $In_{0.53}Ga_{0.47}As/In_{0.52}Al_{0.48}As$ quantum well structures have been grown with PL linewidths comparable to the best reported in the literature. RHEED oscillations were used to calibrate the group III fluxes and obtain the desired alloy compositions, growth rates and thicknesses. Comparison of measured peak energies with theoretical predictions has shown that the well thicknesses obtained agree very well with the target thicknesses.

Samples grown at temperatures of 525°C and 535°C, using the minimum arsenic overpressure, clearly show the presence of monolayer splitting in the PL spectra in 20Å wide wells, indicating that smooth interfaces have been obtained without the need to interrupt growth. The use of a high arsenic overpressure lowers the surface mobility of the group III species and causes a reduction in the average island size at the interface, which can result in the disappearance of the monolayer splitting in the PL spectrum. The exciton binding energy for a 20Å well gives an estimate of ≈ 180Å for the average island size at an $In_{0.53}Ga_{0.47}As/In_{0.52}Al_{0.48}As$ interface grown at 525°C with minimum arsenic overpressure.

Band filling due to charge transfer from residual donors in the $In_{0.52}Al_{0.48}As$ has been found to be the dominant broadening mechanism of the PL linewidths from the quantum well samples grown at lower substrate temperatures but the linewidth can be reduced by increasing the substrate temperature during growth. This improves the quality of the $In_{0.52}Al_{0.48}As$ and causes a drop in the sheet charge density at the interface. The linewidth of the samples still appears to be controlled by the quality of the $In_{0.52}Al_{0.48}As$ and the roughness of the first $In_{0.52}Al_{0.48}As$ /$In_{0.53}Ga_{0.47}As$ interface of each well.

6.8 References

1 'Heterointerfaces in Quantum Wells and Epitaxial Growth Processes: Evaluation
        by Luminescence Techniques'
        M.A. Herman, D. Bimberg and J. Christen
        Journal of Applied Physics 1991 Vol.70 No. 2 ppR1-R52

2 'Quantum Wells and Superlattices'
        Edited by C.R. Leavens and R. Taylor
        (Plenum, New York, 1988)

3 'One Atomic Layer Heterointerface Fluctuations in GaAs-AlAs Quantum Well
        Structures and Their Suppression by Insertion of Smoothing Period in
        Molecular-Beam Epitaxy'
        H. Sakaki, M. Tanaka and J. Yoshino
        Japanese Journal Of Applied Physics Part 2-Letters 1985 Vol.24 No.6

4 'Structural-Changes of the Interface, Enhanced Interface Incorporation of
        Acceptors, and Luminescence Efficiency Degradation in GaAs Quantum
        Wells Grown by Molecular-Beam Epitaxy Upon Growth Interruption'
        D. Bimberg, D. Mars, J.N. Miller, R. Bauer, D. Oertel
        Journal Of Vacuum Science & Technology B-Microelectronics Processing and
        Phenomena 1986 Vol.4 No.4 pp.1014-1021

5 'Kinetics of Island Formation at the Interfaces of
$Al_xGa_{1-x}As/GaAs/Al_xGa_{1-x}As$ Quantum Wells Upon Growth Interruption
D. Bimberg, D. Mars, J. N. Miller, R. Bauer, D. Oertel, J. Christen
Superlattices And Microstructures 1987 Vol.3 No.1 pp.79-82

6 'Optical Properties of High Quality InAlAs/InGaAs SQWs Grown by MBE
Using Specially Refined In and Al Sources'
T. Mishima, J. Kasai, Y. Uchida and S. Takahashi
Journal of Crystal Growth 1989 Vol.95 No.6 pp338-342

7 'GaInAs-AlInAs Heterostructures for Optical Devices Grown by MBE'
D.F. Welch, G.W. Wicks, D.W. Woodard and L.F. Eastman
Journal of Vacuum Science & Technology B-Microelectronics Processing and
Phenomena 1983 Vol.1 No.2 pp.202-204

8 'Luminescence Line Shape Broadening Mechanisms in GaInAs/AlInAs
Quantum Wells'
D.F. Welch, G.W. Wicks and L.F. Eastman
Applied Physics Letters 1985 Vol.46 No.10 pp991-993

9 'Ultrathin GaAs/GaAlAs Layers Grown By MOCVD and Their Structural
Characterization
N. Watanabe and Y. Mori
Surface Science 1986 Vol.174 No.1-3 pp.10-18

10 'Correlation of Optical-Spectra and Atomic Scale Structure of AlInAs-GaInAs
Quantum Wells
A. Juhl, D. Oertel, C. Maczey, D. Bimberg, K. Carey, R. Hull, G.A. Reid
Superlattices And Microstructures 1987 Vol.3 No.3 pp.205-209

11 'Quantum Wells and Superlattices'
Edited by C.R. Leavens and R. Taylor
(Plenum, New York, 1988)

12 'Measurement Of The Conduction-Band Discontinuity Of Molecular-Beam Epitaxial Grown $In_{0.52}Al_{0.48}As/In_{0.53}Ga_{0.47}As$, n-n Heterojunction By C-V Profiling
R. People, K.W. Wecht, K. Alavi, A.Y. Cho
Applied Physics Letters 1983 Vol.43 No.1 pp.118-120

13 'GaInAs-AlInAs Heterostructures for Optical-Devices Grown by MBE
D.F. Welch, G.W. Wicks, D.W. Woodard and L.F. Eastman
Journal Of Vacuum Science & Technology B-Microelectronics Processing and Phenomena 1983 Vol.1 No.2 pp.202-204

14 'Cathodoluminescence Investigations of GaAs Multiple Quantum Wells'
D. Bimberg, J. Christen
Acta Physica Polonica A 1986 Vol.69 No.5 pp.841-849

15 'Structural-Changes of the Interface, Enhanced Interface Incorporation of Acceptors, and Luminescence Efficiency Degradation in GaAs Quantum Wells Grown By Molecular-Beam Epitaxy Upon Growth Interruption'
D. Bimberg, D. Mars, J.N. Miller, R. Bauer, D. Oertel
Journal Of Vacuum Science & Technology B-Microelectronics Processing and Phenomena 1986 Vol.4 No.4 pp.1014-1021

16 'Heterointerfaces in Quantum Wells and Epitaxial Growth Processes: Evaluation by Luminescence Techniques'
M.A. Herman, D. Bimberg and J. Christen
Journal of Applied Physics 1991 Vol.70 No.2 ppR1-52

17 'Image Charges in Semiconductor Quantum-Wells - Effect on Exciton Binding-Energy'
B. Tran Thoai, R. Zimmermann, M. Grundmann and D. Bimberg
Physical Review B-Condensed Matter 1990 Vol.42 No.9 pp.5906-5909

18 'Band Offset Determination in Analog Graded Parabolic and Triangular Quantum-Wells Of GaAs/AlGaAs And GaInAs/AlInAs'
R.F. Kopf, M.H. Herman, M.L.Schnoes, A.P. Perley, G. Livescu and M. Ohring
Journal Of Applied Physics 1992 Vol.71 No.10 pp.5004-5011

19 'Effects of Compositional Clustering on Electron-Transport In $In_{0.53}Ga_{0.47}As$'
J.H. Marsh
Applied Physics Letters 1982 Vol.41 No.8 pp.732-734

20 'Photoluminescence of AlGaAs GaAs Quantum Wells Grown by Metalorganic Chemical Vapor-Deposition'
H. Kawai, K. Kaneko and N. Watanabe
Journal Of Applied Physics 1984 Vol.56 No.2 pp.463-467

Chapter 7

Quantum Transport Measurements on Si ∂- and Slab-doped $In_{0.53}Ga_{0.47}As$ Grown by MBE

7.1 Introduction

The technique of delta(∂)-doping is performed by interrupting the growth of a semiconductor material to allow the deposition of dopant impurities onto the exposed surface. Growth is then recommenced, with the aim of confining the impurities to the doping plane. Ideally, this should result in a delta-function-like dopant distribution, although in practice this is not obtained. It is, nevertheless, this ideal distribution which gives the technique gets its name.

∂-doping, also called planar- or spike-doping, was first used by Bass[1] to produce dopant spikes at substrate/layer interfaces grown by MOCVD. It was subsequently investigated by Wood et al [2] as a means of achieving abrupt Ge doping profiles for MBE-grown GaAs. Growth interrupts were used to produce doping in parallel atomic planes in order to synthesise uniform or complex doping profiles without the need to change the Ge furnace temperature. The initial belief that it would be possible to achieve equivalent bulk doping densities very much greater than those obtainable by conventional doping methods proved to be difficult to achieve in practice due to saturation effects[3,4] which limit the realisable 2-dimensional doping density.

The properties of ∂-doped GaAs structures have attracted interest from researchers with a number of different interests. In particular, much work on the low temperature magnetotransport characteristics of such material[5] has been carried out, and the free-electron concentrations and mobilities of individual sub-bands have been examined using Shubnikov-de Haas (SdH) and persistent photoconductivity measurements.

Applications for ∂-doping have been investigated by several authors, and current applications include non-alloyed ohmic contacts[6], ∂-doped field effect transistors (∂-FETs)[7], and doping of modulation doped $GaAs/Al_xGa_{1-x}As$

heterojunctions in the form of ∂-planes in the $Al_xGa_{1-x}As$[8,9,10]. The use of ∂-doping in $GaAs/Al_xGa_{1-x}As$ high electron mobility transistor (HEMT) structures has been shown to result in an increase in the mobility of the two-dimensional electron gas (2DEG) produced at the channel/spacer heterointerface, particularly in shallow HEMTs. This is thought to be due to two factors:-

    a) The use of ∂-doping allows the spatial separation of the dopant intended to produce carriers in the 2DEG, and the dopant intended to reduce surface depletion; thereby reducing the scattering in the 2DEG[11].

    b) The conduction band well formed by the ∂-doping confines a proportion of the free carriers and produces a screening effect which reduces the scattering caused by ionised dopant atoms[12].

There has as yet been little reported work on the properties of ∂-doped $In_{0.53}Ga_{0.47}As$, and what information there is[13], has not been supported by theoretical calculations which are essential if a comprehensive picture of dopant behaviour is to be built up. This chapter presents the results of quantum transport measurements performed on a series of MBE grown $In_{0.53}Ga_{0.47}As$ samples, either ∂-doped with Si or with the Si impurities distributed uniformly through thin 'slabs' of $In_{0.53}Ga_{0.47}As$.

7.2 High Field Magneto-Transport in 2 Dimensions

As in the 3D case, the application of an electric field E parallel to a 2DEG causes electrons to be accelerated parallel to the applied field until the velocity reaches a steady state. The addition of a magnetic field perpendicular to the plane of the 2DEG produces a Lorentz force perpendicular to both the direction of electron motion and the magnetic field, which results in the electrons describing circles at a constant frequency, known as the *cyclotron* frequency ω_c, which is given by:-

$$\omega_c = \frac{qB}{m^*} \qquad (7.1)$$

where m^* is the electron effective mass, q is the charge on an electron, and B is the applied magnetic field.

For the ideal case, with no scattering, the central point around which the orbits are rotating drifts in a direction perpendicular to the E-field with a constant velocity given by:-

$$v_B = \frac{E}{B}$$

(7.2)

This effect is a consequence of acceleration of the electrons by the E-field being deflected into a direction parallel to the B-field by the Lorentz force. A schematic illustration of this motion is given in Figure 7.1.
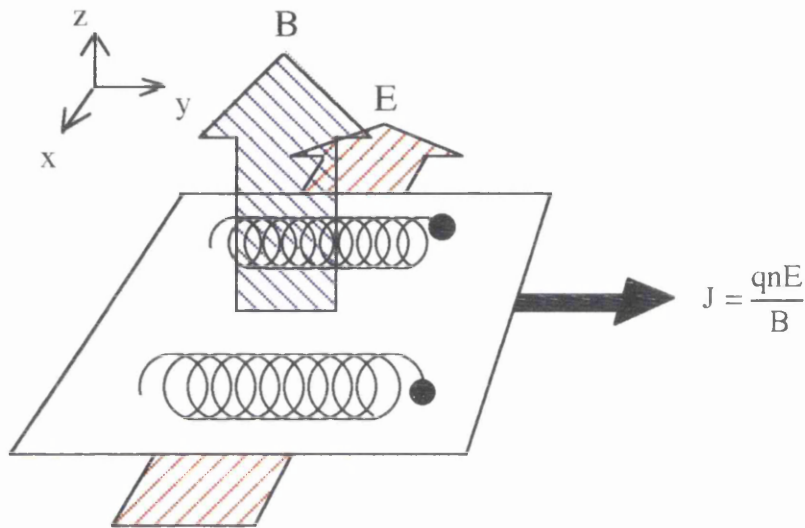
Figure 7.1. Motion of carriers in a 2D electron system with crossed magnetic (B) and electric (E) fields. While rotating, the carriers drift in a direction normal to both B and E, giving rise to a current density J=qnE/B (from reference 15)

The current parallel to the E-field is therefore zero and the resistivity ρ_{xx} defining the electric field strength along the current path also becomes zero since there is no E-field component in the direction of the current flow i.e.

$$\rho_{xx} = 0$$

(7.3)

The current density in a direction parallel to the B-field is given by:-

$$J = qnv_B = \frac{qnE}{B}$$

(7.4)

where n is the carrier density per unit area. The Hall resistivity ρ_{xy} which relates E and J is therefore given by:-

135

$$\rho_{xy} = \frac{B}{nq} \qquad (7.5)$$

This makes the ideal 2D system rather surprising since the values of ρ_{xx} and ρ_{xy} relate an electric field with a current which flows perpendicular to it. In a realistic system scattering takes place and the value of ρ_{xx} will generally be expected to be non-zero. Under certain conditions, however, quantisation of the allowed orbits in a 2D system can produce conditions where scattering events are disallowed, and the behaviour resembles the ideal case.

In high magnetic fields, only a discrete set of orbits with well defined energies are available for an electron to occupy. The allowed radii, known as *Landau* radii, are given by :-

$$r_l = \sqrt{\frac{2\hbar(l - \frac{1}{2})}{qB}} \qquad (7.6)$$

where l is an integer with values 1, 2, 3, . . . and the energy for each Landau level is given by :-

$$E_l = \frac{m^* \omega_c^2 r_l^2}{2} = (l - \frac{1}{2})\hbar\omega_c \qquad (7.7)$$

Individual Landau levels are thus separated by a characteristic energy, $\hbar\omega_c$. An electron encountering a defect can only scatter into a new Landau level if the energy exchange of the scattering event is a multiple of $\hbar\omega_c$. At low temperatures and high magnetic fields, the value of $\hbar\omega_c$ is very much larger than kT and scattering between Landau levels is forbidden. In these circumstances only elastic scattering events within the same Landau level are permitted and these are limited by the availability of empty orbits in the same level. The electrons must obey the Pauli exclusion principle, which restricts the number of electrons to the degeneracy of each Landau level. The maximum density of electrons in any Landau level, s, is therefore given by :-

$$s = \frac{qB}{h} \qquad (7.8)$$

Total suppression of scattering occurs when all the available states of occupied carriers are filled and all higher energy Landau levels are empty. This is obtained when the Fermi level is between two Landau levels, leading to a vanishing electrical resistivity, ρ_{xx}. The oscillatory behaviour of the electrical resistance with reciprocal magnetic field, produced by the Fermi level crossing individual Landau levels, is known as the *Shubnikov-de Haas* [14] (SdH) effect. The periodicity of SdH oscillations can be used to give the carrier density in a 2DEG, although, in the case of multiple sub-band occupancy, each sub-band gives rise to a separate series with its own periodicity and Fourier techniques must be used to determine the fundamental fields of the different series.

The total electron concentration at the vanishing point of ρ_{xx}. is the product of the number of filled Landau levels and the degeneracy of the occupied Landau levels which is given by equation 7.8. Thus :-

$$n = \frac{lqB}{h} \qquad (7.9)$$

The Hall resistivity, ρ_{xy}, is therefore independent of the magnetic field at this point and the ρ_{xy}, vs B curve forms plateaux with values given by :-

$$\rho_{xy} = \frac{h}{lq^2} \qquad (7.10)$$

This is known as the *quantum Hall effect* [15] (QHE).

7.3 Experimental

7.3.1 Sample Preparation & Growth Conditions

Quarter wafer samples of InP were indium bonded to silicon wafers, which were then mounted into standard spring loaded wafer holders. Si wafers were used in preference to the solid molybdenum blocks since better temperature controllability and uniformity were obtained. The heater stage temperature measured by a thermocouple gave a temperature reading very close to the sample temperature measured by an optical pyrometer, eliminating the possibility of large temperature differences across the sample caused by variations in the thermal contact between the substrate and the block. De-oxidation of the substrates was performed in the MBE buffer chamber by heating the samples to 400°C for a period of several hours. The RHEED diffraction pattern substrates showed the

presence of surface reconstruction on transfer of the wafers to the growth chamber.

To achieve consistent results, the layers used in this study were grown under a standardised set of growth conditions at a substrate temperature of 525°C and an As_2 flux density of twice the minimum value needed to suppress droplet formation at this temperature[16]. The In and Ga fluxes were set from RHEED intensity oscillations on InAs and GaAs substrates respectively[17], and periodically checked to confirm growth of $In_{0.53}Ga_{0.47}As$ on InP at $1.0\mu m/hr$. These procedures ensured the complete incorporation of the incident In flux and the growth of layers which were lattice matched to the InP substrate to within ± 150ppm. It has been shown that even small amounts of mismatch can significantly influence the surface of the sample during growth, therefore precise compositional control is vital if reproducible results are to be obtained.

7.3.2 Sample Structures

Two types of test sample were grown; slab- and ∂-doped. The structure of both types was similar: $0.5\mu m$ of $In_{0.53}Ga_{0.47}As$ was grown, followed by the ∂- or slab doped layer, and a final $0.5\mu m$ of $In_{0.53}Ga_{0.47}As$ on top (see Figure 7.2).
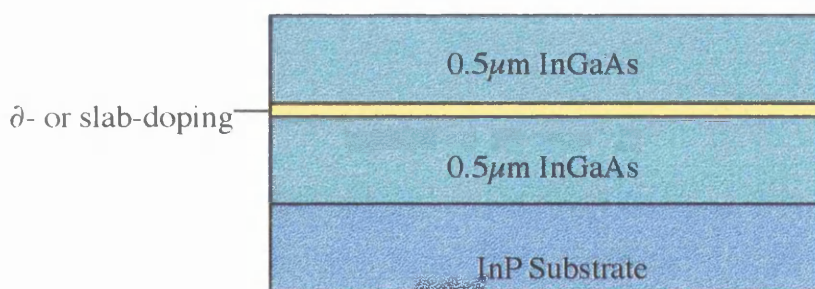
Figure 7.2. Structure of test samples used for this study

The silicon cell was calibrated using low-field Hall measurements of the carrier density in a series of $In_{0.53}Ga_{0.47}As$ layers uniformly doped with Si. A least squares fit to the data was then used to calculate the furnace temperature necessary to give the desired doping density for the growth of slab-doped layers at $1.0\mu m/hr$. The slabs were doped with a constant number of Si atoms, corresponding to a sheet concentration of $5 \times 10^{12} cm^{-2}$. All of the ∂-doped structures were grown with a Si-cell temperature corresponding to a bulk doping level of $1 \times 10^{18} cm^{-3}$ for growth at $1.0\mu m/hr$. The only difference between each ∂-doped sample was therefore the duration of the growth interrupt used to perform

the ∂-doping. The ∂-doping was performed at the growth temperature of 525°C with the As2 shutter open to stabilise the surface.

7.4 Magnetotransport Measurements

Quantum transport measurements were performed on Hall bars defined by photolithography. Standard a.c. techniques were used at a temperature of 1.2K, with magnetic fields up to 13T and typical bias currents of 10-100nA. The high quality of the ∂-doped layers grown for this study is demonstrated by the observation of the quantum Hall effect (QHE) in the samples. Figure 7.3 shows ρ_{xx} and ρ_{xy} as a function of applied magnetic field for a ∂-doped sample with a free electron density of 1.45×10^{12}cm^{-2}. The ρ_{xy} curve contains a clear $l=6$ plateau, suggesting that additional plateaux would be seen at higher magnetic fields. The smaller plateau at a magnetic field of ≈ 6.5T does not correspond to an integer ρ_{xy} plateau. A similar effect has been observed in magnetotransport measurements performed on In$_{0.53}$Ga$_{0.47}$As/InP[18] heterojunctions and has been attributed to interaction between occupied sub-bands.
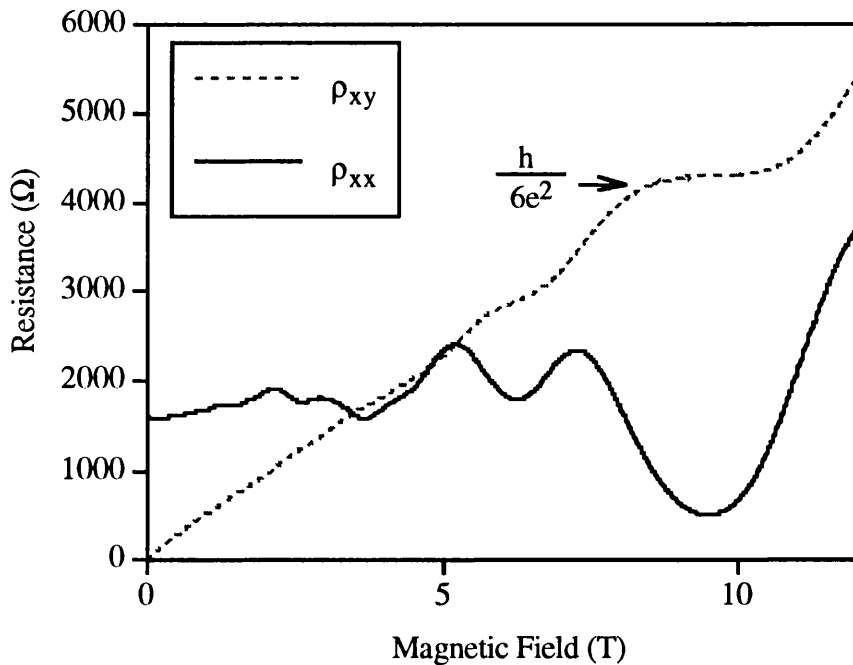
Figure 7.3. Shubnikov-de Haas and quantum Hall effect curves for high mobility ∂-doped In$_{0.53}$Ga$_{0.47}$As with a measured $n_s = 2 \times 10^{12}$cm^{-2}.

Figure 7.4 shows a comparison between SdH oscillations taken in the dark and those taken after illumination. The change in individual sub-band densities

139

after illumination is negligible, indicating little or no persistent photoconductivity associated with deep states.
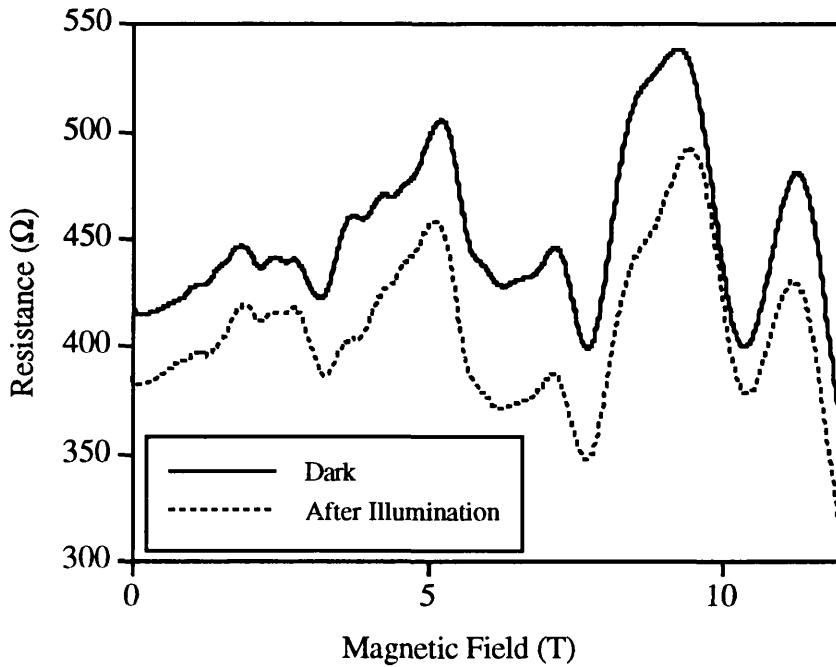
Figure 7.4. Shubnikov-de Haas oscillations before and after illumination for a 30ML thick slab-doped InGaAs sample with intended $n_s = 5 \times 10^{12} cm^{-2}$ and measured $n_s = 4.03 \times 10^{12} cm^{-2}$. The individual sub-band densities show negligible change after illumination.

Individual sub-band densities deduced from fast Fourier transform (FFT) analysis of SdH data for a representative set of ∂-doped $In_{0.53}Ga_{0.47}As$ samples with design doping densities of $2 \times 10^{12} cm^{-2}$, $3 \times 10^{12} cm^{-2}$, $1.5 \times 10^{13} cm^{-2}$ and $5 \times 10^{12} cm^{-2}$ are shown in Table 7.1 together with data for a 20ML slab-doped sample.

	∂-doped				Slab-doped
Subband Index	2×10^{12} (cm^{-2})	3×10^{12} (cm^{-2})	5×10^{12} (cm^{-2})	1.5×10^{13} (cm^{-2})	5×10^{12} 20ML
i=0	0.89×10^{12}	1.15×10^{12}	1.60×10^{12}	7.62×10^{11}	2.04×10^{12}
i=1	0.36×10^{12}	0.56×10^{12}	0.81×10^{12}	4.72×10^{11}	1.07×10^{12}
i=2	0.15×10^{12}	0.25×10^{12}	0.36×10^{12}	2.65×10^{11}	0.52×10^{12}
i=3	0.04×10^{12}	0.09×10^{12}	0.14×10^{12}	-	0.24×10^{12}
i=4	-	-	-	-	0.08×10^{12}
Σn_i	1.45×10^{12}	2.05×10^{12}	2.89×10^{12}	1.5×10^{12}	3.95×10^{12}
$n_{i=0}/n_{i=1}$	2.47	2.05	1.97	1.61	1.90

Table 7.1 Measured sub-band carrier densities for $In_{0.53}Ga_{0.47}As$ ∂-doped samples with design doping densities of 5×10^{12} cm^{-2}, 4×10^{12} cm^{-2}, 3×10^{12} cm^{-2}, 2×10^{12} cm^{-2} 1.5×10^{13} cm^{-2} and a 20ML slab with Si atoms equivalent to a density of 5×10^{12} cm^{-2}.

For all the ∂-doped samples the measured free electron concentration N_e is consistently smaller than the design dopant density N_d and the difference between the two figures increases as the design dopant density is increased. The activity of the Si dopant in the samples is given in Table 7.2.

Design Doping Density ($\times 10^{12}$cm^{-2})	Measured Carrier Density ($\times 10^{12}$cm^{-2})	Ratio of Free Electrons to Dopant Atoms (%)
2	1.45	72.3
3	2.05	68.3
5	2.91	58.2
15	1.5	10
5 (20ML)	3.95	79.0

Table 7.2. Activity of Si as Donors in ∂- and slab-doped $In_{0.53}Ga_{0.47}As$.

For $N_d=2\times10^{12}$ cm^{-2} the ratio between the measured carriers and the supplied Si atoms varies is 72.5%, which falls to 10% for $N_d=1.5\times10^{13}$ cm^{-2}. A graph of measured doping density as a function of design doping density is given in Figure 7.5.
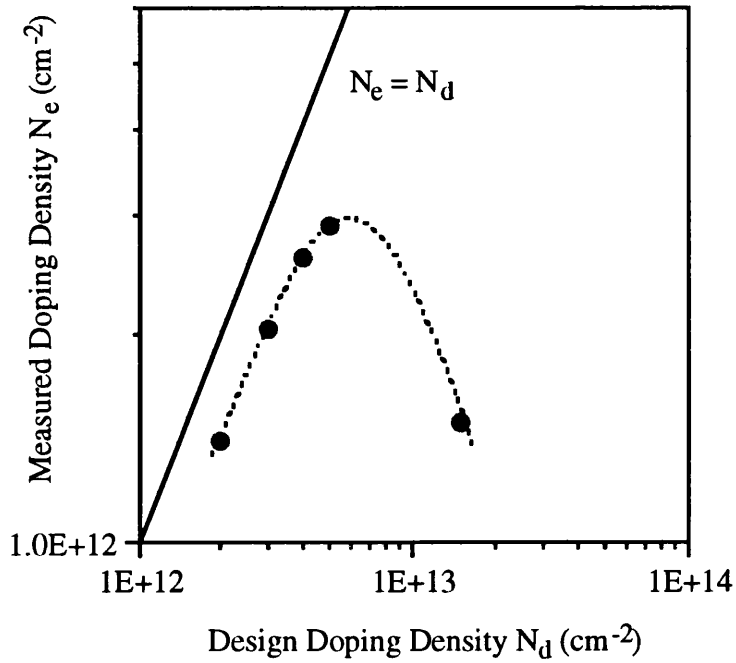
Figure 7.5. Measured doping density vs design doping density for ∂-doped $In_{0.53}Ga_{0.47}As$.

The measured doping density decreases for $N_d > 5 \times 10^{12}$ cm^{-2}. This behaviour is consistent with increasing amphoteric behaviour as the volume density of Si is increased and suggests that the amphoteric limit for ∂-doping is $\approx 3 \times 10^{12}$ cm^{-2}. The proportion of activated donors for a design doping density of 5×10^{12} cm^{-2} is 57.8%, however this rises to 79.0% when a similar number of Si atoms are distributed through a 20ML slab. The FFT power spectra for the 5×10^{12}cm^{-2} ∂-doped and 20ML slab doped samples are given in Figure 7.6.
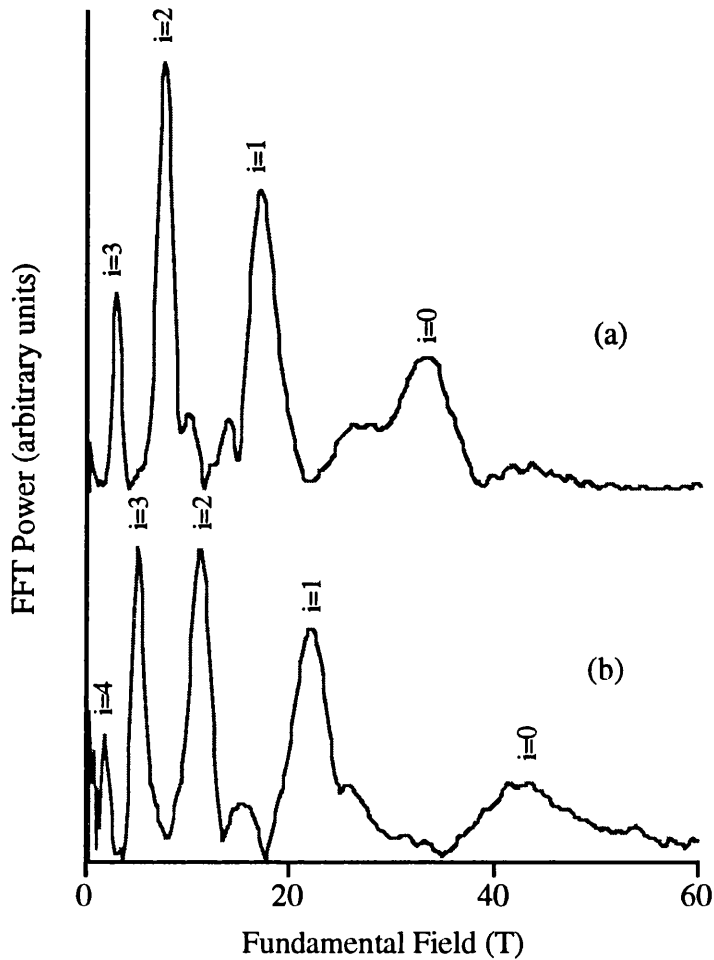
Figure 7.6. FFT power spectra for a) a $5 \times 10^{12} \text{cm}^{-2}$ ∂-doped sample and b) a 20ML slab-doped sample.

The shift to higher fundamental field values for all of the FFT peaks in the slab indicates an increase in carrier population for each of the individual sub-bands. There is also an additional i=4 sub-band present when the Si is distributed throughout 20ML. This is consistent with a decrease in amphoteric behaviour when the Si is deposited during growth of a thin slab.

The ratio between the densities in the first two subbands of Table 7.1, when compared with theoretical predictions, gives an effective measure of the spreading of the Si atoms away from the doping plane. A comparison between measured sub-band densities for the $2 \times 10^{12} \text{cm}^{-2}$ sample and those calculated self-consistently[19] assuming a uniform Si spreading of 2ML, 34ML and 38ML is given in Table 7.3.

143

Subband Index	Measured Density $(\times 10^{12}\text{cm}^{-2})$	Theoretical Density for 2ML spread $(\times 10^{12}\text{cm}^{-2})$	Theoretical Density for 34ML spread $(\times 10^{12}\text{cm}^{-2})$	Theoretical Density for 38ML spread $(\times 10^{12}\text{cm}^{-2})$
i=0	0.89	0.946	0.900	0.887
i=1	0.36	0.330	0.364	0.367
i=2	0.15	0.137	0.142	0.142
i=3	0.05	0.040	0.045	0.046
i=4	-	0.007	0.008	0.008
$n_{i=0}/n_{i=0}$	2.472	2.870	2.471	2.415

Table 7.3. Comparison between measured subband populations for design dopant density of $2\times 10^{12}\text{cm}^{-2}$ and theoretical subband populations for a dopant density of $1.45 \times 10^{12}\text{cm}^{-2}$ with a spreading of 2ML, 34ML and 38ML.

The ratio between the carrier densities for the calculation assuming a spreading of 34ML sample is in good agreement with the experimental measurements, indicating that the Si donors are distributed through $\approx 100\text{Å}$. In Table 7.4 the estimated spreading for design ∂-doping densities of $2\times 10^{12}\text{cm}^{-2}$ and $5\times 10^{12}\text{cm}^{-2}$ are compared with the estimated spreading for the nominally 20ML slab-doped sample.

Design Doping Density $(\times 10^{12}\text{cm}^{-2})$	Estimated Spreading (ML)
2	34
5	47
5 (20ML)	40

Table 7.4. Estimated spreading for ∂-doped samples with of $2\times 10^{12}\text{cm}^{-2}$ and , together with the estimated spreading for a nominally 20ML thick slab doped sample with an equivalent N_d of $5\times 10^{12}\text{cm}^{-2}$.

7.5 Conclusions

A series of high quality Si-∂-doped $In_{0.53}Ga_{0.47}As$ layers has been grown by MBE and a systematic study of the magnetotransport properties of such layers has been undertaken for the first time. The electron gas formed at the doping plane has been shown to be quantised into discrete sub-bands with carrier densities which correlate very well with predictions based on self-consistent calculations. The quality of the layers is illustrated by the observation of quantum Hall plateaux for ∂-doped samples with free electron concentrations of $\approx 1.45 \times 10^{12} cm^{-2}$.

The measured free electron concentrations for ∂-doped layers do not correlate well with the design doping density of the samples. The discrepancy increases as the design doping density is increased and, at a design doping density of $1.5 \times 10^{13} cm^{-2}$, only 10% of the intended doping is obtained. This increasingly amphoteric behaviour limits the realisable sheet carrier concentration to $\approx 3 \times 10^{12} cm^{-2}$ at a design doping density of $5 \times 10^{12} cm^{-2}$.

Comparison between measured sub-band densities and self-consistent calculations for ∂-doped samples have shown that the decrease in activity of the Si as donors with increasing doping density is accompanied by increased spreading away from the original doping plane. Distributing Si atoms uniformly through a thin slab doped layer results in an increase in the carrier density in each of the individual sub-bands, and hence a rise in the activity of the Si. In addition the estimated spreading for the slab-doped sample is comparable to that for ∂-doping, suggesting that thin slab-doped layers are the more efficient method of generating high carrier densities in $In_{0.53}Ga_{0.47}As$.

7.6 References

1   'Silicon and Germanium Doping of Epitaxial and Gallium Arsenide Grown by the Trimethylgallium-Arsenide Method'
     S.J. Bass
     Journal of Crystal Growth 1979 Vol.47 No.5 pp613-618

2   'Complex Free-Carrier Profile Synthesis by "Atomic-Plane" Doping of MBE GaAs'
     C.E.C Wood, G. Metze, J. Berry and L.F. Eastman
     Journal of Applied Physics 1980 Vol.51 No.1 pp383-388

3   'Experimental and Theoretical Mobility of Electrons in Delta-Doped GaAs'
    G. Gillman, B. Vinter, E. Barbier, A. Tardella
    Applied Physics Letters 1988 Vol.52 No.12 pp.972-974

4   'Facts and Fancies About the Delta-Doping Layer of Si in MBE-Grown
    GaAs'
    A. Zrenner, F. Koch, K. Ploog
    Gallium Arsenide And Related Compounds 1987 Vol.91 Ch.200 pp171-174

5   E. Skuras, R. Kumar, R.L. Williams, R.A. Stradling, J. E. Dmochowski,
    E.A. Johnson, A. Mackinnon, J.J. Harris, R.B. Beall, C. Skierbeszewski,
    J. Singleton, P.J. van der Wel and P. Wisniewski
    Semiconductor Science and Technology 6 (1991) 535

6   'Delta-doped ohmic contacts to n-GaAs'
    E.F. Schubert, J.E. Cunningham, W.T. Tsang, and T.H. Chiu
    Applied Physics Letters 1986 Vol.49 No.5 pp292-294

7   'The Delta-Doped Field-Effect Transistor (Delta-FET)'
    E.F. Schubert, A. Fischer, K. Ploog
    IEEE Transactions on Electron Devices 1986 Vol.33 No.5 pp.625-632

8   'Fundamental-Studies and Device Application of Delta-Doping in
    GaAs-Layers and in $Al_xGa_{1-x}As$/GaAs Heterostructures'
    K. Ploog, M. Hauser, A. Fischer
    Applied Physics A-Solids And Surfaces 1988 Vol.45 No.3 pp.233-244

9   'Two-Dimensional Electron-Gas of Very High Mobility in Planar Doped
    Heterostructures'
    B. Etienne, E. Paris
    Journal De Physique 1987 Vol.48 No.12 pp.2049-2052

10 'Radiative Electron-Hole Recombination in a New Sawtooth Semiconductor
    Superlattice Grown By Molecular-Beam Epitaxy'
    E.F. Schubert, Y. Horikoshi, K. Ploog
    Physical Review B-Condensed Matter 1985 Vol.32 No.2 Pp.1085-1089

11 'Electron Mobilities Exceeding 10^7 cm^2/Vs in Modulation-Doped GaAs'
   L. Pfeiffer, K.W. West, H.L. Stormer and K.W. Baldwin
   Applied Physics Letters 1989 Vol.55 No.18 pp.1888-1890

12 'Growth and characterisation of shallow two-dimensional electron gas
   (2DEG) structures'
   M.C. Holland, C.R. Stanley, E. Skuras, C.J. Barton and A.R. Long
   Proceedings of the Seventh European Workshop on Molecular Beam Epitaxy
   Bardonecchia, 1993

13 'Transport Properties of Two-Dimensional Electron Gas Systems in
   Delta-Doped Si:InGaAs Grown by Organometallic Chemical Vapour
   Deposition'
   W.P. Hong, F. DeRosa, R. Bhat, S.J. Allen and J.R. Hayes
   Applied Physics Letters 1989 Vol.54 No.5 pp457-459

14 R.A. Stradling in 'Growth and Characterisation of Semiconductors'
   Edited by R.A. Stradling and P.C. Klipstein
   (Hilger, Bristol, 1990)

15 'The Quantized Hall Effect'
   H.L. Stormer and D.C. Tsui
   Science 1983 pp1241-1246

16 'Thermodynamic Analysis and Growth of $In_{0.53}Ga_{0.47}As$ and $In_{0.52}Al_{0.48}As$
   Lattice matched to InP Substrates'
   M. McElhinney and C.R. Stanley
   to be published in the Journal of Crystal Growth

17 'Reduced Indium Incorporation During the MBE Growth of In (Al, Ga) As'
   M. McElhinney and C.R. Stanley
   Electronics Letters 1993 Vol.29 No.14 pp1302-1304

18 'Quantum Hall Effect in $In_{0.53}Ga_{0.47}As$-InP Heterojunctions with Two
    Populated Electric Subbands'
    Y. Guldner, J.P. Vieren, M. Voos, F. Delahaye, D. Dominguez, J.P. Hirtz and
    M. Razeghi
    Physical Review B 1986 Vol.33 No.6 pp3990-3993

19 E. Skuras, M. McElhinney, S.N. Holmes, E.A. Johnson, A.R. Long and
    C.R. Stanley,
    paper in preparation.

Chapter 8

Growth of Device Structures

8.1 Introduction

The growth of device structures by MBE requires an appreciation of the constraints of the technique and the limits imposed by the physical properties of the MBE system used. The design of any device must take into account the practical aspects involved in its growth, and should be tailored to suit the configuration of the MBE reactor. It is also necessary to consider the influence of growth and structural characteristics on the behaviour of the completed device, and to attempt to optimise the device performance by adjusting the growth parameters. This chapter presents MBE growth details and characterisation data for two examples of device structures, and shows how the problems associated with their growth have been overcome.

The first section deals with the growth of lattice-matched HEMTs and demonstrates that information gained from the fundamental studies of the preceding chapters can be usefully employed for the growth of actual devices. The second example illustrates that the RHEED calibration approach used for the growth of lattice matched InGaAs and InAlAs can also be used for the growth of strained structures, in this case a strain-balanced self electro-optic effect device[1] (SEED) structure.

8.2 HEMT Structures

8.2.1 Introduction

HEMTs based on the InGaAs/AlInAs system have demonstrated the lowest noise figure[2,3,4] and the best high frequency response[5,6] of any transistor. Such devices, with useful gain above 100GHz, are of interest for sensing systems in a variety of terrestrial and space applications[7] such as high resolution radar, and collision detectors. This section describes the growth of HEMT structures and presents characterisation data for devices fabricated by the nanoelectronics group at the University of Glasgow.

8.2.2 MBE Growth of HEMT structures

The structure of an existing HEMT wafer grown by MOCVD (at EPI Ltd.) was duplicated to allow the two wafers to be processed in tandem and provide a comparison between the behaviour of MBE and MOCVD material. The structure used for the growth of this sample (#B299) is shown in Figure 8.1.
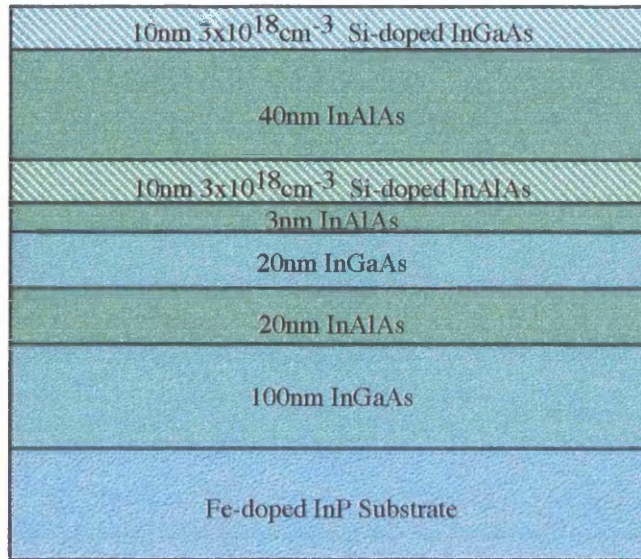
Figure 8.1. Schematic diagram of the structure of sample #B299.

A subsequent sample (#B354) was grown with a modified buffer layer. The structure of this sample is given in Figure 8.2.
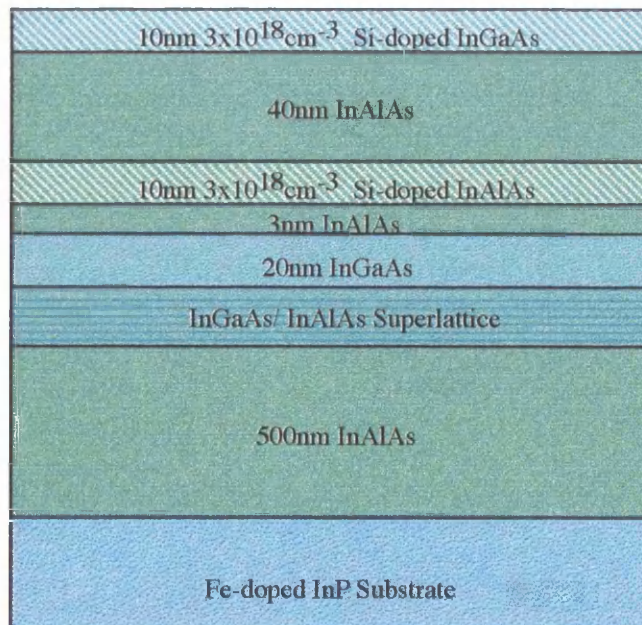
Figure 8.2. Schematic diagram of the structure of sample #B354.

Similar growth conditions were used for both sample #B299 and #B354. Group III flux calibration prior to growth was carried out using the technique described in Chapter 4. The temperature of the In furnace was adjusted to give an InAs growth rate on InAs of 0.625μm/hr and the temperatures of the Ga and Al furnaces were adjusted to give GaAs and AlAs growth rates on GaAs of 0.422μm/hr and 0.441μm/hr respectively. These values gave a growth rate for $In_{0.53}Ga_{0.47}As$ on InP of 1.00μm/hr and an $In_{0.52}Al_{0.48}As$ growth rate of 1.023μm/h. The structures were grown on (100)-orientated Fe-doped InP substrates mounted onto sapphire backed wafer holders. This method of mounting was found to produce a less uniform temperature distribution across the substrate than indium mounting, and gave a centre-to-edge variation of $10°$C. The use of In-mounting was however incompatible with device fabrication involving e-beam patterning which requires a smooth back surface to prevent sample misalignment.

Oxide desorption was performed in the system buffer chamber, using the method discussed in Chapter 5. The samples were heated to a temperature of $375°$C for a period of several hours. On transfer to the growth chamber the surface reconstruction observed by RHEED did not show the presence of a surface oxide layer.

The highest quality interfaces in the quantum well study of Chapter 6 were obtained at substrate temperatures of $535°$C with the minimum As_2 overpressure which was consistent with the growth of $In_{0.53}Ga_{0.47}As$ without surface In droplets. In an attempt to replicate, as far as possible, these conditions, the temperature at the centre of the substrate during the growth of the HEMT structures was set to $530°$C, which corresponded to an edge temperature of $≈540°$C. To compensate for both this slightly higher edge temperature, and a slight drop in incident As_2 partial pressure towards the edge of the substrate produced by the flux distribution of the arsenic cracker, the As_2 partial pressure was calibrated to a value of twice that necessary for $In_{0.53}Ga_{0.47}As$ growth at $535°$C. This value gave a secure margin of error to prevent the possibility of indium droplet formation at the wafer edge.

The Si furnace temperature necessary for the required doping level of 3×10^{18}cm^{-3} was calculated using an Arrhenius plot of Hall carrier density measurements on a series of Si-doped layers. The Si-furnace was degassed at a temperature $20°$C above the doping temperature for a period of 15 minutes and then the temperature was reduced to a lower idling value, prior to the transfer of the substrate from the buffer chamber to the growth chamber. This procedure was employed to prevent a sharp increase in the growth chamber pressure when the

Si-furnace was heated to its doping temperature during the growth of the HEMT structures.

8.2.3 Characterisation

Unfortunately, during fabrication, the MOCVD grown wafer shattered and so no benchmark devices were available for comparison with results from sample #B299. HEMTs were, nevertheless, successfully fabricated on sample #B299. Mushroom shaped gates with footprints ranging from 100nm to 300nm were patterned and recessed non-selectively using wet chemical etching in $H_3PO_4{:}H_2O_2{:}H_2O$. Mesa isolation was also achieved by wet chemical etching in $H_3PO_4{:}H_2O_2{:}H_2O$, although it was found to be necessary to etch down to the InP substrate before isolation was obtained, indicating the existence of parallel conduction at the substrate/epilayer interface. The threshold voltages of the completed devices were in the range of 3 to 5V, dependent on the gate length and drain bias used. Measurement of the DC characteristics, revealed high output conductance (>100mS/mm), and low transconductance (100mS/mm) and a strong kink effect was observed i.e. increased output conductance with increased drain bias. This poor device performance was believed to be due to parallel conduction at the substrate/epilayer interface.

Sample #B354 was grown to attempt to remove the parallel conduction effects seen in #B299 by altering the device structure. An $In_{0.52}Al_{0.48}As$ buffer was used to remove the large bandgap discontinuity at the substrate/epilayer interface. This was followed by a 100 period superlattice with each period composed of 4ML of $In_{0.53}Ga_{0.47}As$ followed by 12ML of $In_{0.52}Al_{0.48}As$. The active region of sample #B354 was identical to that used for sample #B299.

HEMTs were fabricated on #B354 as described above. Device isolation was obtained at an etch depth of ≈60nm indicating that no significant parallel conduction was present at the substrate/epilayer interface. DC characterisation of the devices gave a transconductance of 330mS/mm and an output conductance of 47mS/mm, considerably better than the previous devices fabricated on sample #B299. RF measurements gave a unity current gain cutoff of 167GHz for a gate length of 120nm and RF transconductance of up to 1130mS/mm.

8.2.4 Conclusions

The growth techniques and conditions discussed in the previous chapters have been applied to the growth of HEMT structures. Parallel conduction at the epi-layer/substrate interface (as discussed in Chapter 5) has been shown to be a

problem if the correct buffer design is not used. Devices fabricated on material grown with an $In_{0.52}Al_{0.48}As$ buffer have device characteristics comparable to the best reported lattice matched HEMTs[5,8].

8.3 SEED Device Structures

8.3.1 Introduction

S-SEED arrays operating at 850nm have been shown to be effective as digital photonic logic planes in experiments on parallel optical processing and switching systems[9,10]. However, the clock rates for realistic systems are currently limited by the laser power reaching the device array (milliwatts) and, consequently, there is a need for a better match with suitable higher-power (>1W) lasers. One possible solution to this problem is the development of new SEED arrays capable of exploiting existing efficient laser sources at wavelengths other than 850nm. This section describes the growth and characterisation of a SEED structure designed to operate at 1047nm with a Nd:YLF laser. Nd:YLF lasers have better thermal properties than Nd:YAG and have a fixed wavelength, guaranteeing a good match with specifically tailored switching and diffractive optical components, without special tuning or wavelength stabilisation.

8.3.2 MBE Growth of SEED structures

Due to the difficulty of accurately controlling quaternary growth, good SEED modulators for the 1047-1064nm region fabricated using lattice-matched InGaAsP wells and InP barriers have poor performance. All other attempts to realise SEEDs in this wavelength range have used strained ternary-ternary or binary-ternary MQWs. The MQW in a normal incidence modulator must be 1-2µm thick to achieve a useful contrast ratio without using an asymmetric Fabry-Perot cavity. The strain averaged over the wells and barriers must therefore be balanced close to zero to avoid the propagation of dislocations. It was decided to adopt the approach of Woodward et al.[11] and Fritz et al.[12] by growing an InGaAs buffer structure which deliberately exceeds the critical thickness limit and is relaxed to a larger lattice constant than the GaAs substrate. The MQW modulator is then grown on top the buffer, pseudomorphic to the new lattice constant, with InGaAs wells in compression and GaAs barriers in tension.

The layer structure for the SEED device is given in Figure 8.3.
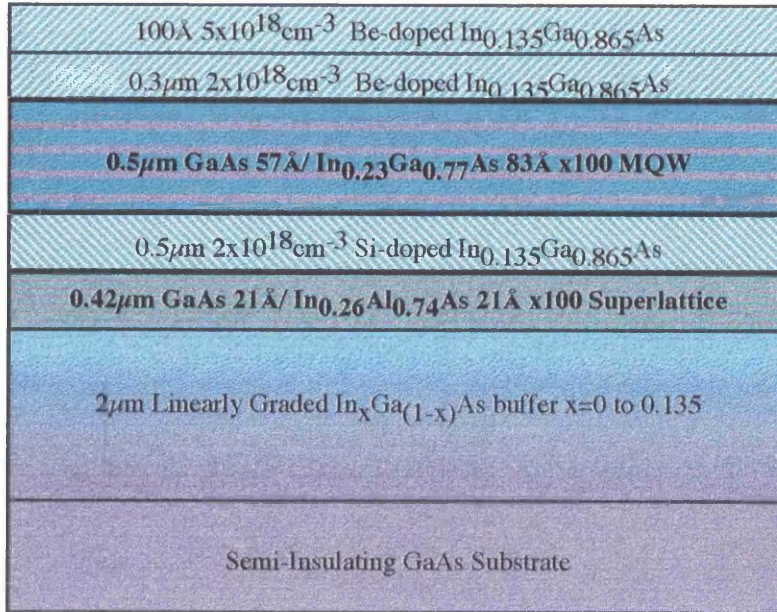
Figure 8.3. Layer structure for SEED device.

The buffer was composed of 2μm of $In_xGa_{(1-x)}As$ with composition linearly graded between x=0 and x=0.135 to reduce threading dislocations. It was not possible to directly program a linear composition ramp using the system control software, only the furnace temperature setpoints could be ramped, so the buffer was grown using ten individual temperature ramps corresponding to composition changes of Δx=0.0135. This enabled a linear composition gradient to be synthesised as shown in Figure 8.4.
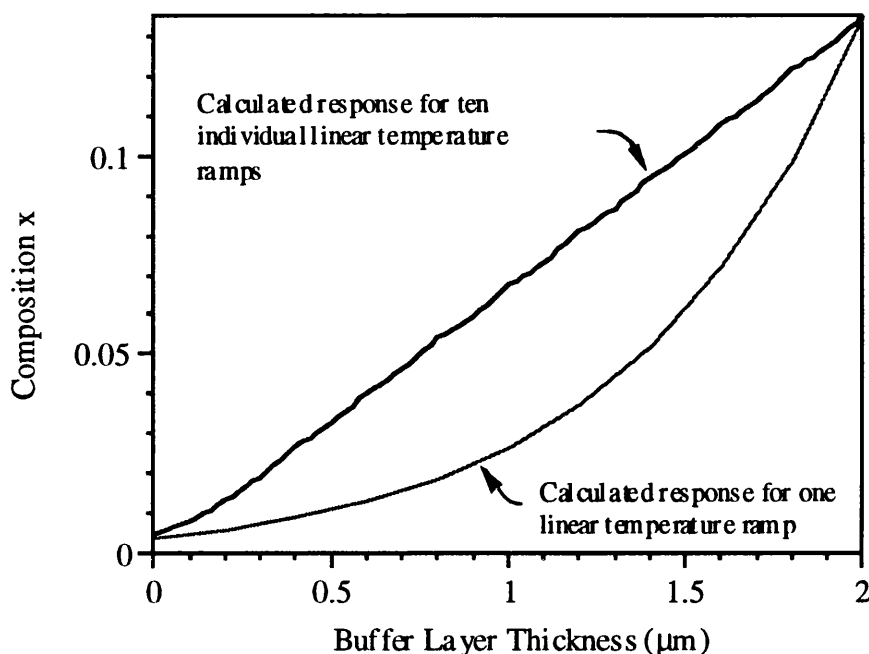
Figure 8.4. Calculated composition vs thickness for single step temperature ramp and ten step temperature ramp for synthesis of linear composition gradient.

The required temperature setpoints for the start and finish of each step were found by performing RHEED intensity oscillation measurements for the growth of InAs on InAs. The required growth rates were scaled by the ratio of the third powers of the lattice constants of InAs and GaAs in a manner analogous to that used in Chapter 4 of this thesis. All $In_xGa_{(1-x)}As$ growth rate (Gr) calculations were performed assuming a GaAs growth rate of $0.865 \mu m/hr$. Details of the growth of each step are given in Table 8.1.

Step	Initial x	Final x	Initial InAs Gr	Final InAs Gr	Average InGaAs Gr	Initial In Temp °C	Final In Temp °C	Time (s)
1	0.0050	0.0135	0.0057	0.0155	0.873	619.3	648.8	825
2	0.0135	0.0270	0.0155	0.0315	0.883	648.8	671.1	815
3	0.0270	0.0405	0.0315	0.0479	0.895	671.1	684.7	804
4	0.0405	0.0540	0.0479	0.0602	0.906	684.7	692.3	795
5	0.0540	0.0675	0.0602	0.0821	0.919	692.3	702.8	783
6	0.0675	0.0810	0.0821	0.1000	0.934	702.8	709.6	771
7	0.0810	0.0945	0.1000	0.1184	0.948	709.6	715.5	759
8	0.0945	0.1080	0.1184	0.1273	0.962	715.5	720.7	748
9	0.1080	0.1215	0.1373	0.1568	0.969	720.7	725.5	743
10	0.1215	0.1350	0.1568	0.1770	0.985	725.5	729.8	731

Table 8.1. Calibration data for the growth synthesis of linear buffer in Sample #B374.

Since the glide of dislocations in crystalline materials is a thermally activated motion, the buffer layer was grown at the relatively low temperature of 420°C to further inhibit dislocation motion. The incident As_2 partial pressure used for the growth of the buffer was 5.5×10^{-7} Torr, close to the minimum calculated in Chapter 4 for InGaAs growth at low temperature.

Flux calibrations for the growth of the active region of the SEED structure were performed assuming 100% relaxation of the buffer to the lattice constant of $In_{0.135}Ga_{0.865}As$, which from Vergard's Law corresponds to 5.708Å. This means that for the growth of $In_{0.135}Ga_{0.865}As$ at 1μm/hr the necessary calibration growth rate of GaAs on GaAs is given by :-

$$\frac{5.65325^3}{5.708^3} \times 0.865 = 0.840 \mu m / hr \qquad (8.1)$$

As discussed in Chapter 4, this value must be modified to take into account thermal expansion at the calibration temperature. Using published values for the thermal expansion coefficient, the Ga calibration setpoint for $In_{0.135}Ga_{0.865}As$ growth therefore becomes 0.850μm/hr. The necessary In and Al calibration setpoints can be similarly calculated. The values used for the growth of the active region of the SEED device are given in Table 8.2.

Alloy	In Calibration Growth Rate (μm/hr)	Ga Calibration Growth Rate (μm/hr)	Al Calibration Growth Rate (μm/hr)	Alloy Growth Rate (μm/hr)
$In_{0.135}Ga_{0.865}As$	0.172	0.850	-	1.000
$In_{0.23}Ga_{0.77}As$	0.326	0.850	-	1.123
$In_{0.26}Al_{0.74}As$	0.172	-	0.378	0.589

Table 8.2. Calibration and alloy growth rates for the growth of #B374. The Ga and Al calibration growth rates refer to the growth of GaAs and AlAs on GaAs, and the In calibration growth rates refer to the growth of InAs on InAs. The alloy growth rates are the expected growth rates for growth on completely relaxed InGaAs with x=0.135.

The substrate temperature was raised to 535°C for the growth of the active region, this temperature was measured at the centre of the wafer and so corresponded to an edge temperature of $\approx$545°C. The As_2 partial pressure used during the growth was 2×10^{-6}Torr, approximately four times that used for the

growth of the buffer. Such a high As_2 overpressure was used since the effects of strain on the desorption characteristics of InGaAs are unknown.

8.3.3 Characterisation

The DCXD rocking curve for sample #B374 is given in Figure 8.5. The splitting for a totally relaxed layer has been shown in Chapter 2 to be related to the mismatch (m) by the equation :-

$$m = \cotan\theta \; \partial\theta \qquad (8.2)$$

where θ is the Bragg angle. For $In_{0.135}Ga_{0.865}As$ on GaAs this gives a splitting of 1299 arcseconds. For strained layers lattice distortion has to be taken into account using the equation :-

$$m = \frac{(1-\nu)}{(1+\nu)}\cotan\theta \; \partial\theta \qquad (8.3)$$

where ν is the Poisson ratio of the material (which must be calculated using Vergard's law as described in Chapter 2). This gives a splitting of 2504 arcseconds for $In_{0.135}Ga_{0.865}As$ on GaAs. From the position of the $In_{0.135}Ga_{0.865}As$ peak in the DCXD rocking curve for sample #B374, it is apparent that the buffer layer has not completely relaxed.

The spacing between the main InGaAs peak and the first order Pendellösung fringe to its left is 1310arcseconds which gives a periodicity of 144Å for the MQW in the device structure. This is 6Å larger than the target thickness of 138Å.

The wavelength of the 300K absorption edge peak (λ_0) also showed a slight discrepancy from the target wavelength, with a value of 1061nm. However, the uniformity of the peak across the wafer was excellent, being within ±0.2nm of 1061nm to a diameter of 1", and ±0.7nm to the full 2". Figure 8.6 shows the transmission-voltage performance of a SEED device. A contrast ratio of 2.0 was obtained between 0 and 10V, which was increased to ≈4.2 by the incorporation of a mirror.
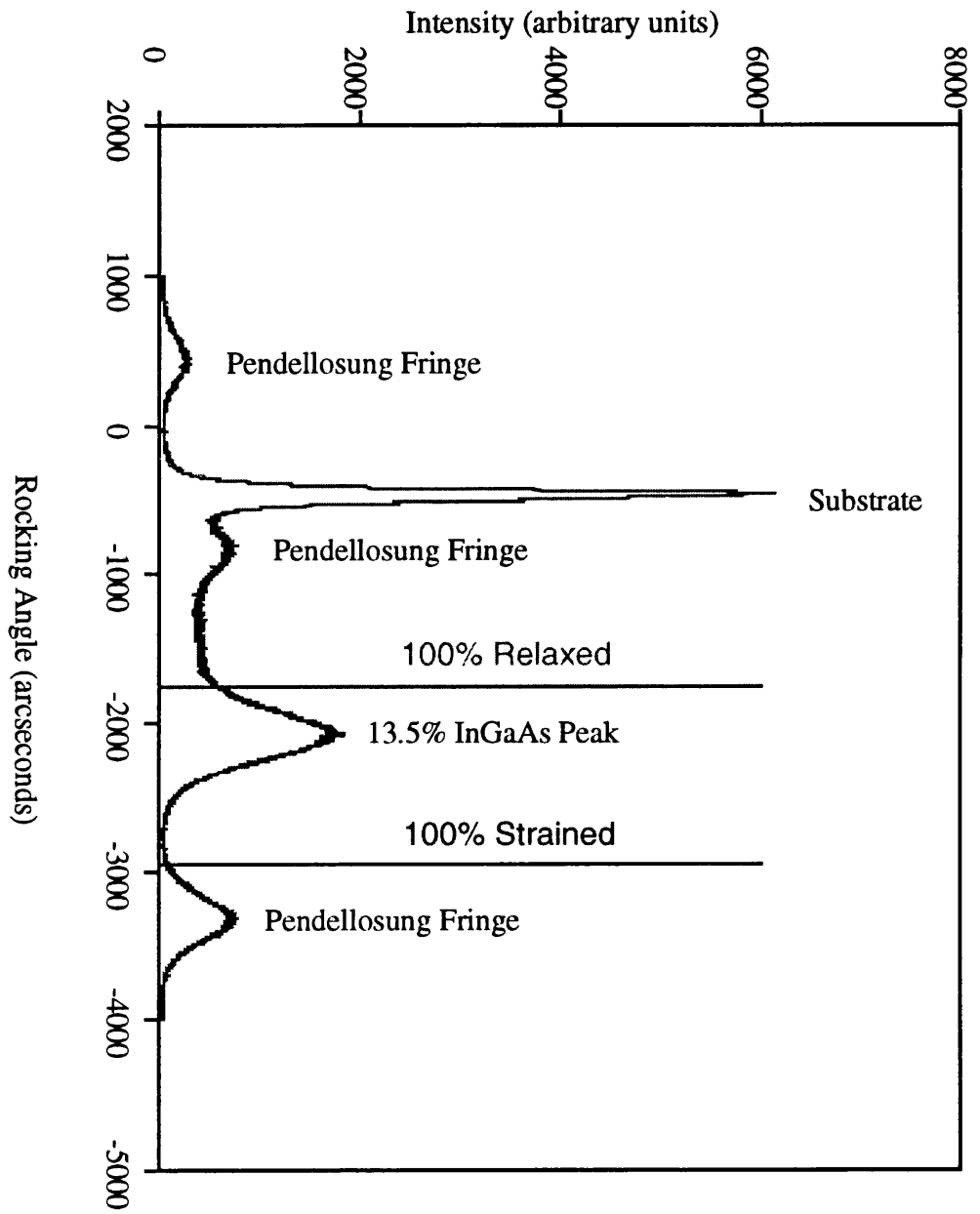
Figure 8.5. DCXD rocking curve for SEED structure.

The figure shows intensity (arbitrary units) versus Rocking Angle (arcseconds). Labeled features include:
- Pendellosung Fringe
- Pendellosung Fringe
- Substrate
- 100% Relaxed
- 13.5% InGaAs Peak
- 100% Strained
- Pendellosung Fringe

158
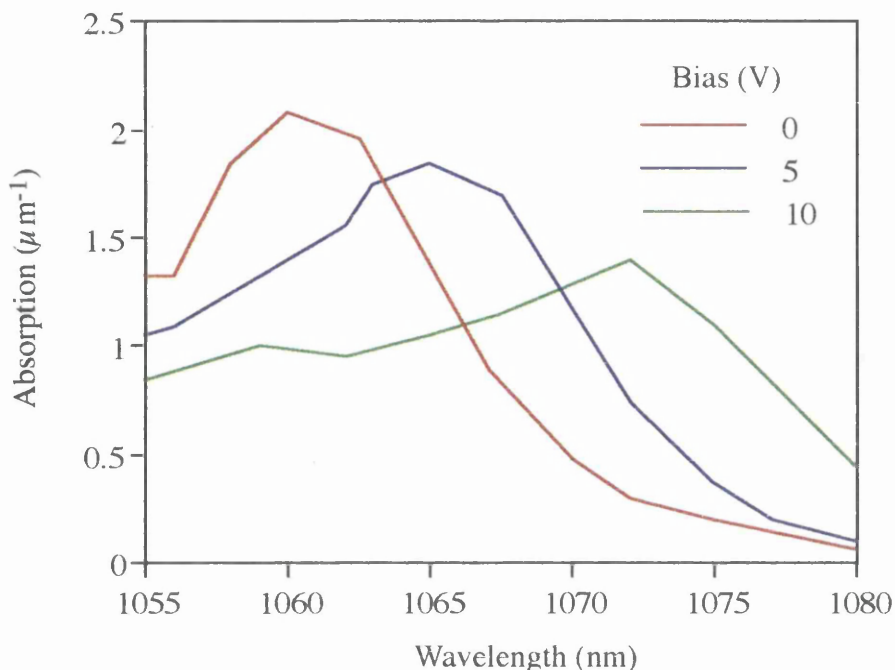
Figure 8.6. Measured absorption spectra of SEED devices for bias of 0V,5V and 10V

The peak MQW absorption at λ_0 and the HWHM on the low energy side of the absorption peak are commonly used figures of merit for SEED material. A comparison between characterisation data for sample #B374 and published values is given in Table 8.3.

Source	well/barrier materials	well/barrier widths (Å)	HWHM of V=0 Peak (meV)	Peak MQW absorption at λ_0 (μm^{-1})
Cunningham *et al.*[13] AT&T	InGaAs/GaAsP	100/100	6.8	0.52
Kim *et al.*[14] Colorado State	InGaAs/InGaP	100/150	5.25	0.49
Woodward *et al.* AT&T	InGaAs/GaAs	100/50	9.9	0.56
#B374[15] Glasgow	InGaAs/GaAs	81/57	6.0	1.20

Table 8.3. Comparison of the performance of SEED material for operation at 1047-1064nm

The surface morphology of the SEED structure showed a faint cross-hatching associated with the generation of misfit dislocations through glide

processes[16]. The wavelength and amplitude of the surface crosshatched profile were measured by optical interferometry and found to be 30nm and 5μm respectively.

8.3.4 Conclusions

A high quality SEED structure has been grown with an absorption peak HWHM figure of 6.0meV. This is the best reported value for the InGaAs/GaAs system and compares favourably with other material systems used for devices operating in the 1047-1064nm wavelength range. Growth was performed in two separate stages: a low substrate temperature and low As_2 overpressure were used for the growth of a linearly graded buffer, and a higher temperature and As_2 overpressure were used for the active region. Calibration of the group III fluxes before growth was performed using RHEED intensity oscillations. The absorption peak of the MQW structure is slightly shifted away from the design wavelength of 1047nm. The reason for this is not known and could be due to calibration errors and the incomplete relaxation of the buffer.

8.4 References

1   'Evolution of the SEED Technology: Bistable Logic Gates to Optoelectronic Smart Pixels'
     A.L. Lentine, D.A.B. Miller
     IEEE Journal of Quantum Electronics 1993 Vol.29 No.2 pp655-669

2   'A 0.1μm T-shaped Gate InP-based HEMT for low noise Application'
     M.Y. Kao, S.M.J. Liu, K.H.G. Duh, P.C. Chao, P. Ho and A.W. Swanson
     Proceedings of the Fourth International Conference on InP and Related Materials 1992 pp 651-653

3   'MBE Growth and Characterisation of Lattice Matched and Pseudomorphic InGaAs/InAlAs/InP HEMTs'
     D.C. Streit, K.L. tan, P.H. Liu, P.D. Chow, J.R. Velebir, R. Lai, T.R. Block, K.S. Stolt and M. Wojtowicz
     Proceedings of the Fourth International Conference on InP and Related Materials 1992 pp 682-684

4 "Microwave Performance of AlInAs-GaInAs HEMTs with 0.2- and 0.1-μm Gate-Length'
U.K. Mishra, A.S. Brown, S.E. Rosenbaum, C.E. Cooper, M.W. Pierce, M.J. Delaney, S. Vaughn and K. White
IEEE Electronic Device Letters 1988 Vol.9 No.7 pp647-649

5 '650Å Self-Aligned Gate Pseudomorphic $In_{0.52}Al_{0.48}As/In_{0.53}Ga_{0.47}As$ High Electron Mobility Transistors'
L.D. Nguyen, A.S. Brown, M.A. Thomson, L.M. Jelloian, L.E. Larson and M. Matloubian
IEEE Electronic Device Letters 1992 Vol.13 No.2 pp143-145

6 'Extremely High Gain 0.15μm Gate-Length InAlAs/InGaAs/InP HEMTs'
P. Ho, M.Y. Kao, P.C. Chao, K.H.G. Duh, J.M. Ballingall, S.T. Allen, A.J. Tessmer and P.M. Smith
Electronic Letters 1991 Vol.27 pp325-326

7 'The Applications of Nanotechnology in Electronic Devices'
S.P. Beaumont
Proceedings of InP and Related Materials 1994 pp371-374

8 '0.05μm-Gate InAlAs/InGaAs High Electron Mobility Transistor and Reduction of its Short-Channel Effects'
T. Enoki, M. Tomizawa, Y. Umeda and Y. Ishii
Japanese Journal of Applied Physics 1994 Vol.33 No.1 pp798-803

9 'Six-stage Digital Free-Space Optical Switching Network Using Symmetric Self-Electro-Optic-Effect Devices'
F.B. McCormick, T.J. Cloonan, F.A.P. Tooley, A.L. Lentine, J.M. Sasian, J.L. Brubaker, R.L. Morrison, S.L. Walker, R.J. Crisci, R.A. Novotny, S.J. Hinterlong, H.S. Hinton and E. Kerbis
Applied Optics 1993 Vol.32 No.26 pp5153-5171

10 'Design of a Symmetrical Self-Electro-Optic-Effect-Device Cellular-Logic Image-Processor'
F.A.P. Tooley and S. Wakelin
Applied Optics 1993 Vol.32 No.11 pp.1850-1862

11 'In$_x$Ga$_{1-x}$As/GaAs Multiple Quantum-Well Optical Modulators for the 1.02-1.07μm Wavelength Range
T.K. Woodward, T. Sizer, D.L. Sivco, A.Y. Cho
Applied Physics Letters 1990 Vol.57 No.6 Pp.548-550

12 'Novel Reflectance Modulator Employing an InGaAs/AlGaAs Strained-Layer Superlattice Fabry-Perot Cavity With Unstrained InGaAs/InAlAs Mirrors'
I.J. Fritz, D.R. Myers, G.A. Vawter, T.M. Brennan, B.E. Hammons
Applied Physics Letters 1991 Vol.58 No.15 pp.1608-1610

13 'Pseudomorphic InGaAs-GaAsP Quantum-Well Modulators On GaAs'
J.E. Cunningham, K.W. Goossen, M. Williams, W.Y. Jan
Applied Physics Letters 1992 Vol.60 No.6 pp.727-729

14 'Strained-Layer In$_{1-x}$As/GaAs and In$_x$Ga$_{1-x}$As/In$_y$Ga$_{1-y}$P Multiple-Quantum-Well Optical Modulators Grown by Gas-Source MBE'
J.W. Kim, C.W. Chen, T.J. Vogt, L.M. Woods, G.Y. Robinson, D.L. Lile
IEEE Photonics Technology Letters 1993 Vol.5 No.9 pp.987-989

15 'InGaAs S-SEEDs and Silicon CMOS Smart Pixels for 1047-1064nm Operation'
D.J. Goodwill, F.A.P. Tooley, M. McElhinney, F. Pottier, C.R. Stanley, D.G. Vass, I. Underwood and M.W.G. Snook
Proceedings of the IEEE/LEOS Topical Meeting on Smart Pixels 1994 pp

16 'Crosshatched Surface Morphology in Strained III-V Semiconductor Films'
K.H. Chang, R. Gibala, D.J. Srolovitz, P.K. Bhattacharya and J.F. Mansfield
Journal of Applied Physics 1990 Vol.67 No.9 pp4093-4098

Chapter 9

Conclusions

9.1 Summary

The MBE growth of $In_{0.53}Ga_{0.47}As$ and $In_{0.52}Al_{0.48}As$ lattice matched to InP is more sensitive to growth conditions than the GaAs/AlGaAs system. The As_2 flux necessary to stabilise the growing surface varies very rapidly as a function of substrate temperature and a very delicate balance must therefore be struck between the substrate temperature required to minimise impurity incorporation and the As_2 overpressure necessary to stabilise the surface at this temperature. Finding the optimum growth conditions requires determination of the minimum possible As_2 partial pressure for a given substrate temperature, and a knowledge of how the properties of the material vary with substrate temperature.

RHEED intensity oscillations can be used to determine the As_2 flux density necessary to suppress the formation of free indium droplets. The onset of In droplet formation correlates with a drop in the measured growth rate of InAs, $In_{0.53}Ga_{0.47}As$ and $In_{0.52}Al_{0.48}As$ and this can therefore be used to identify the required As_2 partial pressure for growth at any substrate temperature. The measured values of minimum As_2 flux for the growth of InAs agree very well with predictions based on simple thermodynamic arguments. These arguments can be extended to deal with the behaviour of $In_{0.53}Ga_{0.47}As$ by treating the ternary alloy as a pseudo-binary compound and employing published values for the activity of InAs in $In_{0.53}Ga_{0.47}As$. A very good fit to the experimental data is then obtained. No data for the activity of InAs in $In_{0.52}Al_{0.48}As$ is available, but a fit to the experimental data yields a value for the ratio between the activity in $In_{0.53}Ga_{0.47}As$ and $In_{0.52}Al_{0.48}As$ which is in good agreement with existing Auger measurements. An accurate understanding of the As_2 flux necessary for the growth of $In_{0.53}Ga_{0.47}As$ and $In_{0.52}Al_{0.48}As$ has thus been achieved, which enables calculation of the minimum permissible As_2 flux for any growth rate and substrate temperature. The minimum As_2 flux necessary for good morphology is considerably less than is common in the literature. The use of relatively low As_2 overpressures offers several advantages. It increases the runtime of the chamber

by slowing down the consumption of As, produces an improvement in interface quality, and reduces the arrival rate of impurities from the As charge.

RHEED measurements of ternary growth rate can also be used to measure desorption from the solid solutions of the lattice matched ternaries. The measured desorption curves are also in good agreement with thermodynamic predictions. It has been shown to be possible to grow $In_{0.52}Al_{0.48}As$ at relatively high temperatures, in the regime where considerable In desorption was present, and still retain accurate control of the composition. This is presumed to be made possible by strain enhanced desorption which produces a 'self-locking' effect.

Accurate control of the composition in the normal growth regime can be obtained by calibrating the incident group III fluxes using RHEED oscillations on separate substrates. The In flux is calibrated by measuring growth rates on InAs substrates, and the Ga and Al fluxes are calibrated by measuring growth rates on GaAs substrates. By adjusting the measured growth rates to a set of well defined values it is possible to obtain composition control to within $\pm250ppm$. This method of calibration was used to grow a series of $In_{0.53}Ga_{0.47}As/In_{0.52}Al_{0.48}As$ single quantum well structures. The photoluminescence energies from wells of varying thickness agree very well with theoretical predictions, indicating that the desired growth rate has been accurately obtained. The major cause of linewidth broadening in the quantum well luminescence is band-filling in the $In_{0.53}Ga_{0.47}As$ which is produced by the ionisation of impurities in the $In_{0.52}Al_{0.48}As$. This can be minimised by growing the structures at temperatures above $530°C$ with minimum As_2 flux. The resultant photoluminescence spectra contain very narrow linewidths and monolayer-splitting can be observed, demonstrating that high interface smoothness has been obtained.

The photoluminescence from bulk $In_{0.53}Ga_{0.47}As$ layers grown with minimal As_2 overpressure is very much influenced by the existence of an InAs segregation layer. Such segregation layers are several monolayers thick and produce a subsidiary peak in the PL spectrum whose position is determined by the mismatch between the substrate and the epi-layer, implying that even very small amounts of strain can significantly increase the amount of In segregation which occurs during growth. This is another reason for ensuring tight control of the composition of lattice matched ternary material since it is possible that the incorporation of dopants into the material could be influenced by the presence of such a segregation layer.

Preliminary investigations of the incorporation of Si into slab- and ∂-doped structures have been performed. For ∂-doped structures the results show an increase in amphoteric behaviour as the doping density rises, which is accompanied by an increase in spreading away from the dopant plane, perhaps

attributable to electrostatic repulsion. This limits the maximum obtainable electron density to $\approx 3 \times 10^{12} cm^{-2}$. The spreading obtained for slab-doped samples is comparable to that for ∂-doped samples and an increase in the activity of the Si dopant is observed when slab-doping is used. This suggests that thin slabs are the more efficient method of generating high carrier densities in $In_{0.53}Ga_{0.47}As$.

The growth of device structures using the principles discussed above has been shown to produce high quality material. Characterisation data from a strain-balanced SEED structure demonstrates that the RHEED calibration technique can also be applied to strained the growth of strained $In_xGa_{(1-x)}As$ on GaAs, yielding state-of-the-art device performance.

9.2 Suggestions for Future Work

The technique of growth in the 'self-locking' regime has only been preliminarily investigated. Although it has been shown that the growth of $In_{0.52}Al_{0.48}As$ is possible at high temperatures, no $In_{0.53}Ga_{0.47}As$ samples have been grown and the sensitivity of the 'self-locking' effect to growth conditions has not been examined. Ideally the validity of the technique should be verified by measuring the composition of a number of samples grown in the regime where significant indium desorption is occurring. If the samples are grown at different substrate temperatures then the composition should, in the absence of a 'self-locking' process, decrease monotonically as the substrate temperature rises. If the desorption is sufficiently increased by strain between the layer and substrate then there should be a temperature range over which the composition does not vary, giving a curve of the form shown in Figure 9.1.
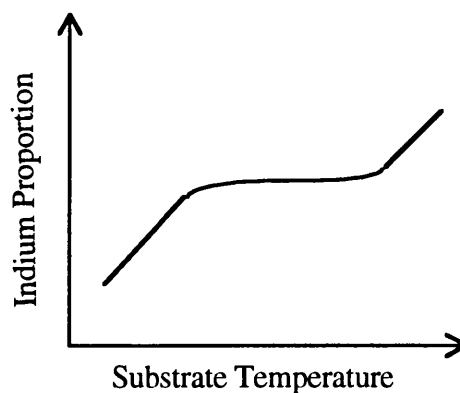
Figure 9.1. Predicted relationship between the In content of InGaAs and the substrate temperature during growth

165

A curve of similar shape should be obtained for the indium proportion as a function of excess indium flux supplied during growth. By performing such measurements experimentally it should be possible to determine the extent of the parameter 'window' in which lattice matched growth is obtained.

The work carried out so far has been restricted to ternary alloys, but similar arguments could be employed for the growth of quaternary $In_xAl_yGa_{1-x-y}As$ material lattice matched to InP. This alloy system spans the same bandgap range (0.9-1.65μm) as $In_xGa_{1-x}As_yP_{1-y}$, however it is only necessary to control one high vapor pressure group V element. The methods described in this thesis for the calibration of group III fluxes are equally applicable to $In_xGa_{1-x}As_yP_{1-y}$ and, with minor modifications the thermodynamic arguments used to determine minimum incident As_2 fluxes, could be extended to deal with this system.

The ternary materials system could be extended to include the growth of strained structures. The use of strained device structures has been shown to result in improvements in the performance of both optical devices such as strained quantum well lasers and electrical devices such as pseudomorphic-channel HEMTs (pHEMTs). The presence of strain in such structures, significantly alters the desorption characterics of the material being grown, which in turn alters the necessary stabilising As_2 flux. There has as yet been very little systematic work on the effects of strain on growth conditions. To a certain extent, the attempt has already been made to expand the techniques for lattice matched growth to the growth of strained device structures, however much work remains to be done.

The studies of the incorporation of Si into $In_{0.53}Ga_{0.47}As$ presented in Chapter 7 are not yet complete and the growth of several additional structures is necessary to provide a complete picture of the incorporation process. This will involve the growth of ∂-doped layers to determine more precisely the amphoteric limit and the point at which all of the incident Si donors are activated. Further slab doped layers are reqired to investigate the influence of segregation processes on the migration of Si atoms. In addition, the doping properties of $In_{0.52}Al_{0.48}As$ layers have yet to be studied.
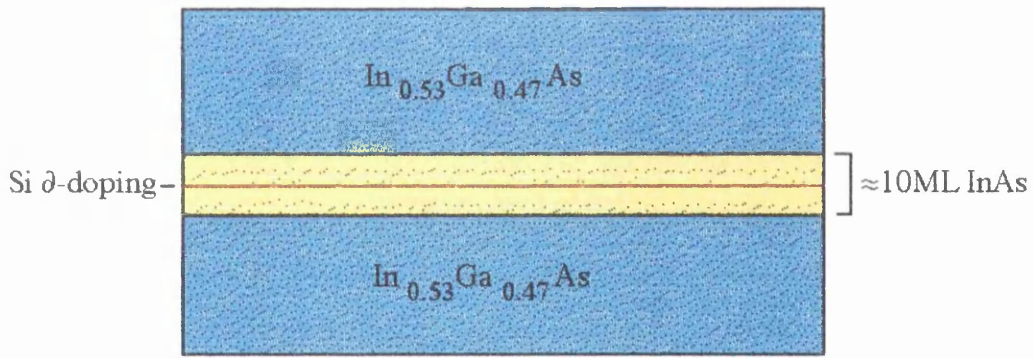
Figure 9.2. Structure to investigate the effect of a thin InAs layer on the incorporation of Si ∂-doping of $In_{0.53}Ga_{0.47}As$.

The use of a thin InAs host has the potential to increase the amphoteric Si ∂-doping limit of $In_{0.53}Ga_{0.47}As$. The ∂-doping could be imbedded in an InAs layer whose thickness was below the critical thickness threshold ($\approx$10ML). This is illustrated in Figure 9.2.

Acknowledgements

I wish to thank Professor Colin Stanley for his supervision during my period in the MBE research group. I am very grateful for the help, advice and friendship of the other members of the group, John Cochrane, Alistair Kean (now at Sharp Labs., Oxford), Martin Holland, François Pottier (even though he does beat me at squash), William Reid and Brigitte Vögele. I particularly wish to thank Ray Hutchins for the exclusive use of his computer to write this thesis, and his constant sniping to make sure I got on with it.

A number of people have contributed to this thesis. They include; Nigel Cameron of the Nanoelectronics Research Group, who was responsible for fabricating and testing HEMT devices; Mark Davison of the Optoelectronics Research Group, who wrote software to calculate quantum well energies; Dominic Goodwill of the Department of Physics at Herriot Watt University, who designed and tested SEED devices; and Elef Skuras of the Department of Physics at Glasgow University who performed magnetotransport measurements on ∂-doped material. Thank you all.

There is another group of people who deserve some thanks. They have also contributed to this thesis, by making life more enjoyable while I was working on it. I wish to express my gratitude to those people, some of whom I have already mentioned. I would especially like to thank the following: Joe Smith and John Bebbington for organising the departmental football team, and kindly allowing me to pretend I could play football; Bill Leitch, John Weaver, Caroline Holland and the late Don Reid for a lot of good times; Calum Cossar and Dave Staton for letting me drive them to various golf courses; Judith Sharples for smiling a lot; Kurt and Anne Lundblad, and my cousins Angela and Thomas for welcoming me into their home and teaching me to ski (I still have the scars); and Delbert Armstrong for teaching me all there is to know about parallel parking.

Finally, I wish to thank my parents for their support and encouragement....oh, and money.

List of Publications

'Measurement of Aluminium Concentration in Epitaxial Layers of $Al_xGa_{1-x}As$
on GaAs by Double Axis X-Ray Diffractometry'
BK Tanner, AG Turnbull, CR Stanley, AH Kean and M. McElhinney
Applied Physics Letters 1991 **59**(18) 2272-2274

'Growth of High Mobility InP'
C.R. Stanley, V.M. Airaksinen, R.H. Hutchins and M. McElhinney
Proceedings of the 6th European MBE Workshop, Tampere, 1991

'Studies of Indium Incorporation Into InAs and InGaAs'
M.McElhinney and C.R. Stanley
Proceedings of the 7th European MBE Workshop, Bardonecchia, 1993

'Reduced Indium Incorporation During the Growth of In(Al,Ga)As'
M.McElhinney and C.R. Stanley
Electronics Letters 1993 **29**(14) pp1302-1304

'Improvements in Strain-Balanced InGaAs/GaAs Optical Modulators for 1047nm
Operation'
D.J. Goodwill, A.C. Walker, C.R. Stanley, M.C. Holland and M.McElhinney
Applied Physics Letters 1994 **64**(10) 1192-1194

'The MBE Growth and MCP/RIE-based Fabrication of InGaAs-GaAs MQW
Structures for 1047-1064nm S-SEED Arrays'
C.R. Stanley, M. McElhinney, F. Pottier, Y.P. Soong, D.J. Goodwill and C.D.
Wilkinson
Proceedings of IEEE/LEOS Topical Meeting on Optoelectronic Materials Growth
and Processing, Lake Tahoe, 1994

'InGaAs S-SEEDs and Silicon CMOS Smart Pixels for 1047-1064nm Operation'
D.J. Goodwill, F.A.P. Tooley, A.C. Walker, M.R. Taghizadeh, M. McElhinney,
F. Pottier, C.R. Stanley, D.G. Vass, I. Underwood, M.W.G. Snook, M.H. Dunn, J.
Hong and B.D. Sinclair
Proceedings of IEEE/LEOS Topical Meeting on Smart Pixels, Lake Tahoe, 1994

'Operation of 16x16 array of strained MQW InGaAs/GaAs S-SEEDs for
1047-1064nm'
D.J. Goodwill, A.C. Walker, M. McElhinney, F. Pottier and C.R. Stanley,
Proceedings of 3rd International Conference on Optical Computing, Edinburgh,
1994

'Quantum Transport Measurements on Si ∂- and slab-doped InGaAs grown by
MBE'
M. McElhinney, E. Skuras, S.N. Holmes, E.A. Johnson, A.R. Long and C.R.
Stanley
Proceedings of the 8th International Conference on MBE, Osaka, 1994
(to be published in the Journal of Crystal Growth)

'Growth and Thermodynamic Analysis of InGaAs and InAlAs Lattice Matched to
InP'
M. McElhinney and C.R. Stanley
Proceedings of the 8th International Conference on MBE, Osaka, 1994
(to be published in the Journal of Crystal Growth)

'Far-Field Behaviour of 980nm Lasers with Band Shifted Extended Regions'
K. McIlvanney, J. Carson, A.C. Bryce, M. McElhinney and J.H. Marsh
Presentation to the Institute of Physics Congress, Brighton, 1994